NTNU

Norwegian University of
Science and Technology

Fabrication of a Photonic Crystal using self-assembly

A potentially new rear reflector for thin solar cells

Håvard Granlund

Master of Science in Electronics

Submission date: June 2009

Supervisor: Tor A Fjeldly, IET

Norwegian University of Science and Technology
Department of Electronics and Telecommunications

Problem Description

When moving to very thin solar cells, a problem arises with photons leaving the cell before being absorbed. One possible solution to this, is to use a photonic crystal (PC) as a rear reflector. PCs have the rather nice feature that they can reflect light in a non-specular manner, which can greatly enhance the otical pathlength of light within the cell, as it can be reflected almost parallel to the wafer. Another nice property of PCs is that they can reflect light incoming from any angle.

In this master project an attempt will be made at making an inverted opal photonic crystal. This will be done in three steps: (1) growing an opal using self-assebly of sub-micrometer spheres from a colloidal suspension, then (2) filling in the gaps between the spheres with a low temperature, low pressure plasma enhanced chemical vapour deposition process, before (3) the spheres are removed by evaporating them at high temperature, leaving the silicon framwork behind, i.e. the inverted opal.
In addition, reflection simulations of an inverted opal on a silicon substrate will be done.

Assignment given: 26. January 2009
Supervisor: Tor A Fjeldly, IET

Preface

This master thesis was written in my 5^th year at the Norwegian University of Science and Technologi (NTNU). The project work has been done at the Institue for Energy Technology (IFE), Kjeller.

I would like to thank my supervisor at IFE, Erik Stensrud Marstein, for invaluable help and motivation during the project, and everyone else at the Solar department at IFE for being such a good bunch of heroes. A great thanks also goes to my fellow students at UNIK for supplying me with an unending stream of distractions, and for receiving them with equal gratitude.

Summary

The major issue with solar cells today, is the price per watt. To tackle this challenge several approaches are being made. One possible approach is to reduce the amount of silicon raw material used in todays wafer-based solar cells by making the wafers thinner. This approach does however bring with it another problem; much of the incident light will escape the cell before being absorbed. One possible way to solve this problem is to use a photonic crystal (PC) as a rear reflector. PCs is a periodic dielectric structure that can reflect light in a non-specular manner, which can substantially increase the optical pathlength for the light within the cell, and hence increase the probability of absorption- One such PC is the inverted opal.

To make an inverted opal, one first fabricates a synthetic opal, consisting of microspheres of some kind, that can be used as a template. The gaps between the spheres of such an opal can then be filled with a suitable dielectric, e.g. silicon, and the spheres can be removed by a selective process, leaving the inverted opal structure.

In this master project, opals were attempted made with Ugelstad spheres and polysterene (PS) spheres. With the Ugelstad spheres, wafer sized monolayers were made, but opals were not achieved. The PS spheres however, proved very suitable, and opals with a grain size of 150x300μm were successfully made. These opals were then partially inverted, by first filling in the gaps between the spheres with silicon, using a low temperature low pressure PECVD process, and then heating the samples to 600℃ for 2.5 hours.

Contents

List of Figures

Chapter 1

Introduction

According to the International Energy Agency's (IEAs) annual report, the World Energy Outlook (WEO) 2008, the current global trends in energy consumption and supply need to change. The future of human prosperity depends on it. There are two main tasks ahead: Securing the supply of affordable and reliable energy; and converting to environmentally friendly energy sources that are both sustainable and effective [1]. The tasks are overwhelming, but they are not insurmountable.

Today, fossil fuels are the world's main supply of energy, and will beyond doubt remain so for many years to come. If nothing is done to change this, fossil fuels are estimated to account for 80% of the world's energy consumption in 2030, which is only slightly down from today (in %; the energy demand is estimated to rise by 1.6% every year, increasing the energy demand by 45% from today to 2030)[1]. Should this happen, and such a trend continue in the long term, it will result in catastrophic and irreversible damage to the global climate. To change the current trend, the average consumers needs to change how they use energy, and energy suppliers have to implement "cleaner" energy sources.

One possible energy source is the sun. The amount of energy from the sun that hits the surface of the earth is more than 10 000 times higher than today's energy consumption, and is unlike other energy sources, available everywhere. Although this should make the sun an ideal choice as an energy source in the future, there are some major challenges that have to be solved before solar energy can become a viable replacement to hydrocarbon energy sources, like oil and coal.

One way to utilize solar energy, is to convert the photons in the sunlight to electrical energy by exploiting the photovoltaic effect. This is what is done in solar cells, which typically have an ouput of several ampère and 0.5V. However, solar cells are usually connected in parallel and series in a solar module (or solar

[1]This is from the reference scenario in the WEO, and embodies only those governmental actions that has already been enacted or adopted

panel if you like) to generate the desired voltage and current[2]. Another reason for mounting the cells in a solar module, is to protect them from external harm. The major issue with solar cells, as for most solar energy solutions, is the price per watt which is 2-5 times higher than for the current grid connected electrical energy [3], depending on sunlight conditions and local energy prices. To make solar cells a viable alternative, two main approaches can be taken. One is to reduce the cost per module, another is to increase the efficiency of the cells. A combination of the two will probably be needed.

To tackle the challenges of price and efficiency, several approaches are possible. One approach is to increase solar cell efficiency, either through continous improvements of existing wafer-based or thin film solar cells, or through the development of radically more efficient solar cells. One example of the latter is the so-called tandem cell [2], which essentially is two or more cells placed on top of each other that are optimized for different parts of the light spectrum, so that a greater portion of the incoming light can be utilized effectively. Another approach is to reduce cost, for example by reducing the cost or the amount of silicon raw materials used in wafer-based solar cells. In Norway, companies like REC, Elkem and Fesil are reducing the cost by introducing new production processes for silicon.

The approach that is important for this paper, is to reduce the amount of silicon used in solar cells by using thinner wafers. Wafers that are thinner than those used in today's standard cells can already be made. One example of a company that is aiming at this is SiGen, a North American company that has developed a method to make silicon wafers significantly thinner than todays standard wafers, with a method very different from today's standard method of sawing. Using their technology, wafers with a thickness below 20μm have been fabricated. However, thinner wafers bring another problem; much of the incident light will escape the cell before being absorbed.

High energy photons are absorbed shortly after entering the silicon, but the photons in the near visible part of the IR spectrum travel quite far before being absorbed. To prevent the photons from simply traveling through the solar cell and leaving at the other end, two approaches are currently being used; surface texturing [2] and an aluminum rear reflector [2]. The textured surface causes the incident light to be refracted at more oblique angles, leading to a longer optical pathlength[2] for the light in the cell. The aluminum rear reflector on the other hand, reflects light that has traveled through the cell, thereby increasing the optical pathlength further. This length can be further enhanced by total internal reflection from the top of the cell, if the angle is oblique enough, which can be achieved with a combination of surface texturing and an aluminum rear reflector. Until now the combination of surface texturing and a rear reflector has been satisfactory as the

[2]The physical length the light travels times the refractive index of the material, n

wafers are sufficiently thick to absorb the photons before they leave the solar cell. However, as the wafers get thinner, the optical pathlength becomes increasingly shorter, and hence more and more photons will escape before contributing to current generation within the cell.

Several alternative rear reflectors have been considered to solve this problem; a metal grating at the interface between the aluminum and silicon [4], a Distributed Bragg reflector (DBR) with a dielectric grating [4, 5] and a photonic crystal (PC) [4, 6], which is of interest for this paper. All of the above solutions have one thing in common; they may reflect light in a non-specular manner [4–7], which will increase the optical pathlength of the photons and hence their probability of being absorbed. PCs have a property that makes them more desireable than the two other candidates. They can reflect light incoming from **any** angle, while the other solutions are optimized for one angle of incidence. In figure 1.1 the difference in reflection between an aluminium and a PC is visualized. Notice that although the PC reflect light in a non-specular manner, it will still reflect some of the light specularily as well.

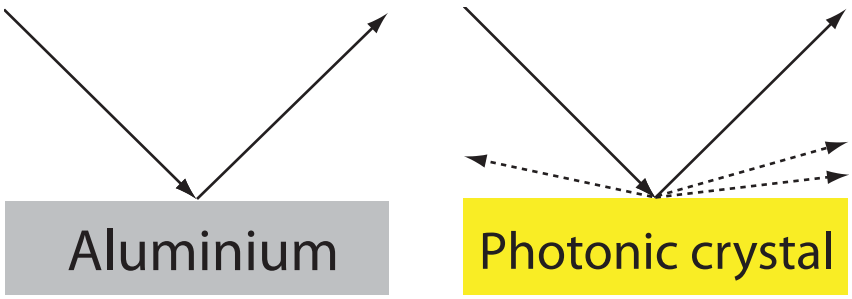

Figure 1.1

One type of PC that has been proposed as a reflector, is the inverted opal [7], which can be fabricated using self-assembly of micro- and submicrometer spheres situated in a liquid. These spheres will tend to crystallize in a face centered cubic (fcc) structure [8]. Crystals made this way are called synthetic opals and can be used as a template to make the inverted opal. Self-assembly of spheres spheres to make inverted opal PCs is a very attractive route as it has the potential to create structures with full three dimensional ordering. This is very important for the reflective properties of PCs, and is what sets them apart from the previously mentioned gratings.

In this master project an attempt at making an inverted opal will be made. This will be done by first making an opal template, then filling in the gaps between the spheres with silicon and finally removing the spheres, leaving the silicon framwork, i.e. the inverted opal. The opal will be attempted made using Ugelstad spheres

and polysterene (PS) spheres, the silicon will be deposited with a plasma enhanced cheimical vapour depositioin (PECVD) process and the spheres will be removed by evaporating them at high temperature. In addition, reflection simulations of an inverted opal on a silicon wafer will be done.

Chapter **??**: Theory will start off with some basic theory on PCs, with a special emphasis on the inverted opal structure and reflection from PCs towards the end. The theory will then continue with an explanation of various opal growth methods and mechanisms, before rounding up with crystal defects and their effect on PCs. Chapter 3: Experimental will present the various opal growth methods used in the master project, and theory on the characterization techniques used as well as PECVD. At the end of the chapter, the theory behind the simulation program MEEP will be presented. Chapter 4: Reflection simulations will, not surprisingly, present the results from the reflection simulations of inverted opal structures on a silicon substrate, as well as visualize some of the features of PCs in general. In chapter 5: Results, the results from the opal growth experiments will be presented, as well as the results from the opal inversion process. These results, together with the simulations, will be discussed in chapter 6: Discussion, which is followed up by the chapters 7: Conclusion and 8: Further work. In appendix MEEP kode the code used in the reflection simulations can be found, and the code used to plot the data in matlab can be found in appendix **matlab kode**.

Chapter 2

Theory

As mentioned in the introduction, this thesis looks at one of the problems that arises when moving to thinner wafers for solar cells. The particular problem in question, is the decrease in the optical pathlength, i.e. the amount of time the light spends inside the solar cell, due to thinner wafers. With thinner wafers this pathlength unfortunately becomes shorter, which results in a decrease in absorption and hence the efficiency and current generation of the cell. In the graph in figure 2.1 the absorption in silicon is plotted versus wavelength and optical pathlength. The graph clearly shows that for thinner solar cells to utilize the near-visible part of the IR-spectrum (800-1200nm), something has to be done. Currently, the optical pathlength is inreased by surface texturing, causing the light to be refracted at a more oblique angle when entering the cell, and an aluminium rear reflector. However, these methods are proving less than satisfactory for very thin cells, and something better is desired. A photonic crystal (PC) can be this something.

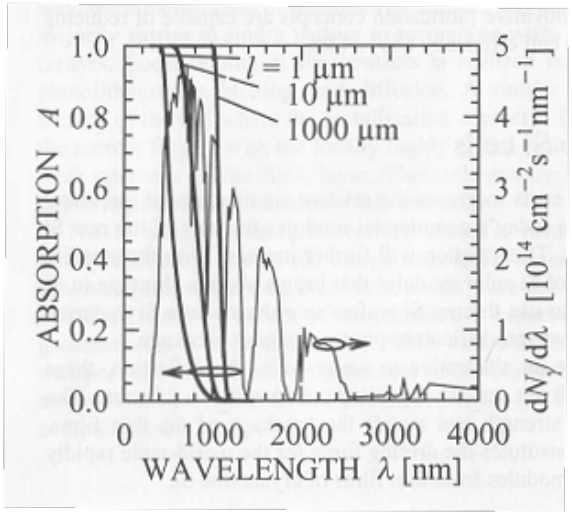

Figure 2.1: Absorption in silicon as a function of wavelength for three different optical pathlengths (10,100 and 1000 μm.). The other graph is the solar photon flux at the earth surface as functioon of wavelength.

PCs have a property that is particularily useful; they can reflect light in a non-specular manner (i.e. into diffractive orders). If a PC is used as a backside reflector, this can result in light being reflected almost parallel to wafer, which again could

significantly enhance the optical pathlength and, as an extension, the absorption. Dielectric and metallic gratings have also been proposed, but they have to be optimize for one angle of incidence, whereas the PC can reflect light incoming from any angle, making it the superior choice.

In this chapter PCs and their reflective properties will be described, and the inverted opal structure will be given special attention. Most emphasis will however be given to the crystallization process of microspheres. The chapter will then wrap up with a description of various crystal defects and their effect on PCs.

2.1 Photonic crystals

Photonic crystals (PCs) represent a class of materials that behaves as the photonic analog to the semiconductor (SC). As stated in [7]; *in a PC the atoms of the crystal lattice is replaced by macroscopic media with differing dielectric constants, and the periodic potential is replaced by a periodic dielectric function.*

In an atomic crystal lattice, electrons can't move in certain directions with certain energies due to Bragg reflections [9]. The lattice is said to introduce an energy **gap**, or **band gap**. The size of the gap increases with increasing lattice potential [9], and if such gaps exist for all possible propagation directions and the lattice potential is strong enough for these gaps to overlap (in energy), a **complete band gap emerges**. A material with such characteristics is called a semiconductor, or an insulator if the gap is big enough. Similarily, a PC can have a complete **photonic** band gap (PBG) if the dielectric constants of it's constituent materials differ sufficiently and the absorption of light is minimal. The effect of the complete PBG, is that incident light on a PC with an energy corresponding to an energy in the gap cannot propagate through the crystal, but will be reflected, regardless of the angle of incidence. The emergence of the PBG in PCs can be explained based on partial reflections at an interface between two materials, as given by Fresnel's equations [10], and by constructive interference of waves fulfilling the Bragg condition [10]. In this paper however, the PBG will be explained on a basis of band structures.

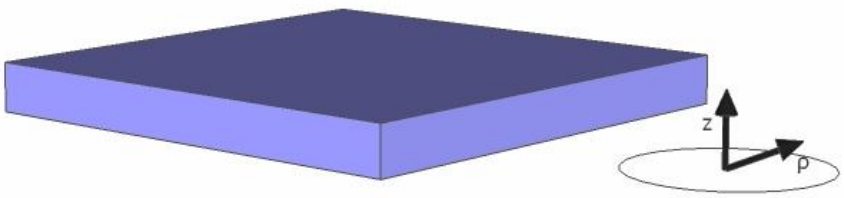

Figure 2.2: A glass plane.

Before continuing with the theory of PCs, the concept of **bands** should be explained further. Consider the glass plane in figure 2.2. This structure has light modes[1] described by plane waves modulated by $\mathbf{h}(z)$, which represent the finite extention of the glass plane in the z-direction [7]:

$$\boldsymbol{H}_k(r) = e^{i\boldsymbol{k}_\parallel \boldsymbol{\rho}} \boldsymbol{h}(z), \tag{2.1}$$

where $\mathbf{k}_\parallel = \mathbf{k} - \mathbf{k}_z = \mathbf{k}_x\hat{x} + \mathbf{k}_y\hat{y}$ is the in-plane wavevector. The allowed propagation modes of light that are confined to this plane can be classified by $\mathbf{k}_\parallel$, and can be lined up in order of increasing frequency for a given $\mathbf{k}_\parallel$ (remember that $|\mathbf{k}| = \left|\mathbf{k}_z + \mathbf{k}_\parallel\right| = \frac{w}{c}$). Labeling a mode by it's place in line of increasing frequency by n, a mode can be described by a unique combination $(\mathbf{k}_\parallel, n)$. Here, n is called the **band number**. If there is a discrete allowed number of frequencies for a given $\mathbf{k}_\parallel$, n will have integer values. If the wavevector of each mode in the plane of glass is plotted versus frequency, the different bands corresponds to the different lines, as can be seen in figure 2.3.

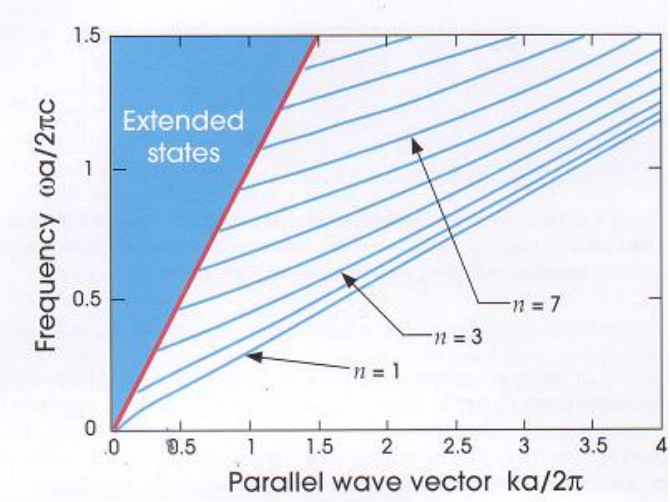

Figure 2.3: The blue lines represent the mode frequencies for a plane of glass with thickness a. The red line corrsponds to light with no k_z component, while the shaded blue region corresponds to light that is not confined to the plane of glass. Figure taken from [7].

[1] A single mode is given by an electric field distribution, a frequency and a wavevector

2.1.1 The master equation and scaling properties of Maxwell's equations

So, how can one find the allowed modes in a given structure? First of all, some limitations must be set: the material is assumed to be linear, i.e. no higher order terms [2], and that it's macroscopic and isotropic so that **E(r,**ω**)** and **D(r,**ω**)** are related by ϵ_0 multiplied by a scalar dielectric function $\epsilon(\mathbf{r},\omega)$. In addition, any frequency dependence of the dielectric constant is ignored and the material is assumed to be transparent. The latter condition allows us to treat $\epsilon(\boldsymbol{r})$ as purely real and positive. This leads to the following form of the Maxwell equations:

$$\nabla \cdot \boldsymbol{H}(\boldsymbol{r},t) = 0 \tag{2.2a}$$

$$\nabla \cdot [\epsilon(\boldsymbol{r})\boldsymbol{E}(\boldsymbol{r},t)] = 0 \tag{2.2b}$$

$$\nabla \times \boldsymbol{E}(\boldsymbol{r},t) + \mu_0 \frac{\delta \boldsymbol{H}(\boldsymbol{r},t)}{\delta t} = 0 \tag{2.2c}$$

$$\nabla \times \boldsymbol{H}(\boldsymbol{r},t) - \epsilon_0 \epsilon(\boldsymbol{r}) \frac{\delta \boldsymbol{E}(\boldsymbol{r},t)}{\delta t} = 0 \tag{2.2d}$$

Althogh these restrictions have been made, the theory based on them will serve as a good foundation for understanding the general properties of more complex materials.

The next step is to separate the time dependence from the spatial dependance. This can be done by expanding the fields into a set of **harmonic modes**, i.e. field patterns that varies sinusoidally with time. As "usual" these harmonic modes will be written as a spatial pattern times a complex exponential:

$$\begin{aligned} \boldsymbol{H}(\boldsymbol{r},t) &= \boldsymbol{H}(\boldsymbol{r})e^{-i\omega t} \\ \boldsymbol{E}(\boldsymbol{r},t) &= \boldsymbol{E}(\boldsymbol{r})e^{-i\omega t}. \end{aligned} \tag{2.3}$$

Expressing the fields as complex is only done to make the mathematical calculations easier however, and one has to take the real part to get the actual physical fields.

If the equations in 2.3 is inserted into Maxwell's divergence equations 2.2a and 2.2b, the following conditions are reached:

$$\nabla \cdot \boldsymbol{H}(\boldsymbol{r}) = 0, \quad \nabla \cdot [\epsilon(\boldsymbol{r})\boldsymbol{E}(\boldsymbol{r})] = 0, \tag{2.4}$$

which means that the electromagnetic waves, which the fields are built up of, is transverse to the direction of propagation.

[2] n(E)=n + a_1E + $a_2 E^2/2 + \cdots$ [10]

Next, if one inserts eq. 2.3 into Maxwell's curl equations 2.2c and 2.2d, and then decouples the equations, the **master equation** is reached:

$$\nabla \times \left(\frac{1}{\epsilon(\boldsymbol{r})} \nabla \times \boldsymbol{H}(\boldsymbol{r}) \right) = \left(\frac{\omega}{c} \right)^2 \boldsymbol{H}(\boldsymbol{r}). \tag{2.5}$$

This equation, together with eq. 2.4 can tell us all one needs to know about $\boldsymbol{H}(\boldsymbol{r})$.

So, knowing the master equation, how does one find the allowed modes of a known structure $\epsilon(\mathbf{r})$? The first step is to solve the master equations to the find all the $\mathbf{H(r)}$ modes, and their corresponding frequencies, which is allowed by the structure $\epsilon(\boldsymbol{r})$ and that upholds the transversality requirements. Next, $\mathbf{E(r)}$ is found by inserting this result into equation 2.2d (using the complex fields in eq. 2.3 as before). This procedure ensures that $\mathbf{E}$ upholds the transversality requirements.

The main point in deriving the master equation here, is to use it to show the scaling invariance of the Maxwell equations. Contrary to atomic physics, there are no fundamental constant with the dimension of length for PCs. There is only an assumption that the system is macroscopic. This means that when the mode profiles for a given structure have been found, the solutions for a scaled version of the structure can be found by simply rescaling the mode profiles and the corresponding frequencies.

Suppose that the electromagnetic mode $\mathbf{H(r)}$ with frequency ω in a dielectric structure $\epsilon(\mathbf{r})$ is known. What if the dielectric structure is simply compressed or expanded? The new dielectric function then becomes $\epsilon(\boldsymbol{r}/s)=\epsilon'(\boldsymbol{r})$, where s is an arbitrary scaling factor. By changing the variables in eq. 2.5, with $\boldsymbol{r}'=s\boldsymbol{r}$ and $\nabla'=\frac{\nabla}{s}$, the master equation becomes:

$$s\nabla' \times \left(\frac{1}{\epsilon(\boldsymbol{r}'/s)} s\nabla' \times \boldsymbol{H}(\boldsymbol{r}/s) \right) = \left(\frac{w}{c} \right)^2 \boldsymbol{H}(\boldsymbol{r}'/s) \tag{2.6}$$

By noticing that $\epsilon(\boldsymbol{r}'/s)=\epsilon'(\boldsymbol{r}')$ and dividing by s, the following equation is reached:

$$\nabla' \times \left(\frac{1}{\epsilon'(\boldsymbol{r}')} \nabla' \times \boldsymbol{H}(\boldsymbol{r}'/s) \right) = \left(\frac{w}{cs} \right)^2 \boldsymbol{H}(\boldsymbol{r}'/s). \tag{2.7}$$

Equation 2.5 is just the master equation, but now with scaled versions of the old mode profile and its frequency. As stated above: the solution for a problem at one length scale determines the solution at all length scales, a rather neat feature[3]. So, why is this so useful? Related to figure 2.4 below, which is a stack of layers with alternating dielectric constant: if this structure has a reflection peak over a narrow wavelength range, this wavelength range can be shifted up or down (in

[3]It's really, really cool!

wavelength) simply by increasing or decreasing the layer thickness. This will be further visualized later, although for a more complicated structure.

2.1.2 Optical properties

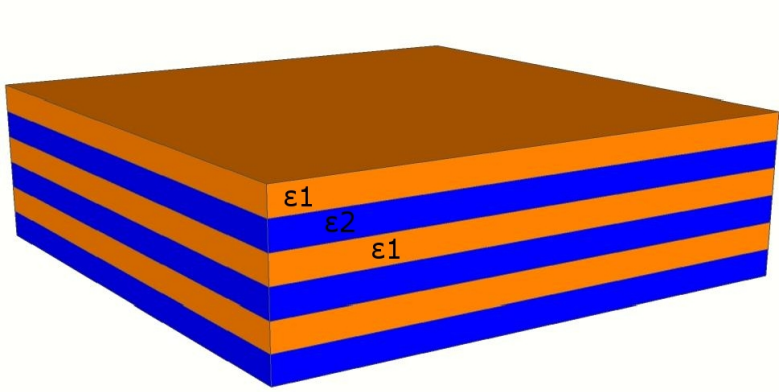

Figure 2.4: A multilayer structure. The z-direction is perpendicular to the shown planes.

For a qualitative understanding of how a PC works, it's instructive to look at the one dimensional case. The simplest one dimensional PC is the multilayer film, which is a stack of layers with alternating dielectric constant (figure 2.4). The electromagnetic modes that can be sustained by such a crystal can be written in Bloch form [7]:

$$\boldsymbol{H}_{n,k_z,\boldsymbol{k}_\parallel}(\boldsymbol{r}) = e^{\boldsymbol{k}_\parallel \boldsymbol{\rho}} e^{ik_z z} \boldsymbol{u}_{n,k_z \boldsymbol{k}_\parallel}(z), \tag{2.8}$$

where ρ denotes a vector in the x-y plane. The form of equation 2.8 is called a Bloch state, and can be thought of as a plane wave modulated by a periodic function, $\mathbf{u}(z)$. The function's period is $\mathbf{a}$, which is the period of the lattice:

$$\boldsymbol{u}(z) = \boldsymbol{u}(z + ma), \tag{2.9}$$

where m is an integer. One feature of the Bloch states is that a Bloch state with wavevector k_z is identical to a state with wavevector $k_z + m2\pi/a$ [7]. This means that the mode frequencies must be periodic in k_z [7]:

$$\omega(k_y) = \omega(k_y + \frac{m2\pi}{a})), \tag{2.10}$$

and that it's sufficient to consider k_z in the range -$\pi/a < k_z \leq \pi/$a. This interval is called the first **Brillouin zone**, and contains all the nonredundant values of k_z [7, 9]. Although the frequency of the Bloch states are periodic, this doesn't mean that higher frequency modes don't exist in the PC. The set of frequencies that are covered by eq. 2.10 are labeled by a band number n, as explained above. There exists an infinite number of such bands ranging all possible frequencies. $k_{\|}$ can assume any value as the crystal has continous translation symmetry in the x-y plane, i.e. the system is invariant for any translation operator working in the x-y plane [7], as one would suspect since the materials are homogenous in this plane:

$$\hat{T}_d \epsilon(\rho) = \epsilon(\rho - d) = \epsilon(\rho). \tag{2.11}$$

$\hat{T}_d$ is a translation operator working in the x-y plane and $\epsilon(\rho)$ is the dielectric constant in the x-y plane.

In a homogenous medium, the speed of light will be reduced by the refractive index of the material, and the frequency will be a linear function of the wavevector. The function

$$\omega(k) = \frac{ck}{\sqrt{\epsilon}}, \tag{2.12}$$

will then give the possible propagation modes of the material.

When light is traveling through the one dimensional PC in figure 2.4 at normal incidence to the layers, the linear relation between frequency and wavevector (equation 2.11) is broken due to the inhomogenity of the crystal in the z-direction. The light will experience an effective refractive index depending on the distribution of it's electric field in the two materials. For waves with a wavevector at the edge of the Brillouin zone, there will be a gap in the allowed frequencies, i.e. a band gap. This will divide the modes into different bands, labeled n=1,2,3,4...

To understand why this band gap appears, let's look at the different ways the electric field can be distributed in the materials for a wave at the edge of the Brillouin zone (wavelength equals 2a), where the band gap appears. This wave can be centered in two different ways; either by having the nodes in the material with a low refractive index, or in the one with high refractive index. Figure 2.5 shows the two possible field distributions for alternating layers with $\epsilon_1 = 13$ and $\epsilon_2 = 12$. The two distributions represent modes in the bands n=1 and n=2. Positioning the fields in any other way will violate the symmetry of the unit cell about it's center [7]. According to the **variational theorem** [7], the lowest frequency mode is the mode that minimizes the **energy functional**:

$$U_f(\boldsymbol{H}) = \frac{\int d^3\boldsymbol{r} \left| \bigtriangledown \times \boldsymbol{E}(\boldsymbol{r}) \right|^2}{\int d^3\boldsymbol{r} \epsilon(\boldsymbol{r}) \left| \boldsymbol{E}(\boldsymbol{r}) \right|^2}, \tag{2.13}$$

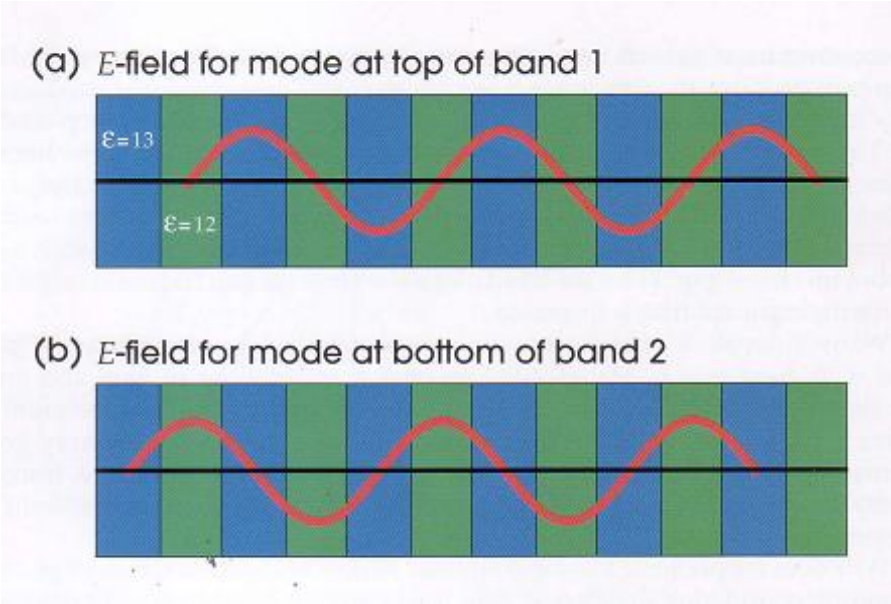

Figure 2.5: Field distributions for modes at the edge of the Brillouin zone. Figure taken from [7].

and stays orthogonal to the modes below it in frequency. As can be seen from equation 2.13, the way to minimize the energy functional is to concentrate the electric field in the regions with high refractive index and to minimize the number of oscillations [7]. From equation 2.12, it then becomes clear that the mode with a larger fraction of it's energy in the high index material will have a lower frequency than the one with more of it's energy in the low index material. This also makes it clear why a high index contrast is needed for a large gap, as a high index contrast will cause the two modes to concentrate their fields in materials with increasingly different refractive index, and therefore have increasingly different frequencies. Figure 2.6 shows the gap for ϵ_1=13 and ϵ_2=13 (*left*), ϵ_2=12 (*middle*) and ϵ_2=1 (*right*). It's important to note that for a one dimensional PC, light incident at an angle will experience no band gap. This is because there is no periodic dielectric regions in the x-y plane that can reflect the light and split open a gap [7]. When choosing a backside reflector for solar cells, it's beneficial to have a rear reflector that reflects light incoming at any angle. This is of course motivated by the movement of the sun across the sky.

For a PC to exhibit a band gap in all directions, also known as exhibiting a complete PBG, it needs to be periodic in all directions. In addition to this, the structure has to accomodate a band gap for both transverse magnetic (TM) and transverse electric (TE) polarizated light, which favours different conditions. The TE polarization favours a connected network of a dielectric material with

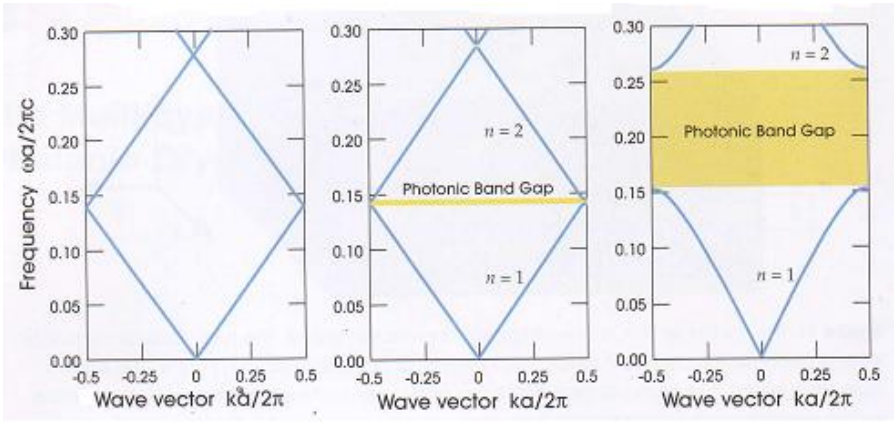

Figure 2.6: The diagrams shows dispersion diagrams for a multilayer film with layers of alternating dielectric constant. *Left*:$\epsilon_1 = \epsilon_2 = 13$, *Middle*: $\epsilon_1 = 13$ and $\epsilon_2 = 12$, *Right*:$\epsilon_1 = 13$ and $\epsilon_2 = 1$. Note that the photonic band gap increases with increasing contrast in dielectric constant. Figures taken from [7].

high refractive index which the electric field can follow, while the TM polarization favours isolated spots of high dielectric constant [7]. These restrictions makes it obvious that a compromise has to be reached. One such compromise is to use a lattice of dielectric spots connected by thin veins. In three dimensions this has been realised in several different ways; the *Yablonovite* structure [11], the *woodpile* stack [12, 13] and the one of interest in this thesis, the *inverted opal* [14]. The three abovementioned structures are shown in figures 2.7(a), 2.7(b) and 2.7(c). The inverted-opal structure will be described in more detail below.

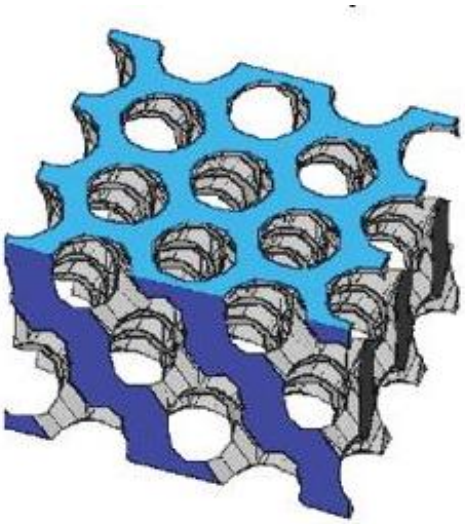

(a) Yablonovite structure.

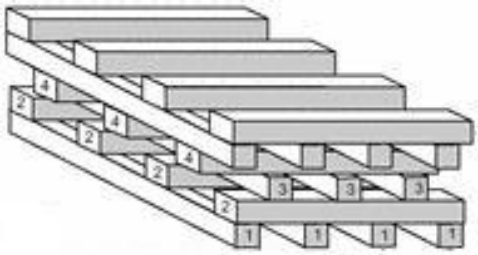

(b) Woodpile structure.

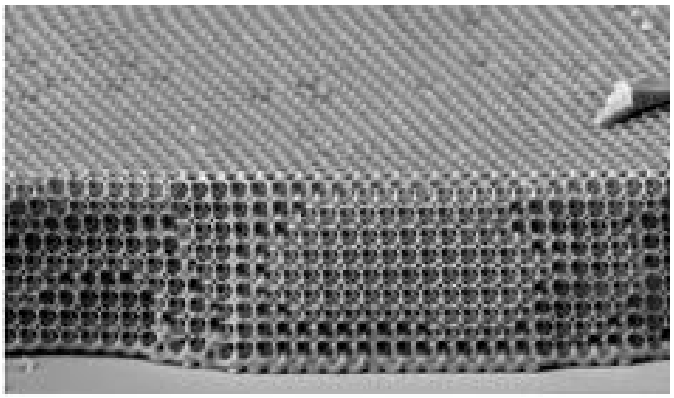

(c) Inverted opal structure.

Figure 2.7: Three possible PC structures. Figure **a** shows the Yablonovite structure, figure **b** shows the woodpile structure and figure **c** shows the inverted opal structure, which is of importance in this paper. Figures taken from [15], [7] and [8] respectively

.

2.1.3 Reflection from a PC

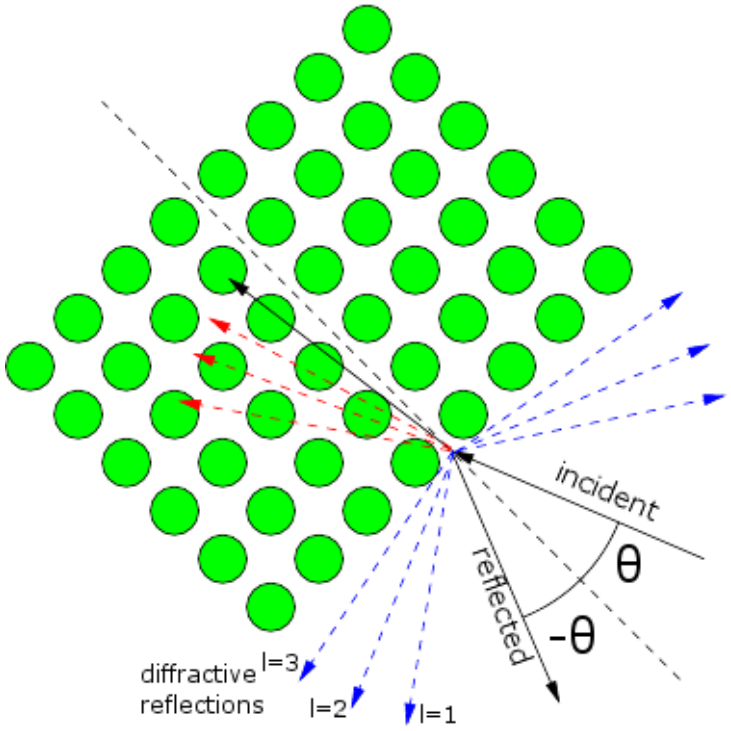

Figure 2.8: Figure shows light incident on a PC, represented by the lattice of green discs. Black arrows represent the reflection, diffraction and refraction for the case of a homogenous medium. Blue arrows represents diffraction orders, and red arrows represents possible refraction orders introduced by the PC structure.

Consider plane waves incident on a PC at some angle. Some of this light will be reflected in a specular manner, some of it will be refracted, traveling at some angle within the PC, and some of the light will be reflected and refracted at angles not existing for the case of a homogenous medium (see figure 2.8). These angles depend on the crystal periodicity, frequency of the light and the band structure of the PC [5–7].

According to Bloch's theorem [7, 9], in a linear system with discrete translational symmetry, the Bloch wave vector $\mathbf{k}$ will be conserved[4] as the light propagates. At the interface to the PC there is only translational symmetry parallel to the plane of incidence, so that only the wavevector parallel to the interface, $k_{\|}$, will be conserved. For a wave incident from a medium with refractive index n_i, i.e.

[4]Note that for a Bloch, wave k and k + $\frac{2\pi l}{a}$, where a is the period and l an integer, are eqivalent.

$(\frac{n_i\omega}{c})^2 = k_\parallel + k_\perp$, the refracted and reflected waves will have a frequency ω[5] and wavevector $(k_\parallel + \frac{2\pi l}{a}, k'_\perp)$ for any integer l and some $k'_\perp$ [7]. For l=0 this will be the ordinary reflected wave with equal angle of incidence and reflection [16]. For $l \neq 0$, frequency dependent diffractive reflections can occur. Conservation of frequency then yields:

$$k'_\perp = -\sqrt{n_i^2\omega^2/c^2 - (k_\parallel + 2\pi l/a)^2}. \tag{2.14}$$

For this wave to be propagating, $k'_\perp$ has to be real, since imaginary $k'_\perp$ yields evanescent fields that decay exponentially away from the PC. Writing $k_\parallel = \omega$ $\sin(\theta)n_i/\mathrm{c}$ and requiring real values of $k'_\perp$, eq. 2.14 yields:

$$\frac{\omega a}{2\pi c} > \frac{l}{n_i(1 + sin\theta)}. \tag{2.15}$$

The diffracted orders start at glancing angles ($k'_\perp = 0$), and move towards the specular angle θ as ω increases. Increasing orders, i.e. increasing l, will be reflected closer to the interface.That is, if ω is large enough to allow several diffraction angles, the lowest diffraction order, i.e. l=1, will be closest to the specular angle, while the highest diffraction order will be at a more glancing angle, as can be seen in figure 2.8. This property is what makes the PC so attractive as a backside reflector for solar cells, as this effect can be used to greatly increase the pathlength of the photons within the solar cell, and hence their probability of being absorbed.

[5] Conservation of frequency

2.2 The inverted opal

The inverted opal is a PC that exhibits a complete photonic bandgap, and is, as the name implies, an inverted version of the opal.

Natural opals consist of close packed silica spheres with submicron silica spheres in a matrix of silica-water [7]. Similarily to a fcc structure of close packed dielectric spheres, they do not exhibit a complete PBG [7][6]. These opals do however exhibit a band gap in certain directions for certain energies, giving the opals their characteristic brilliant appearance. Although the opal itself does not have a complete PBG, a **synthetic opal**[7] can be used as a template to make an **inverted opal** [7], which does exhibit a complete PBG [8, 14].

A complete BG is essential when one wants to utilize a PC as a rear reflector in solar cells, as the light will be incident on it from a large range of angles. This is due both to the movement of the sun across the sky, but also due to refraction of the light upon entering the cell, which again can be modified by surface texturing.

To make an inverted opal, one first fabricates a synthetic opal that will be used as a template. This is described further in the next section. The opal can then be inverted by filling in the gaps between the spheres with a suitable dielectric material, such as silicon, and subsequently removing the spheres with a selective etch. This will leave an inverse opal; an opal structure of air-holes in a silicon lattice. Before filling in the gaps, the opal needs a sintering step to make the spheres adhere to each other. This step will give rise to small "air-tubes" between the airholes of the inverted opal, resulting in an interlacing of an air lattice and a dielectric lattice. The inverted opal that will be attempted made in this master thesis, will be grown in the [111] direction on a silicon substrate. As a consequence, the reflective properties of the structure must be measured and simulated in this direction to be of interest. This direction corresponds to the ΓL direction in figure 2.10. The

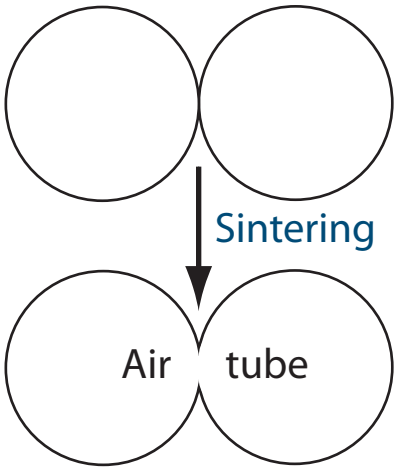

Figure 2.9: Sphere fused together after sintering, resulting in an air tube after invertion.

[6]The silica spheres of an opal can be arranged in a fcc lattice, but are most often random hexagonally close packed (rhcp).

[7]A synthetic opal can be made with a fcc structure, which is more favorable than natural opals that usually have a rhcp structure

figure shows the calculated bandstructure for the inverted opal with a dielectric contrast of 13, which corresponds to the dielectric constant of silicon at λ=930nm [17]. As can be seen, the inverted opal has a complete BG for frequencies between 0.76 and 0.8 (yellow band in figure 2.10), and partial BGs in the γL direction just below 0.7 (green band) and between 0.41 and 0.51 (red band). All frequencies in units of $\frac{\omega a}{2\pi c}$.

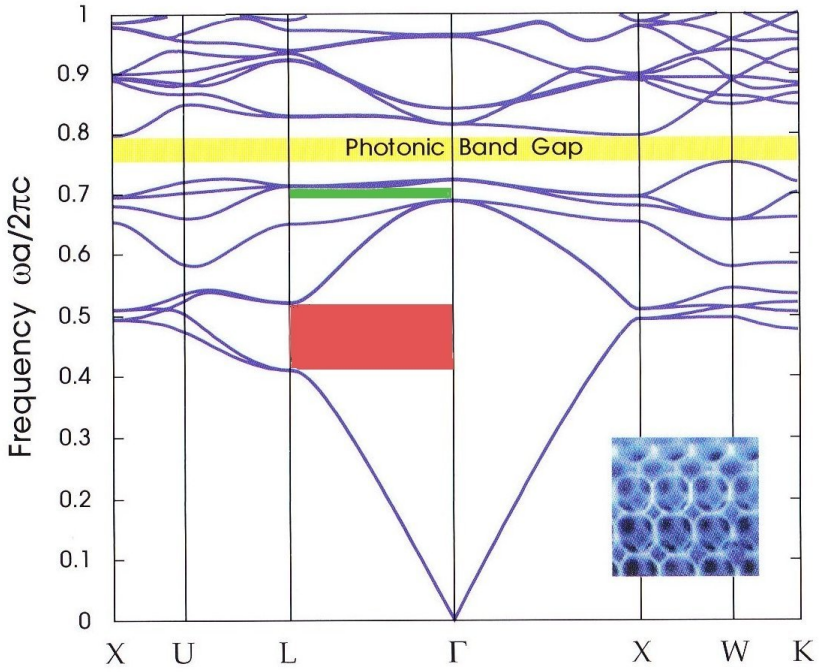

Figure 2.10: Band diagram of the inverted opal, calculated for a dielectric contrast of 13. Figure taken from [7].

One of the differences between the inverted opal and other 3D PCs, is that its complete BG appears between the 8th and 9th bands instead of between the 2nd and 3rd bands. One effect of this is that the inverted opal structure is much more sensitive to structural defects. This was shown with simulations by Li and Zhang [18], indicating that variations in sphere size and sphere displacements in the order of 5% of the sphere radii could completely close the bandgap. Although the complete BG is quickly closed, the lowest partial bandgap is only slightly affected by these defects. More on the effect of defects on PCs in chapter 2.4.

The inverted opal that is the goal for this master thesis, is intended as a rear reflector for solar cells, both because of its reflective properties and that it is potentially easy and cheap to make. The structure has been simulated for this use previously by Biel et al. and Bermel et al., using 6 and 8 layered structures

respectively, yielding satisfactory results.

2.3 Crystal growth

Several self-assembly methods have been used to fabricate synthetic opals from spheres in a solvent. The three most commonly used methods/mechanics, are: self-assembly by slow **sedimentation** of spheres [19, 20], **drying of a colloid**[8] suspension on a solid (or fluid) substrate [22–25] and the **exploitation of capillary forces** [8, 26–31].

In the **sedimentation** method, gravity is the driving force towards the fcc structure. Most of the reported opals of good quality made with this method, have been made on a timescale of months [19], making it a very slow process. The method also introduces a high amount of defects [8, 32] and gives very little control of the number of layers and morphology of the top surface [29]. Due to the fact that the method is gravity driven, there is a narrow range of sphere sizes that can be used with this method: for silica spheres this method is reported to be limited to spheres with a diameter between 300 nm and 550 nm (smaller spheres descend too slow, whereas larger spheres descend too fast) [33]. This range should be different for polymer spheres with a smaller mass density. Although the size range is relevant for the PCs pursued in this work, the very long times needed for sedimentation and the reportedly poor surface layer control makes this method unattractive.

Another method that's been used to make opal films, is the **drying of a colloidal suspension** on a hydrophilic substrate [24]. This is however a more complex process than pure sedimentation. When a colloidal is deposited on a hydrophilic substrate and left to dry, there will be a tendency of the spheres to accumulate at the edges. The reason for this, is that the evaporation rate of the solvent is higher here, resulting in a capillary flow of solvent from the center toward the edge (figure 2.11) to compensate liquid. This flow will bring with it more spheres. However, depending on sphere size and mass density of the spheres, this process will have to compete with sedimentation. If the spheres sediment too fast, the particle flow will only happen in the beginning, resulting in the formation of an outer ring disconnected from the center (figure 2.12). Whether the spheres sediment fast or slow, the capillary flow will result in an accumulation of spheres at the edge. The spheres at the edge will crystallize, beginning at the contact line as seen in figure 2.11.

Close packed monolayers of spheres can also be formed by **attractive lateral capillary forces**. These forces appear between spheres that are partially immersed in a liquid/solvent on a substrate [32] and spheres floating on a liquid surface. If the necessary conditions are met, these forces can cause the spheres

[8] A colloid is a mixture where one substance (spheres) are evenly distributed in another substance, i.e. water [21].

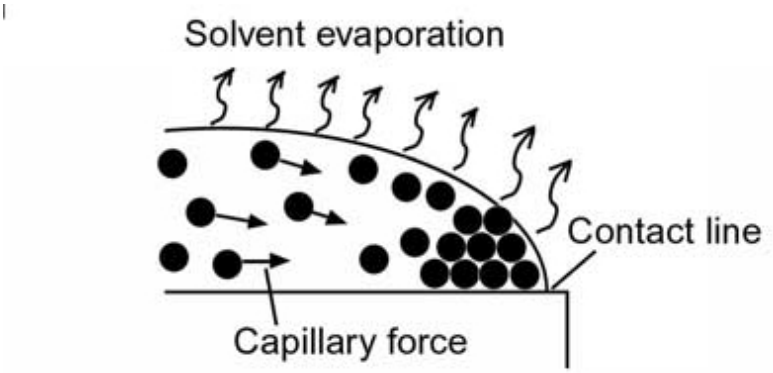

Figure 2.11: The figure shows capillary flow of particles due to higher solvent evaporation rate at the edges of a drop. This will result in an accumulation of spheres at the edges. Figure taken from [24].

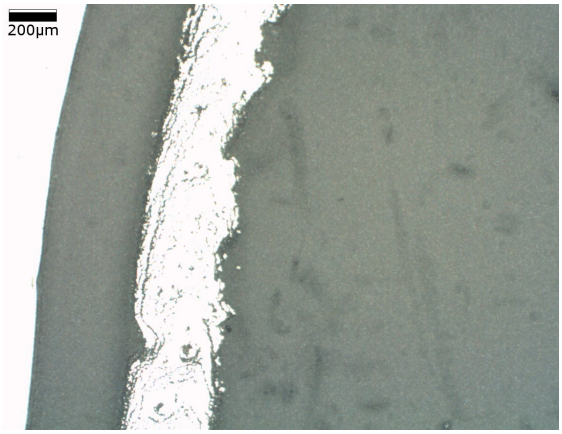

Figure 2.12: A microscope image showing a drop of water and spheres that has been left to dry on a glass substrate. Shows the outer ring disconnected from the central disc. Image taken from the preceeding project [34].

to be pushed together so that they nucleate into ordered two-dimensional layers, i.e. a monolayer of spheres. The capillary forces appears due to a deformation of the liquid surface, and the larger the deformation the greater the force. The mechanisms leading to the surface deformation are not the same in the two cases however.

For particles floating on a liquid surface, the deformation is due to gravitational forces. As illustrated in figure 2.13, the particles will attract each other when the product of the sines of the menisci slope angles, Ψ, are positive. When this is the case, the surface is deformed in such way that the gravitational potential of the particles will decrease when they approach each other. For identical particles, these forces will therefore always be identical (equal sign of Ψ means that the product of their sines always will be positive).

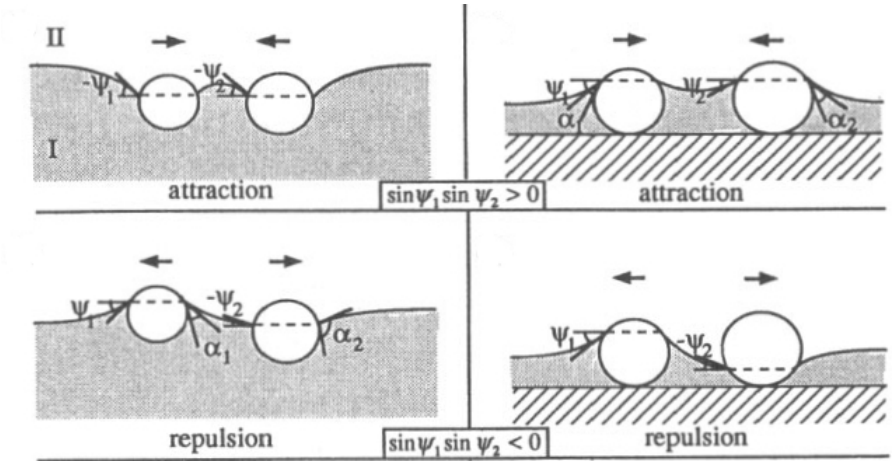

Figure 2.13: Figure showing attractive and repulsive floatation and immersion forces between spheres. α_k and ψ_k are the contact and meniscus slope angles respectively. The menisci slope angle, referring to the figure, is the angle between the slope of the liquid at the contact point with the spheres and the horizontal. Contact angle is the angle between the slope of the liquid at the contact point and the tangential at the contact point. For the forces between the spheres to be attractive, the product of the sines of the menisci slope angles have to be positive. Figure taken from [30].

In the case of particles partially immersed in a liquid on substrate, the deformation of the surface depends on the surface properties of the spheres. Related to figure 2.13, the product of the sines of the menisci slope angles, Ψ, must be positive for the forces to be attractive, as for the floating particles. Ψ will be negative for hydrophobic particles and positive for hydrophilic particles. Therefore, as long as the particles have the same surface property (hydrophobic, hydrophilic), these forces will be attractive.

Nagayama et al. showed that the magnitude of the attractive forces vary in the two cases, as they have different physical origins. For spheres floating on a liquid, the forces will be proportional to R^6, and will be overcome by the thermal energy when the radii becomes less than $10\mu m$. This is because the spheres become too light to cause any substantial deformation of the surface (mass density of the spheres were $1.05gcm^{-3}$). For spheres partially immersed in a liquid on a substrate, the forces will be proportional to R^2 and can be significant compared to the thermal energy for sphere radii down to 10 nm. This can happen when the liquid film in which the spheres are partialy immersed becomes thinner, e.g. by evaporation. When the liquid film becomes thinner, the deformation of the surface between the spheres increases (figure 2.14), and the attractive forces becomes stronger.

(a) (b)

Figure 2.14: Change in water surface deformation between two spheres partially immersed in a water film with a change in film thickness as the water evaporates.

Using attractive capillary forces in the way described above can prove well suited for making monolayers of spheres, as was shown in the preceeding project [34], and as will be shown in this thesis. Forming multilayer structures does prove more difficult, but other methods have been sucessfully used for this purpose [26, 28, 29, 31].

The methods used exploits the fact that when a substrate is placed vertically in a suspension of spheres, the spheres will spontanously form monolayers and multilayers on the substrate at the meniscus[9] (figure 2.15) that forms at the substrate-gas-suspension contact point. As this meniscus moves along the substrate, either by solvent evaporation as used by Colvin et.al and McLachlan et al., or by substrate withdrawal as used by Nagayama et al. and Gu et al. [29], ordered layers of spheres in the cm range can be deposited.

Before continuing, something should be said about surface tension and the formation of the meniscus at a substrate-gas-liquid interface. In the following it will be assumed that the liquid is water, which is the solvent used in the suspensions mentioned, and that the gas is air.

[9] A meniscus forms because the molecules in the liquid have a stronger attraction to the substrate than each other [35].

Surface tension can essentially be said to be the force that keeps a droplet of water together when it's placed on a substrate. The reason why the water doesn't form a thin film on the substrate is that the molecules in the water attracts each other. In the bulk of the droplet these forces balance each other, but at the surface the pull towards the bulk of the drop will be greater than the pull towards the surface. This results in a minimization of the area of the water/air interface, and the water forms a droplet.

When a hydrophilic substrate is partially submerged vertically in water, the water molecules will have a stronger attraction towards the substrate than to the water bulk. This will result in the water being pulled upwards along the substrate, forming a meniscus/water film.

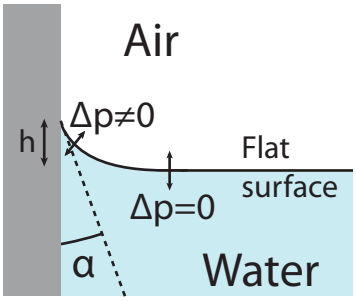

Figure 2.15: A menisci formed at the substrate-air-water interface. Δp is the pressure difference between the two sides of the water surface, h the height relative to the flat surface to which the meniscus reach on the substrate, and α is the contact angle between the water surface and the substrate.

How high up on the substrate the water is pulled from the flat surface (see figure 2.15), will depend on the surface tension constant γ, and the contact angle α. When the meniscus forms at the substrate-air-water interface, the water surface will curve towards the substrate. This curvature will set up a pressure difference (proportional to the inverse of the radii of the curvature) on the different sides of the meniscus, i.e. the pressure just beneath the surface will be lowered with respect to the air side, and therefore to the water bulk [36]. As the pressure is lower in the meniscus than the water bulk, the water in the meniscus will be raised until a compensating hydrostatic pressure is reached. The height to which the surface will rise, is given by [36]:

$$sin\alpha = 1 - \frac{\Delta\rho g}{2\gamma}h^2, \tag{2.16}$$

where $\Delta\rho$ is the density difference between the water and its surroundings (i.e. air), g the gravitational acceleration and h the height to which the surface rises above the flat surface. From this equation it becomes clear that for hydrophilic surfaces, where α can be very small, such liquid wetting films (which the meniscus essentially becomes "far" from the flat surface) can extend quite high up on a substrate.

Now, let us return to the case of close packed spheres on a vertical substrate. There are two main steps involved in the close packing of spheres; a convective flow of spheres from the suspension towards the water film due to evaporation of water from the surface of the water film, and the interactions between the spheres that pack them together (including lateral capillary forces). This is illustrated in figure 2.16.

When water starts to evaporate, a pressure gradient appears from the bulk suspension towards the meniscus due to a thinning of the wetting film and increased lateral capillary forces between the spheres in the wetting film. This pressure gradient causes an influx of water and spheres. The water flux compensates for the water that evaporates from the menisci and the array of hard packed spheres, and upon reaching the edge of the array will press the spheres towards the array while flowing through its pores. The spheres which accumulates at the edge of the array, tend to pack themselves together in a fcc structure. Exactly why is not known, but one hypothesis will be presented at the end of this section.

The above explanation assumes that the array growth is in progress, but does not explain the growth start. When the substrate is first put into the suspension, a wetting layer forms which, due to the hydrostatic pressure, becomes thicker and thicker towards the suspension bulk. This inclination with the substrate sets up capillary forces which forces spheres with a diameter larger than the film thickness out of the film. In that case, the lateral capillary forces between the spheres can not initiate the growth process, i.e. create a pressure difference. However, the evaporation from very thin wetting films (less than 1 μm) can cause a pressure difference due to an increase in the disjoning pressure [10]. The pressure difference thus created produces a water influx to the water film which brings with it spheres. These spheres can then be stored in the film, and the growth can start.

Colvin et al. made use of these principles, but using solvent evaporation rather than substrate withdrawal, and found that the film thickness could easily be controlled by particle size and particle volume fraction in the suspension. Gu et al., which followed the method described above more closely, also reported this, but also that withdrawal speed could be used to tailor film thickness, although not as a linear relation. A saturation thickness seemed to be reached, depending on the volume fraction of spheres. Another important parameter is the temperature during opal growth, which McLachlan et al. showed to affect the opal quality extensively (with the method using solvent evaporation to move the meniscus along the substrate). The ideal temperature was experimentally found to be approximately 65°C.

As a last note: why exactly does the spheres tend to arrange themselves in a

[10]The disjoning pressure appeares between two parallel interfaces due to van der Waals interactions. This pressure increases with a decrease in the separation of the interfaces [37]

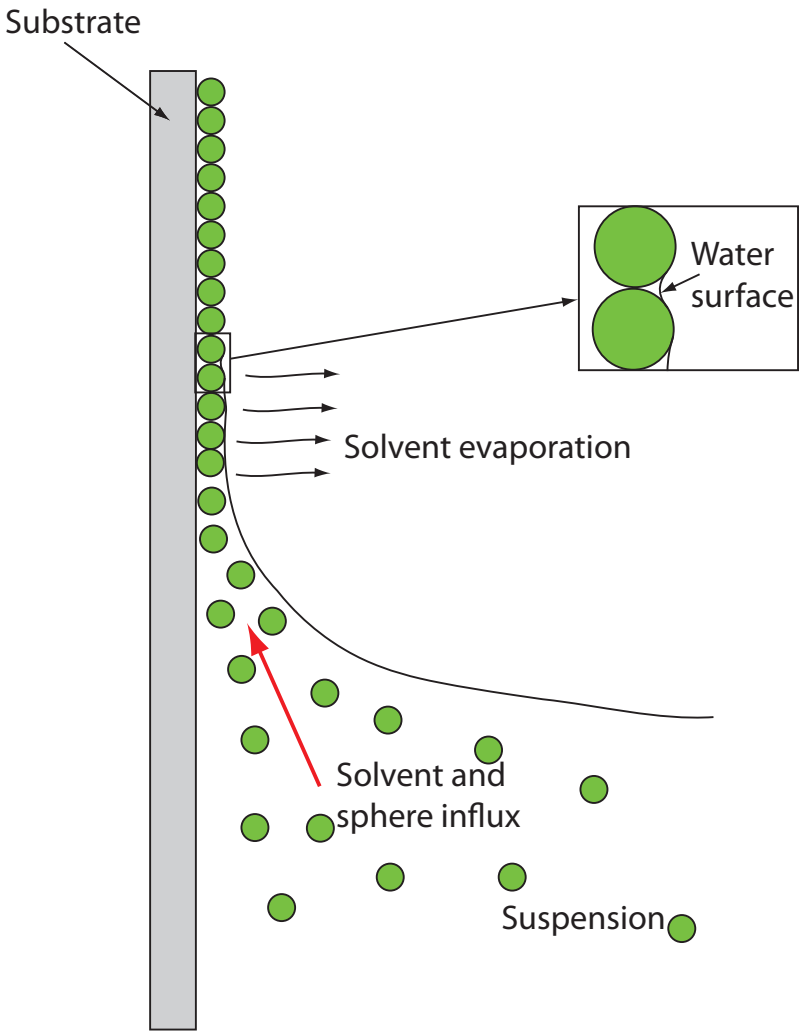

Figure 2.16: Crystal growth on a substrate partially submerged vertically in a colloid. As the solvent evaporates from the meniscus and the menisci between the spheres in the water film, a pressure gradient arises between the bulk of the solution and the meniscus, causing a flow of water and spheres towards the meniscus. These spheres will be packed together by the water flow, and the capillary forces between the spheres.

fcc structure with the method described above? The energy difference between fcc and hcp is extremely small, only about $\leq 10^{-3} k_B T$ per particle [38]. Even so, the opals formed within a few hours (with the method described above) have a greater tendency towards the fcc structure [32] than sedimented opals, which form over a time span of months. Norris et al. theorized that it was because, at least in part, of the way the water flowes through the pores between the spheres.

As the spheres are carried to the leading edge/face of the growing opal by the water flow, the spheres are carried into the niches between the spheres of the opal. When the spheres is carried into these niches, the Stokes viscous drag [39] on the spheres increase so they get lodged [32]. The theory presented by Norris et al. was that if the flow through some of the niches is stronger than through the others, it could guide the opal growth. As seen in figure 2.17 there are essentially two kinds of niches, **clear** and **obstructed**. According to Norris et al. it has been shown that the flow through the clear niches is 33% higher than through the obstructed niches, irrespective of the structure under the two first layers of spheres. In the best case where the spheres lodge only into the clear niches, a fcc packing will be obtained. Even though this may not fully be the case, there will be a preference towards the fcc packing.

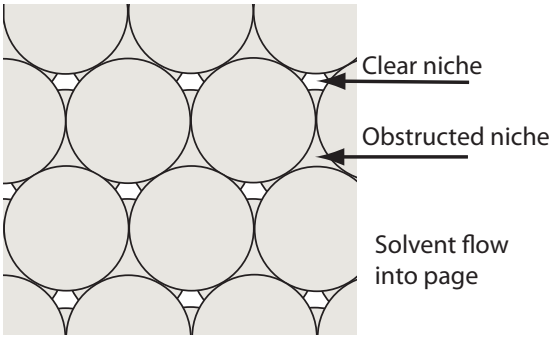

Figure 2.17: Pointed out in the figure, are an obstructed and an unobstructed niche in an opal. The solvent flow is 33% more likely to flow through the unobstructed niches irrespective of the layers below. This leads to a preference for the ABCABC... stacking order, i.e. the fcc structure.

2.4 Defects and their effects on a PC

When an opal is made using self-assembly, there will unavoidably be defects present. Referring to the opal template, these can be in the form of point defects, line defects and planar defects.

The incorporation of point defects in an opal structure can be in the form of missing spheres or by spheres of deviating size. In a PC, point defects, in the form of missing or smaller spheres, will introduce localized states within the crystal [7], but will not noticably disrupt the overall behaviour of the PC [40]. However, the appearance of bigger spheres can be destructive, as they will introduce short-range disruption of the crystal lattice, as well as dislocations and stacking faults.

The dislocations are a class of line defects, and can be either *edge-* or *screw* dislocations. Edge dislocations can be visualized as a termination of a crystal plane within the lattice (figure 2.18(a)). Screw dislocations can be visualized as follows: make a cut into the crystal, and shift one side of the cut a lattice constant relative to the other (figure 2.18(b)).

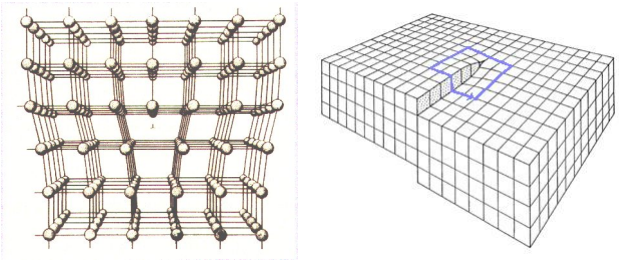

(a) Edge dislocation. (b) Screw dislocation.

Figure 2.18: Two types of line defects, edge and srew dislocation. An edge dislocation, figure **a**, can be visualized as a termination of a crystal plane within the lattice. A screw dislocation, figure **b**, can be visualized by making a cut into the crystal, and shift one side of the cut a lattice constant relative to the other. Figures taken from [41].

Palacios-Lidón et al. [40] have done a study of the effects of these defects on a PC. By reflectence measurement they found that the characteristic Bragg reflection peak, corresponding to the bandgap of the PC, broadened and became flattened. These effects became more pronounced with increasing amounts of defects and increasing size of the the defect spheres. At some point, it was no longer useful to talk about a crystal. This happened when the defect concentration was so high that effects of the individual defects interfered with each other. For lower concentration of defects, and spheres deviating only a "little" in size (33% in their experiments), the spheres were easily incorporated into the crystal lattice with only

minor effects on the Bragg reflection peak. For the spheres used in this project, the size deviations was 2.5%, as reported by the producer (490nm with a mean deviation of 12nm).

In this master project, the structures that are expcted to be grown, is the fcc structure, which have a ABCABC... stacking order, and the hcp structure whcih have a ABABAB... stacking order. The stacking order is referenced to figure 2.19. When growing such structures, stacking faults may occur, usually in the growth direction, so that a random error in layer sequence is introduced, e.g ABCABABC.... Vlasov et al. [19] have made a study of the effect of these defects on the optical properties exhibited by PCs, and found that they caused a broadening and flattening of the Bragg reflection peak for all incident angles. This effect was greater for light not at normal incidence to the growth direction of the crystal, and was accompanied by a shift of the peak to higher frequencies for increasing angles. A structure with a lot of stacking faults, i.e. neither being fcc or hcp, is called random hcp (rhcp).

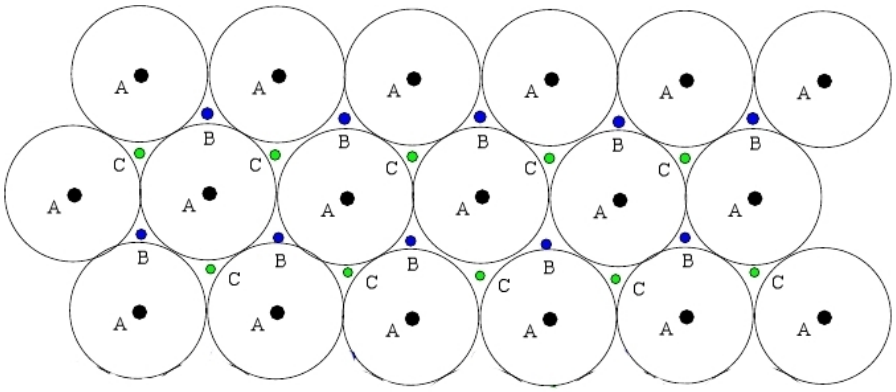

Figure 2.19: Circles represent bottom layer of spheres. The next layer will have spheres with centers above the points marked B (*blue dots*), and the third layer will have spheres with centers above the points marked C (*green dots*). This stacking structure will then be repeated in sequence, ABCABC..., for the fcc structure. For the hcp structure, the stacking order is ABABAB...

Chapter 3

Experimental

In this chapter the various methods used to fabricate opals from a suspension of spheres will be described. Theory on plasma enhanced chemical vapour deposition (PECVD) and the scanning electron microscope (SEM) will also be given, followed up by the theory behind the simulation software MEEP. MEEP was used to simulate the reflection properties of the inverted opal, the PECVD to deposit silicon in between the spheres of the opal templates, while the SEM was used to obtain images of the samples in the various stages of the fabrication process.

But before that, the equipment list:

3.1 Equipment list

Opal growth equipment

- *Reaction vessel*: used with opal growth method #2, where a solution of spheres were drained from the reaction vessel to acheieve meniscus translation along a substrate vertically placed in the solution
- *UltraSonic bath*: used to break up aggregates in the solutions prior to use
- *Oven*: Used in method #3, as explained below
- *Glass vials* of different sizes used as solution containers in growth methods #2&3, soulution mixing, pipette cleaning etc.
- *Pipettes*: solution, ethanol and water handling
- *Peleusball*: help with liquid uptake and dispensing with a pipette
- *Tweezers*: handling substrates without contaminating them
- Loads and loads of DI water
- *OptiClear*: used to remove unwanted contaminations from the substrates used in method #2&3 before being used
- *Acetone*: used to remove OptiClear from samples

- *Isopropanol*: used to remove any remaining Acetone and to clean substrates used in method #1
- *Clamps*: used to hold substrates vertically in a solution

Inversion equipment

- *Oven*: used to sinter the spheres, i.e. heating them up to softening temperature and then cooling them, resulting in better adhesion between spheres
- *Plasmalab System 133 PECVD*: used to fill in the gaps between the spheres with silicon
- *Oven*: used to remove the spheres at 600℃

Characterization equipment

- *Zeiss light microscope*: Used for optical imaging of samples
- *ALC13 digital camera*: mounted on the light microscope for live transfer of the microscope image to a computer
- *Hitachi S-4800 Field Emission SEM*: Used to obtain image of samples made with PS spheres, as theses sphere were too small to be imaged optically

Software

- *MEEP*: used to do reflection simulations of inverted opal structures
- *Matlab*: plotting of reflection data
- *Adobe Illustrator*: Used to make figures
- *Google Sketchup*: Used to make figures
- *Gimp*: Image editing
- *Adobe photoshop*: Image editing

Miscellanous equipment

- Too large lab coat and a pair of snuggly fitting clogs
- *Texwipe*: paper tissue made for clean-room use
- *vinyl gloves* to avoid unnecessary contamination

3.2 Opal growth

Opal growth was attempted with two different kind of spheres in the master work. These were the Ugelstad spheres used in the preceeding project, which was obtained from Conpart, and polysterene (PS) spheres obtained from Bangs Laboratories. More detailed information about the spheres is listed in table 3.1.

The important difference between the two kind of spheres, is the diameter. For the inverted opal to exhibit a complete bandgap and/or strong reflection in the

Sphere type	Ugelstad	Polysterene
Diameter	$3.27\mu m$	490nm
Diameter deviation (mean)	NA	12nm ($\approx$2.5%)
Refractive index	NA	1.59
Mass density	1.16 g/cm^3]	1.05[g/cm^3]
Surface property	Slightly hydrophobic	Hydrophobic

Table 3.1

near-visible range of the IR-spectrum, spheres with a diameter of less than $1\mu m$ is needed. For this reason PS spheres with a diameter of 490nm was purchased to replace the Ugelstad spheres, which had a diameter of $3.27\mu m$. As will be explained below, the change in spheres also resulted in a change of growth method. The monolayers of spheres grown with the Ugelstad spheres, were made using method #1, while methods #2 and 3 was used for the PS spheres. Note that that the mean diameter deviation of the PS spheres is less than 5%, which was the diameter at which the complete BG of the inverted opal would close [18], as mentioned in the theory.

3.2.1 Opal growth method #1: Diffusion

In the preceeding projectwork, a crystalline monolayer was grown by diffusing Ugelstad spheres onto a water film situated on a silicon wafer, and subsequently letting the water evaporate. This was done with the water film and the reservoir of (ethanol containing) sphere solution on the same wafer, adjacent to each other. When the water film dried, the wafer was partially covered with a polycrystalline monolayer of spheres, connected to the dried reservoir of spheres, as can be seen in figure 3.1. It should be noted that the shape of the water film prior to being covered by spheres, closely matches the shape of the monolayer of spheres.

During the experiments with this method in the project, it was noted that a small contact point between the reservoir and waterfilm yielded a better result, i.e. the crystals in the monolayer became larger and the amount of defects and excess spheres on top of the layer decreased. This, together with that fact that it was desired to achieve a wafer sized structure, motivated the development of a slightly different method.

Instead of having both the solution with spheres and the water film on the same wafer, the wafer was covered entirely with a water film. The sphere solution was then placed at the corner of a piece of a wafer, adjacent to the wafer covered with a water film (figure 3.2). This corner was then brought into contact with the water film, allowing for diffusion. This way the entire water film was covered

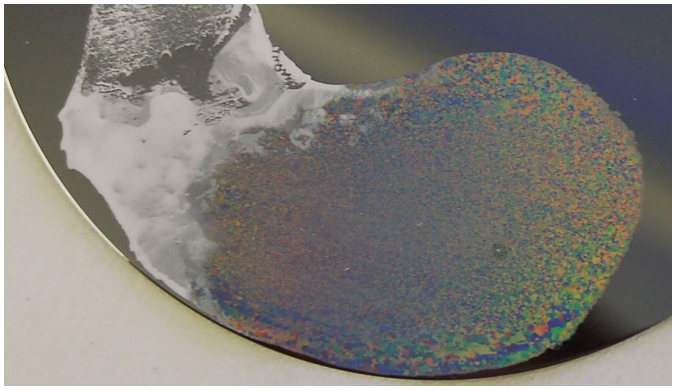

Figure 3.1: Monolayer of Ugelstad spheres obtained in the projectwork. The irridiscent nature of the monolayer can be clearly seen. White areas are the dried remains of the reservoir of spheres.

with spheres, and subsequently almost the entire wafer could be covered with a monolayer of spheres.

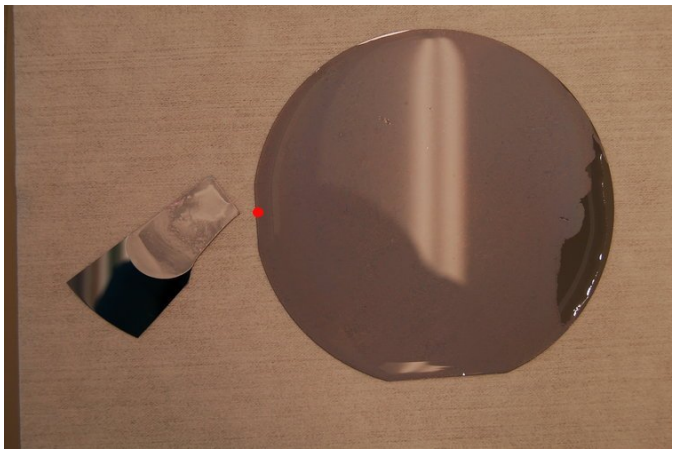

Figure 3.2: Image shows the water covered wafer after diffusion of spheres, and the reservoir wafer piece. As can be seen, almost the entire water film has been covered with spheres. The two wafers were connected at the red point

3.2.2 Opal growth method #2: Draining

This method was developed as method #1 proved unsuited for the PS spheres, and is based on methods reported in literature [26, 29] which utilize the fact that submicrometer spheres tend to be packed together in a fcc structure at a slowly moving meniscus, as explained in chapter 2.3. Previously, the movement

of the meniscus along a (vertical) substrate has been achieved by slowly pulling a substrate out of a solution of spheres [26, 29] and by solution evaporation [31]. The method developed here takes a slightly different approach: a solution of spheres is placed in a reaction vessel with a drawl at the bottom. The substrate onto which the spheres are to crystallize, is placed vertically in the solution, which is then slowly drained from the reaction vessel. A simple schematic can be seen in figure 3.4(a)

The main strength of the method is its simplicity, which also is its weakness. By simply draining the solution from the vessel, the speed at which the meniscus moves along the substrate will be getting slower as the amount of solution becomes less. This is because the pressure at the valve gradually decreases as the amount of solution above it decreases. In addition, adjusting the draining speed with the valve is not very precise, especially so when the speed of the meniscus is on the order of a few hundred nm a second. To get some control over the initial draining speed, adjustments was first done with only water, before the solution was added to the vessel and the experiment was started. It was assumed that the draining speed would be slightly lower for the sphere containing solution than for water, so the speed was adjusted to a slightly higher speed (for water) than desired. An image of the setup can be seen in figure 3.3

3.2.3 Opal growth method #3: Evaporation

The third method that was used, was also based on methods reported in literature [31] and was even simpler than method #2. In this method, the translation of the meniscus along the (vertical) substrate was achieved by solvent (water) evaporation. A substrate was placed vertically in a solution of spheres, and the setup was placed in a pre-heated oven. The oven used in the experiments here however was a bit inaccurate, with the actual temperature being within 2℃ of the chosen. Also, the built in thermometer did not match the actual temperature in the oven, with a discrepancy of 10-15℃ (varying with the set temperature). For this reason, another thermometer was placed in the oven and used for temperature determination. A simple schematic of the setup can be seen in figure 5.16.

3.2.4 Substrate and solution preparation

All the handling of solutions mentioned in this section was performed with pipettes, unless otherwise specified.

The substrates used with method #1 were cleaned with a tissue (Texwipe) and isopropanol, and then rinsed with deionized water (DI water). A water film was added to the substrates with the use of a pipette. Solutions used with this method

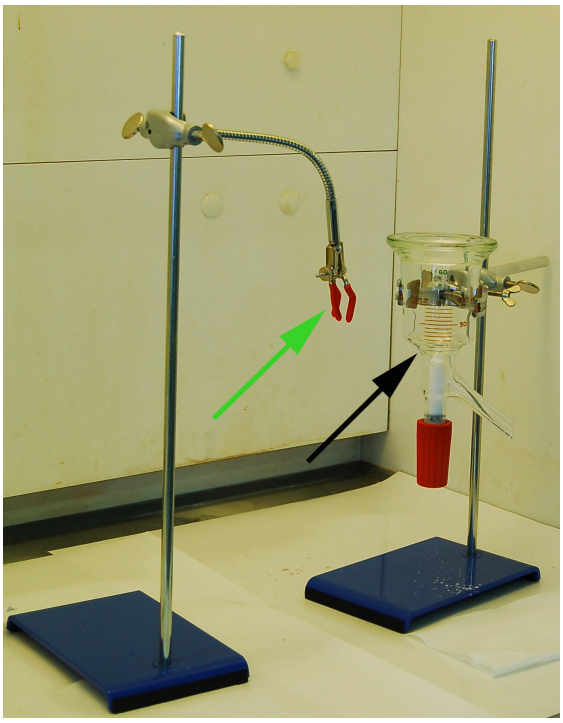

Figure 3.3: An image of the setup for opal growth method #2. The black arrow indicates the reaction vessel, while the green arrow points out the clamp used to hold the substrate vertically in the vessel.

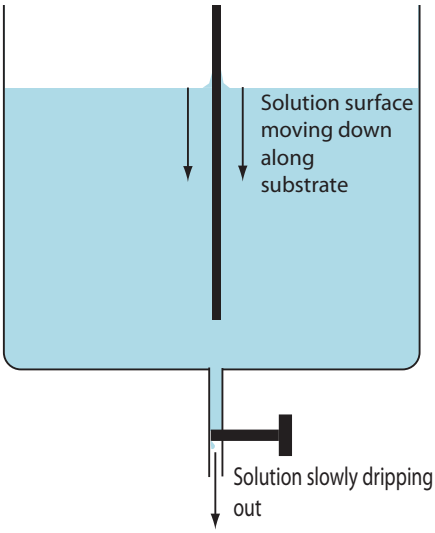

(a) Method #2: Draining

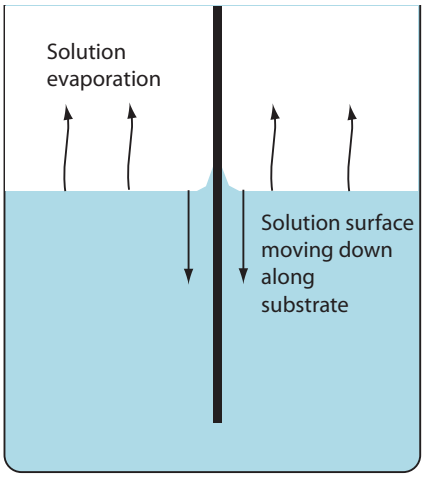

(b) Method #3: Evaporation

Figure 3.4: Schematics of method #2 and #3. With method #2, the movement of the meniscus was achieved by slowly draining the solution out at the bottom of the reaction vessel, while in method #3 the solution solvent was evaporated by placing the setup in an oven.

were mixed together in small glass vials, and then dispensed on the reservoir wafers. All glass vials were thorughly cleaned with DI-water.

For method #2 and #3, the substrates were prepared with the following process:

- 5 minutes in OptiClear
- 5 minutes in acetone to remove OptiClear
- 5 minutes in isopropanol to remove any remaining acetone

Before being diluted with water to obtain the desired solution, the spheres used with method #2 and #3 were placed in an ultrasonic bath for 5 minutes to break up any possible aggregates that may have formed. Spheres and DI-water were then mixed together as desired, and then transferred to the reaction vessel. A substrate was held vertically in the solution, using the clamp indicated with a green arrow in figure 3.3. The solution was then slowly drained from the vessel. The entire setup was placed in a temperature controlled laboratory at 20.5°C±1°C. To determine the speed of the meniscus along the substrate, the height of the surface in the

reaction vessel was measured at different stages of the growth process. Meniscus speed was then calculated as meniscus speed = height difference/time.

Thereafter the solution was collected in a glass vial, and added more DI-water. This solution was placed in an ultrasonic bath for 5 minutes to break up aggregates, before being used with method #3. The reason for this reuse was the limited suply of spheres. More DI-water was added to reduce the concentration of spheres, because method #3 produced thicker films than method #2, as indicated by initial attempts with the method.

3.3 Opal inversion

Inversion was only done for the opals made of PS spheres, and was done in three steps: (1) sintering the opal, (2) filling in the gaps between the spheres with silicon and (3) removing the spheres.

Sintering was done in an oven at 95℃, the temperature at which the PS spheres begin to soften, to make the spheres adhere better to each other. The gaps between the spheres in the opal was then filled in with silicon, using a *plasma enhanced chemical vapour deposition* (PECVD) process at 90℃ and with a pressure of 300mTorr. This process was allowed to run for 1.5 hours. Lastly the spheres were removed by calcining the samples for 2.5 hours at 600℃ in an oven. At such high temperatures, the spheres dissolves and evaporates, leaving only the silicon framework on the substrate. Silicon has a melting point of 1414℃[**?**] and softening temperature of just above 700℃, and should stay intact.

About the runtime for the PECVD process. The thought was to deposit enough silicon to fill in the gaps for about 8 layers of spheres. It wasn't expected that the method would perfectly fill in the gaps between the spheres, so a filling fraction of 0.2 (as opposed to 0.26 for a perfect filling) was assumed. 8 layers of spheres are approximately $3.3\mu m$ high, but with a filling fraction of 0.2, approximately 650nm silicon should be needed ($0.2 \cdot 3.3\mu m$). The height of 8 layers was calculated as 2·sphere radius+7·($layerseparation = (sqrt(8/3)$·sphere radius). In the standard process used by IFE, which is performed at 230℃, 650nm of silicon is deposited after 1 hour. It was expected that the deposition rate would be slower at 90℃, hence the longer time.

3.3.1 Plasma Enchanced Chemical Vapour Deposition

PECVD is a type of *chemical vapour deposition* (CVD) process, in which a solid film of a material is deposited onto a substrate through chemical reactions of a gas mixture, with the help of a RF induced plasma. The PECVD that was used in this master thesis, was the Plasmalab System 133 PECVD.

In a standard PECVD setup, two parallel plates are placed inside a reaction chamber. The substrate onto which the film is to be deposited is placed on the grounded bottom plate (anode), while a RF source is applied to the top plate (cathode). Precursor gases that are situated in between the plates, will then be bombarded by electrons, emitted from the cathode and generated from ionization of the precursor gases themselves. These electrons are accelerated by the applied electric field, and when they've gained a high enough energy, they can elevate the gaseous molecules to an elevated electronic state. These molecules can relax in four different ways; either by (1) photon emission, from where the plasma gets its characteristic glow, by a disassociation into (2) free radicals, (3) free radicals, positively charged ions and electrons or (4) free radicals and negatively charged ions. The free radicals are chemically very reactive atoms and molecules, i.e. they have unsaturated bonds, and are the primary reactants in the formation of the film. The electrons generated when the molecules relax, are important to sustain the plasma.

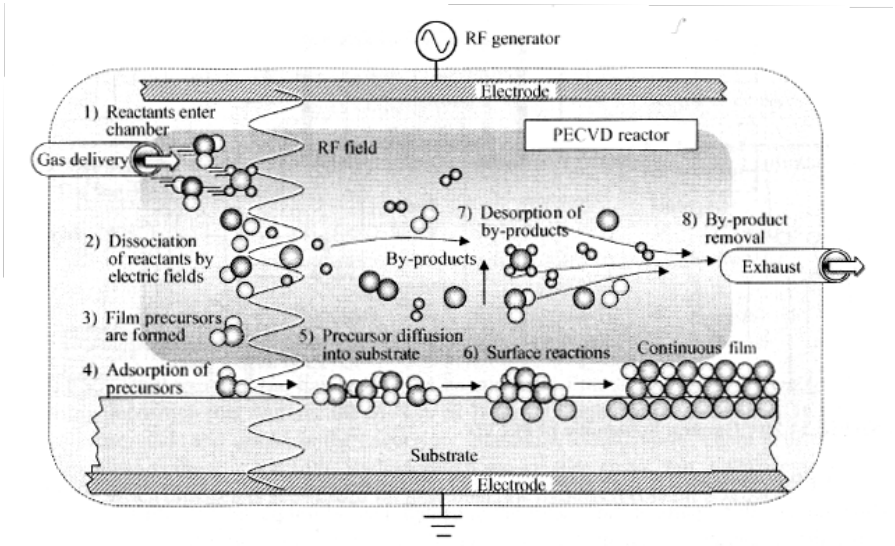

Figure 3.5: A schematic of the PECVD process. A gas is pumped into the chamber and is broken up in the plasma. At the surface, surface reactions with film precursors created in the plasma leads to a thin film on the substrate. By-products are removed by the gas flow thorugh the chamber.

In this process surface reactions leads to a developing film on the substrate, as well as several by-products. The latter do not adhere to the substrate, and can be removed from the chamber, together with the by-products from the disassociation process in the plasma, by the gas flow through the chamber. A schematic of the process can be seen in figure 3.5.

PECVD can be performed at low temperatures, from room temperature to 400℃(700℃with stainless steel electrode). The quality of the deposited films decrease with lower temperatures however, so the temperature range is usually specified as 100-400℃.

Some of the advantages of PECVD, are low processing temperature, good film adhesion to the substrate and high deposition rates.

3.4 Sample characterization

The samples, i.e. opals and inverted opals, were imaged at several stages in the fabrication process; after opal growth, sintering and calcination. For this an optical microscope and a SEM was used. The optical microscope was the only imaging tool used for the Ugelstad spheres, but for the PS spheres the SEM was also used as the resolution of the optical microscope wasn't good enough to distinguish the spheres from each other. It was however successfully used to determine the average grain size of the samples.

To determine the average grain size, an image of an area of approximately average quality was chosen and the grain size was then found visually using a length bar. The length bar was added to the images when they were exported from the imaging software connected to the microscopes.

3.4.1 Scanning Electron Microscopy (SEM)

The *scanning electron microscope* (SEM) used in the work on this master thesis, was the Hitachi S-4800 Field Emission (FE) SEM.

SEM is a non-contact metrology too that usually is considered to be nondestructive, and can, among other things, be used to image features on the nm scale. In the *secondary electron imaging (SEI)* mode, this is done by scanning the surface of a sample with an electron beam, and detecting the emitted inelasticly scattered secondary electrons[1]. The brief theory on SEM presented below, is based on the book "Semiconductor Manufacturing Technology" by Michael Quirk and Julian Serda **Ref** and on the SEM site on Wikipedia [42]. A simple schematic of a SEM can be found in figure 3.6.

The SEM consists of an electron gun that can emit electrons with energies ranging from a few hundred eV to some hundred keV, depending on imaging mode and the size of the features (i.e. smaller features requires electrons with higher energy, as they have a shorter wavelength assosiated with them). These electrons are gathered into a beam by the electron gun, but is further gathered by a set of

[1]Secondary electrons are generated as ionization products, and are called secondary because they are generated by other radiation, i.e. the incoming electrons [42]

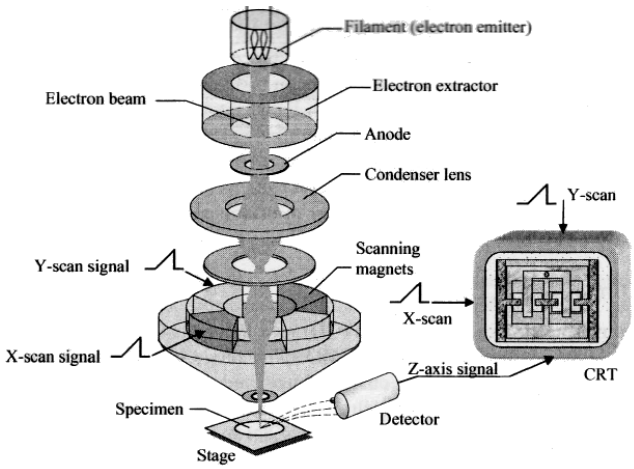

Figure 3.6: A schematic of a SEM. Electrons are emitted from a filament, and are gathered to a beam that can be scanned along a sample. In the SEI imaging mode, the secondary electrons (emitted from the sample surface) created by this beam are gathered and used to determine the topgraphy of the sample surface.

focusing elements to a beam with a spot size of 0.4nm to 6nm. The beam is then focused onto the sample by a cylindrical magnetic objective lens, and is scanned acrossed it with an electrostatic deflector. When the electron beam hits the sample, the electrons are scattered and absorbed (and in some cases transmitted). This happens in a volume which, depending on the electron energy and sample composition and density, extends 100nm - 5μm into the sample. A SEM can therefore also image parts of the sample lying below its surface. In the SEI imaging mode, secondary electrons emitted from the near surface of the sample, are collected and accelerated towards a scintillator that emits flashes of light. These flashes are then conducted to a photomultiplayer, the electrical output of which can be displayed as an image on a computer (after a necessary digitilizing step). The electrical output of the detection system is synchronized with the beam on the sample, so the image is essentially a distibution map of the detected signal intensity.

Nonconductive samples do however need special treatment before they can be imaged, especially so when the SEI mode is used. This is because the samples tend to become charged when they are scanned, resulting in scanning faults and other image artifacts. To prevent this, the sample can be coated with an extremely thin layer of a electrically conductive material, e.g. gold or carbon, and needs to be grounded so as to prevent electrical charging (naturally conductive samples are also grounded). The coating also improves the signal and the spatial resolution.

3.5 MEEP

The description of MEEP that will be given in this section is heavily based on the Wiki site of Steven G. Johnson, John D. Joannopoulos and Marin Soljačić [43] from MIT.

MIT Electromagnetic Equation Propagation (MEEP), is a finite-difference time-domain (FTDT) simulation software package used to model electromagnetic systems, e.g. reflection and transmission properties of a photonic crystal (PC). In short, this is done by evolving Maxwell's equations over time within a finite computational region. When using this technique, space is divided into a discrete grid and the fields are then evolved in time using discrete time steps. By making these steps increasingly smaller, many problems can be solved essentially exactly.

3.5.1 Maxwell's equations

The Maxwells equations which are used in the evolution of the fields in MEEP, are:

$$\begin{aligned} \frac{d\boldsymbol{B}}{dt} &= -\nabla \times \boldsymbol{E} - \boldsymbol{J}_B - \sigma_B \boldsymbol{B} \\ \frac{d\boldsymbol{D}}{dt} &= \nabla \times \boldsymbol{h} - \boldsymbol{J} - \sigma_D \boldsymbol{D} \\ \boldsymbol{B} &= \mu \boldsymbol{H} \\ \boldsymbol{D} &= \epsilon \boldsymbol{E} \end{aligned} \tag{3.1}$$

Here **D** is the displacement field, ϵ is the dielectric constant, **J** is the current density, J_B is the magnetic charge current density, **B** the magnetic flux density, μ the magnetic permeability, and **H** is the magnetic field. The σ_B and σ_D terms correspond to the frequency-independent magnetic and electric conductivities, respectively. Implicitly, the divergence equations are:

$$\begin{aligned} \nabla \cdot \boldsymbol{B} &= -\int^t \nabla \cdot (\boldsymbol{J}_B(t') + \sigma_B \boldsymbol{B}) dt' \\ \nabla \cdot \boldsymbol{D} &= -\int^t \nabla \cdot (\boldsymbol{J}(t') + \sigma_D \boldsymbol{D}) dt' \equiv \rho \end{aligned} \tag{3.2}$$

3.5.2 Units in Meep

In MEEP units like ϵ_0, μ_0 and c are all unity. This does not affect the result, as most anything that one would want to compute is expressed as a ratio, so that the units cancel. Also, since Maxwell's equations are scale invariant, it's convenient to choose scale-invariant units when solving electromagnetic problems. This means

that one can choose a characteristic lengthscale of the system, e.g. a, and use that as the unit of distance. The frequency ω in MEEP is specified as $\frac{a}{\lambda_0}$, where λ_0 is the vacuum wavelength. If for example a photonic crystal is being described, microns are a convenient unit. Thus a=1μm. If we want to specify a source corresponding to $\lambda_0 = 0.8\mu m$, the frequency is specified as ω=1μm/0.8μm=1.25.

3.5.3 Boundary conditions

A computer can only simulate a finite region of space, so the simulation must be terminated with a boundary condition. Two of the basic types of boundary conditions available in MEEP, are **Bloch-periodic boundaries** and **perfectly matched layers (PML)**.

When setting **Bloch periodicity** in a cell of size L, the field components satisfy $f(x + L)$=$e^{ik_xL}f(x)$ for a given Bloch wavevector k_x. This is what will be used when solving the reflection and transmittance spectrum of a PC. When an **open boundary** condition is desired, i.e. boundaries that absorb all incident waves without reflecting them, PML layers are used. PML is a special (and entirely fictious) absorbing material that is placed adjacent to the boundaries. This material is designed to have zero reflections at its interface in a theoretical continous system, but in the discretized system used by MEEP, some small numerical reflections will be present from the discontinuity. For that reason, a PML is given some finite thickness in which the absorbtion is gradually "turned on", i.e. there is no longer a discontinuity.

3.5.4 Finite-difference time-domain methods

As mentioned above, FDTD methods divide space into a finite discrete grid, which result in a couple of effects that are worth discussing. The first thing concerns memory usage and time consumption. If the grid has a spatial resolution, defined by the user, δx, then the discrete time-step is given by δt=$S\delta x$, where S is the Courant factor and must satisfy

$$S < n_{min}/\sqrt{\#dimensions}, \tag{3.3}$$

in order for the method to be stable. This means that if the resolution is doubled, so does the number of time steps. If one is working with a 3D-structure, the memory consumption will increase by 8, and the simulation time by (at least) 16.

The second thing one should know about, is that in order to discretize the equations with second-order accuracy, FDTD methods store different field components at different grid locations. Such a discretization is known as a **Yee lattice**

[44]. Therefore MEEP must interpolate the field components to a common point whenever you want to combine, compare, or output the field components. This is usually nothing one has to worry about, as MEEP does this automatically. However, since this is a simple linear interpolation, while **E** and **D** may be discontinous across dielectric boundaries, it means that the interpolated **E** and **D** fields may be less accurate than one might expect across dielectric interfaces.

Even though FDTD uses discretized space and time, the user can work in continous coordinates while using MEEP. One only needs to specify the spatial resolution at the beginning of the simulation. The structure that one wants to simulate, can be specified as a set of objects like spheres, sylinders, blocks etc., and MEEP will figure out how they are to be represented on a discrete grid.

3.5.5 Transmission and reflection

When computing the transmission and reflectance spectra from some finite structure in MEEP, the response of the structure to a short pulse is measured. By Fourier transforming this response, a broad-spectrum response can be obtained from a single computation.

The transmittance of a structure, for fields at a given frequency, is the integral of the Poynting vector over a plane on the far side of the structure:

$$P(\omega) = Re\hat{n} \cdot \int \boldsymbol{E_\omega}(\boldsymbol{x})^* \times \boldsymbol{H_\omega}(\boldsymbol{x}) d^2\boldsymbol{x}. \tag{3.4}$$

To do this one first accumulates the Fourier transforms $E_\omega(\mathbf{x})$ and $H_\omega(\mathbf{x})$ for every point in the flux plane via a summation over the discrete time steps n:

$$\tilde{f}(\omega) = \frac{1}{\sqrt{2\pi}} \sum_n e^{i\omega n\Delta t} f(n\Delta t)\Delta t \approx \frac{1}{\sqrt{2\pi}} \int e^{i\omega t} f(t) dt. \tag{3.5}$$

After the time stepping is done, $P(\omega)$ can be computed from the fluxes of the Fourier transformed fields. This is all done by MEEP; the user only need to specify the region and frequencies over which the fluxes should be calculated. For the aquired data to be meaningful, the power must be normalized. This can be done by running the simulation twice, where the first run is done without the structure. The data aquired this way can be used to normalize the transmitted power.

The reflection spectrum on the other hand is a bit more tricky. In this case one can not simply measure the flux in the backwards direction, as this would give the sum of the incident and reflected incident power, nor can one simply subtract the incident power, as this won't tak into account interference effects. To get the correct reflected power, one must subtract the Fourier-transformed incident fields $E_\omega^{(0)}(x)$ **and** $H_\omega^{(0)}(x)$ to get the reflected power:

$$P_r(\omega) = \boldsymbol{Re\tilde{n}} \cdot \int \left[\boldsymbol{E_\omega(x)} - \boldsymbol{E^0_\omega(x)}\right]^* \times \left[\boldsymbol{H_\omega(x)} - \boldsymbol{H^0_\omega(x)}\right] d^2\boldsymbol{x} \tag{3.6}$$

This can also be achieved by running the simulation twice. Once without the structure and once with. On the second run, the Fourier transforms in the reflected plane from the first run can be subtracted before the flux is computed. To get the reflection spectrum, one only has to normalize to the incident power.

3.5.6 The simulation

When doing a simulation, one uses a control file which contains all the information MEEP needs. This file contains information about the computational cell, like the structure that will be simulated, resolution (of the grid) and boundary conditions. It also contains information about sources, where in the cell transmisson and reflection shall be measured and when the simulation shall end.

The resolution is by default 10, meaning that each unit length of the cell is divided into 10. This will in most cases be insufficient, as the structures won't be accurate enough, as demonstrated in figure 3.7(a) and figure 3.7(b), where the resolution were 10 and 40 respectively. The figures shows crossections of a triangular structure of spheres, and as can clearly be seen from figure 3.7(a), a resolution of 10 is far from enough to accurately define a circular shape (spherical in 3 dimensions of course). However, doubling the resolution has the drawback of increasing the memory consumption by 8 and the time by 16 (approximately), meaning that a compromise usually must be made due to time constraints or available memory (e.g. the longest simulations run in this project used a resolution of 50 and took about 135 hours for the largest structures.). In the end, a resolution of 40 was chosen, as this yielded satisfactory results and reduced the simulation time substantially (approximately 24h).

The transmission and reflection is measured through planes specified by the user. Specifying how long the simulation is to run, can either be done by setting a simulation time, or by setting a condition that must be fulfilled before the simulation comes to an end. The latter is used for photonic crystals, as these structures trap light for a relatively long time. In this case one can simply say that, e.g. E_x^2, at a given position within the cell has to decay to certain level before the simulation is ended. By setting this parameter lower, the the accuracy of the simulation will be increased, but so will the simulation time.

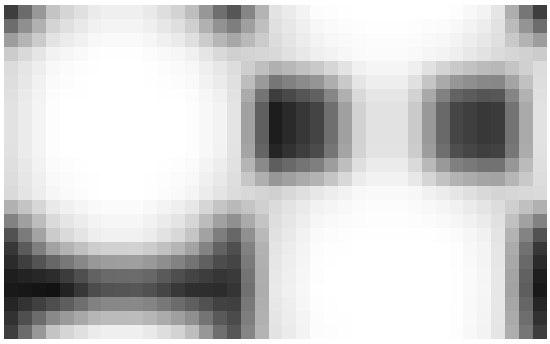

(a) Resolution: 10

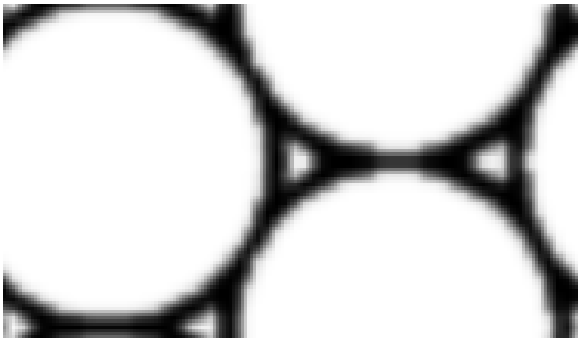

(b) Resolution: 40

Figure 3.7: Crossectional images of a structure with two different resolutions, in this case 10 and 40. Although neither resolution is high enough to define a perfect spherical shape, a resolution of 40 is sufficient to get the needed accuracy, while 10 is not.

Chapter 4

Reflection simulations

In this section the simulated reflection properties of the fcc and hcp inverted opal structures will be presented. These simulations were done for three reasons. Firstly, the simulations were done to investigate the width and placement of the reflection peaks relative in wavelength for a inverted opal of finite thickness on a substrate. Secondly, they were done to obtain a reference for determining whether the grown structures were fcc or hcp, simply by comparing simulated and measured reflectance. Secondly, although not less important, the simulations were done to visualize the scalability of Maxwell's equations, and how this can be used to tailor the properties of the inverted opal just by adjusting the sphere size. The source code for the simulations can be found in appendix A.

4.1 Reflection from fcc and hcp inverted opals

The fcc and hcp structures were built up of air spheres covered with a thin layer of silicon on a silicon wafer, with the topmost layer of spheres terminated in the middle, leaving a surface layer of half-spherical shells (essentially looking like a triangular structure of bowls). In a cartesian coordinate system, the z-axis was chosen perpendicular to the substrate and the x- and y-axis parallel to the substrate. Simulations were done for structures with 1, 3 and 6 layers of spheres grown in the z-direction. The structures were oriented with the [111] crystallographic direction perpendicular to the substrate (i.e. [111] plane is parallel to the substrate), that effectively extended to infinity in the directions parallel to the substrate. Reflection simulations were done for light incoming from both silicon and air, and were with a resolution of 40 for frequencies from 0.35 to 0.95 (in units of $\frac{2\pi c}{a}$), corresponding to wavelengths (in vacuum) from 730 nm to 1980 nm. Reflection spectra were calculated at normal incidence for 700 different frequencies in this interval, and the simulations were allowed to run until E_z^2 in the reflection plane

was reduced to $1e^{-6}$ of its peak value. Two Gaussian sources were used to get a strong enough signal over the entire frequency range, as too low a signal yielded a poorer accuracy in the simulations. The two sources were in phase, but with center frequencies 0.2 apart. These and more parameters are listed in table 4.2. Absorption in silicon was not taken into account.

Table 4.1: Simulation parameters

Resolution	40
Infill ϵ	13
Sphere ϵ	1
# of sources	2
Source type	Gaussian
Center frequencies	0.65±0.1
Frequency range	0.35-0.95
# of frequencies	700
λ_0	730-1980nm
Decay to value	$1e^{-6}$

Table 4.2: Parameters used in the simulations.

As mentioned above, the structures that were simulated were the hcp and fcc structures, which only differ in the stacking order of the sphere layers, as explained in chapter 2.4. The *fcc* structure has an ABCABC... stacking order, while the *hcp* structure has an ABABAB... stacking order. This is further visualized in figures 4.1(a)-4.1(h), which shows cross-sectional images of the computational cell, parallel to substrate (perpendicular to the [111]-direction) of the four first layers in the two structures. The green and red line in figure 4.1(c) indicates where the cross-sectional images perpendicular to the substrate, which will be shown below, were taken in the cell. The green line indicates the y=0 cross-section, and the red line indicates the x=0 cross-section.

Below, the reflection spectrum will be presented for the 1-layered structure (triangular) and 3- and 6-layered fcc and hcp structures with a silicon wafer as a substrate. Cross-sectional figures of the structures will also be shown (perpendicular to the substrate). In the X- and Y-crossections, some spheres appear to be smaller, but this is simply because the crossections doesn't go through their middle, i.e. their centers are displaced in the y or x direction relative to the large spheres. The black border around these images was added afterwards as a visual aid.

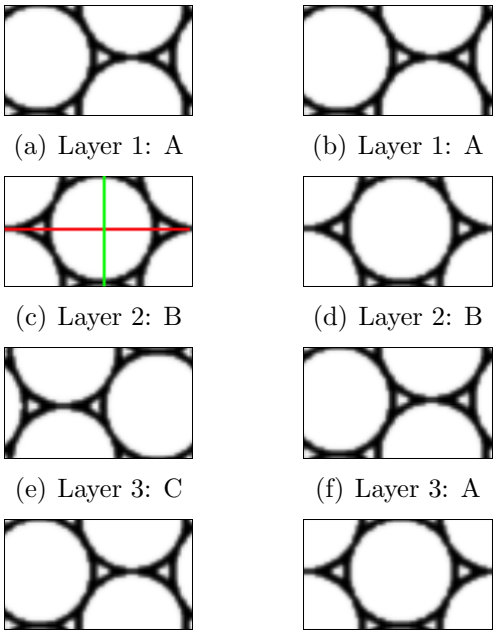

(a) Layer 1: A (b) Layer 1: A

(c) Layer 2: B (d) Layer 2: B

(e) Layer 3: C (f) Layer 3: A

(g) Layer 4: A (h) Layer 4: B

Figure 4.1: Cross sectional images parallel to the substrate of the four first layers of the fcc (left) and hcp (right) structures. Notice the ABCA stacking of the fcc structure (left column) and the ABAB stacking of the hcp structure (right column).

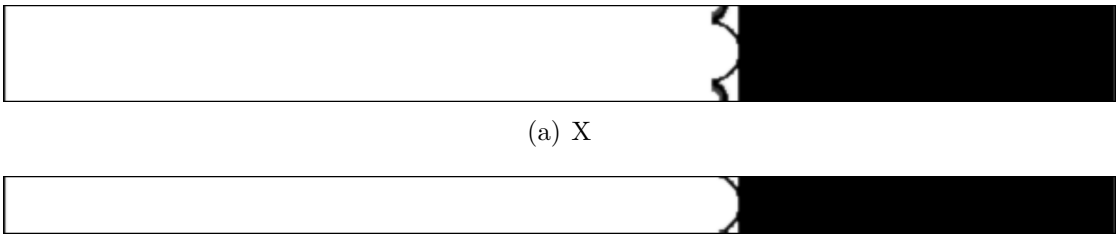

(a) X

(b) Y

Figure 4.2: X and Y cross-sections of one cell of a triangular lattice of air spheres infilled with silicon on a silicon substrate (black).

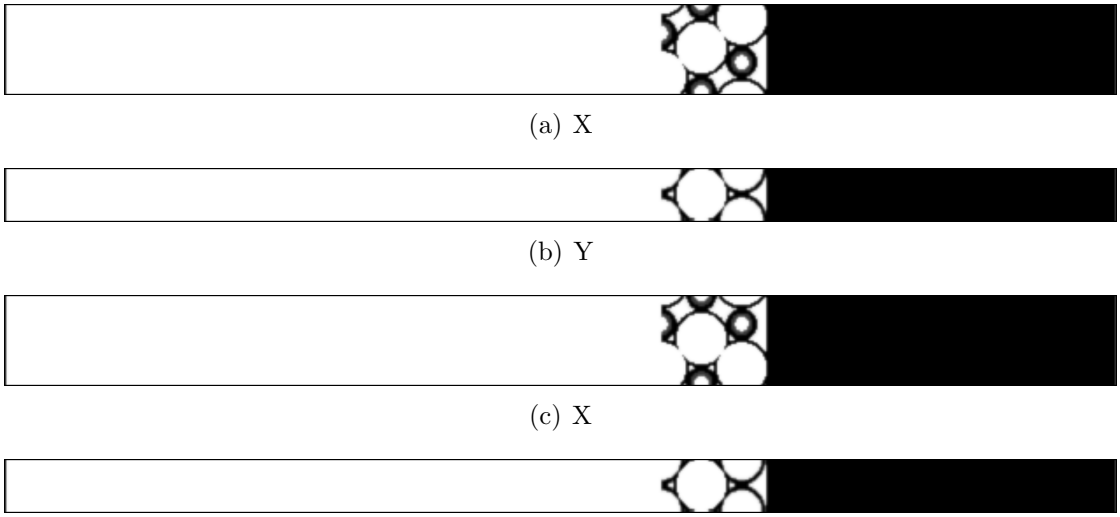

(a) X

(b) Y

(c) X

(d) Y

Figure 4.3: X and Y cross-sections (parallel to the growth direction) of a 3-layered fcc structure (a and b) and a 3 layered hcp structure (c and d) on a silicon substrate (black).

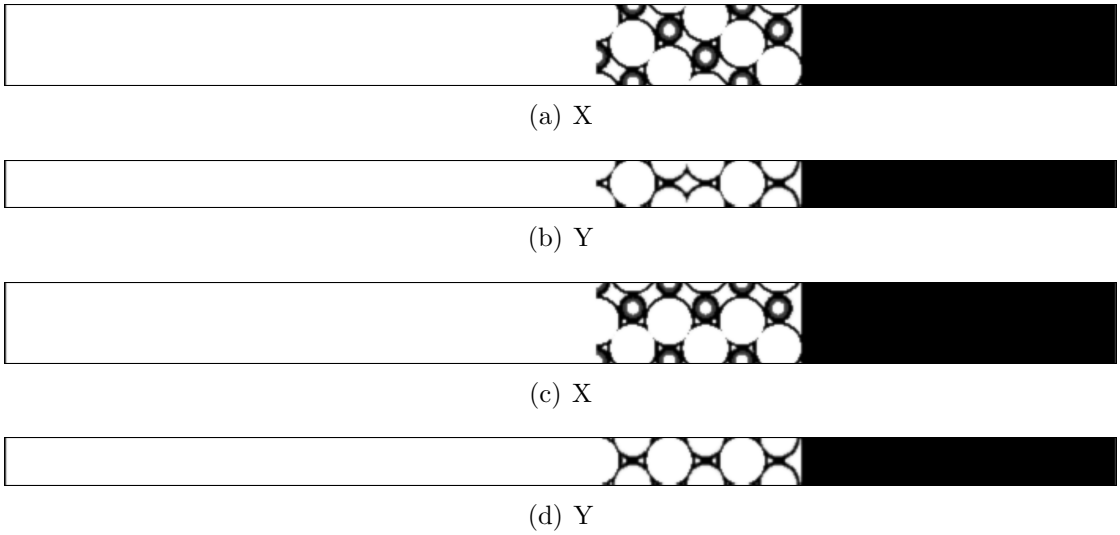

(a) X

(b) Y

(c) X

(d) Y

Figure 4.4: X and Y cross-sections (parallel to the growth direction) of a 6-layered fcc structure (a and b) and a 6-layered hcp structure (c and d) on a silicon substrate (black).

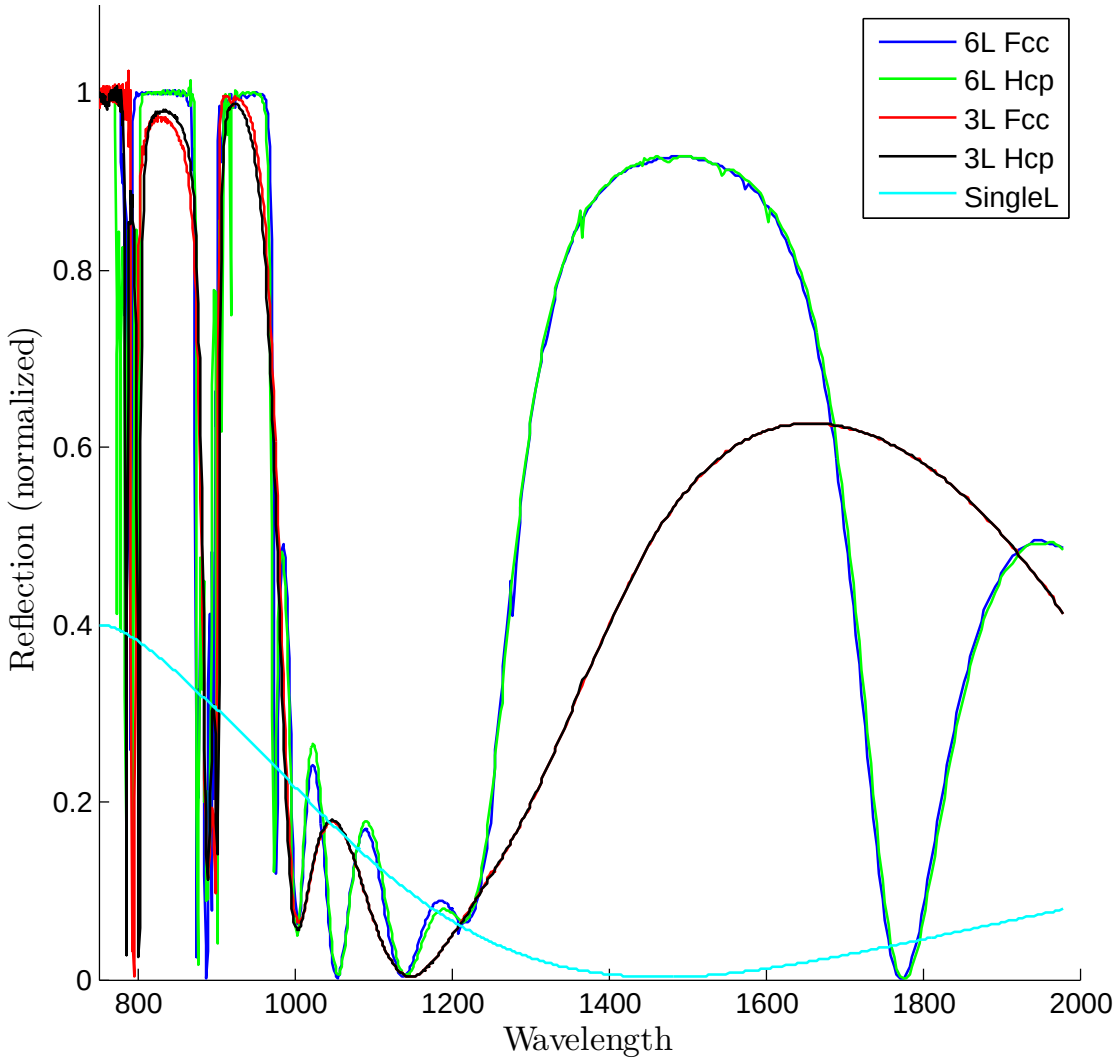

Figure 4.5: Reflection from opal structures on a silicon substrate, with light incoming from air.

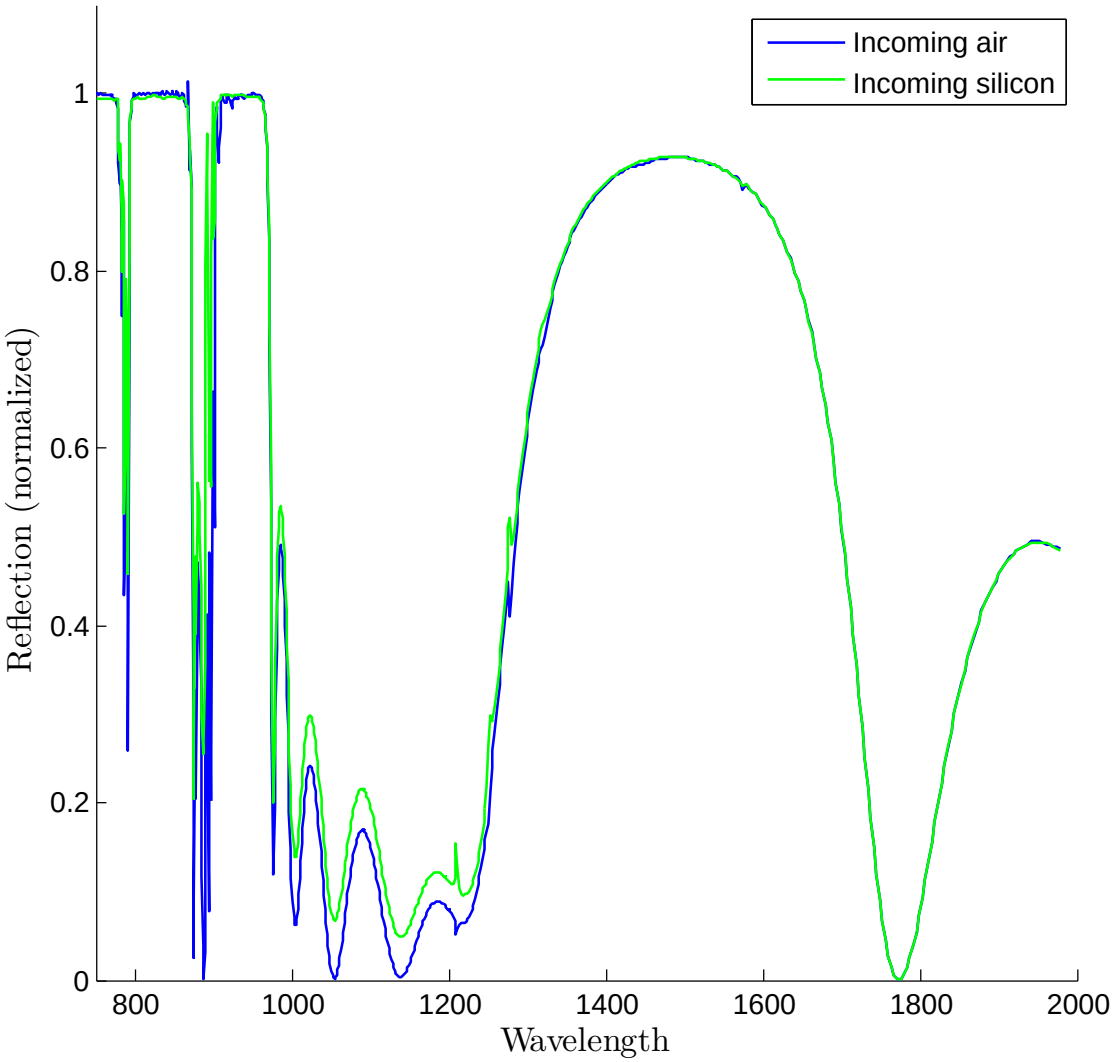

Figure 4.6: Comparison of reflection spectra of ligth incident on a 6 layered opal structure from air and silicon.

Before discussing the simulated reflection spectra in figure 4.5, the reader should be made aware that there seems to be a shift upwards in frequency for the band structure of the structure used in these simulations compared to the calculated band structure in figure 4.7 (calculations by Joannopoulos et al. [7]). This shift is not very noticable for the lower lying bands, but for the calculated complete PBG, i.e. between abnds 8 and 9, the shift is of about 0.05 in frequency, corresponding to 100nm in wavelength. Detailed information about the band structure calculations done by Joannopoulos is not available, but one can assume that an effectively infinite structure was used (setting Bloch boundary conditions

on the calculation cell). This differs from the structure simulated here, which was of finite thickness with an interface towards air one side and to silicon on the other. The relative sphere radius and dielectric contrast were the same. Valsov et. al [8] did band gap simulations of a structure similar to the one used in this master project, and shows the same frequency shift, leading to the assumption that the shift is related to finite nature of the structure.

These oscillations are caused by light that is still trapped in the structure, an effect most strongly observed for light within the complete BG. Interference between this light and light that has escaped, will cause the oscillating nature, and can be avoided by running the simulations longer. These effects appears more strongly in the loss spectrum, as the effects on both transmission and reflection are added here. Loss was calculated as 1-reflection-transmission (power reflectance and transmission). A simulation was done to quantify this effect, and the result can be seen in figure 4.8, where the loss is plotted for two simulations. One that has a decay-to value of $e^{-}6$ and the other with $e^{-}7$, and as can be seen, the loss is nearly eliminated, exept for some spikes around 900nm. Unfortunately, this also increased the simulation time manyfold; from 24 hours to a week for a single simulation. The general result of the simulations were however still valid, so a satisfactory compromise between simulation time and accuracy was reached.

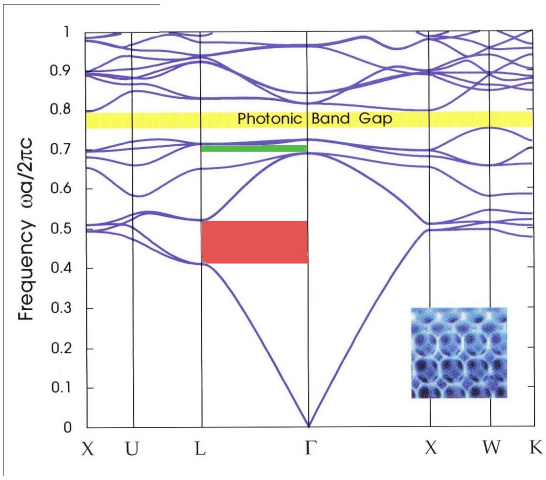

Figure 4.7: Band diagram of the inverted opal. Reprinted for conveniance.

The simulated reflection spectrum in figure 4.5 shows several reflection peaks. Starting at long wavelengths, the broad reflection peak centered around 1480 nm appears due to the first incomplete bandgap, marked with a red band in figure 4.7. This reflection top has a reflection of 93% for both the 6-layered fcc and hcp structure, and as can be seen, there is little difference between the two. The full width half maximum (FWHM) of the peak is 430 nm.

The reflection peaks between 950nm and 1200nm are due to constructive interference between waves reflected from the wafer and the top of the structure. As can be seen, the thicker structures have several peaks as their increased thickness increase the amount of wavelengths fulfilling Braggs criteria [16] for constructive interference:

$$\lambda = 2dcos\theta. \tag{4.1}$$

λ is the wavelength of the light, d the thickness of the structure and θ the angle of incidence (90°for normal incidence). For normal incidence on one layer of spheres (d=490nm), the longest wavelength fulfilling this criteria would be 980nm (i.e. two times the sphere diameter). This does of course assume that light travels strictly through air and that no refraction occur. Both of these assumptions are of course incorrect. Firstly, the surface of the structure is not planar, so some light would be "bent" on entering it, resulting in a shift upwards in wavelength. Secondly, the light does not travel only through air on its way through the structure, but will also move through the dielectric framework. As the wavelength of light becomes shorter with increasing refractive index n ($\lambda = \frac{\lambda_0}{n}$), this will cause a shift upwards in wavelength as the effective wavelength of the light in the structure becomes shorter.

In addition to result in a shift upwards in frequency, both of the above effects will cause a broadening of the reflection tops. The reason for this is that not all the light incident on the structure will bent equally, nor will all the light move equally much through the dielectric framework. In figure 4.5 the net result of these effects can be seen, where the reflection peak for the single layer is centered around 1010 nm, and stretches out for almost 200 nm.

Next, there are two reflection peaks with near unity reflectance, centered around 835 nm and 940 nm. The peak around 940 nm is due to the incomplete BG marked with a green band in figure 4.7, while the peak around 835 nm is due to the complete BG marked with a yellow band.

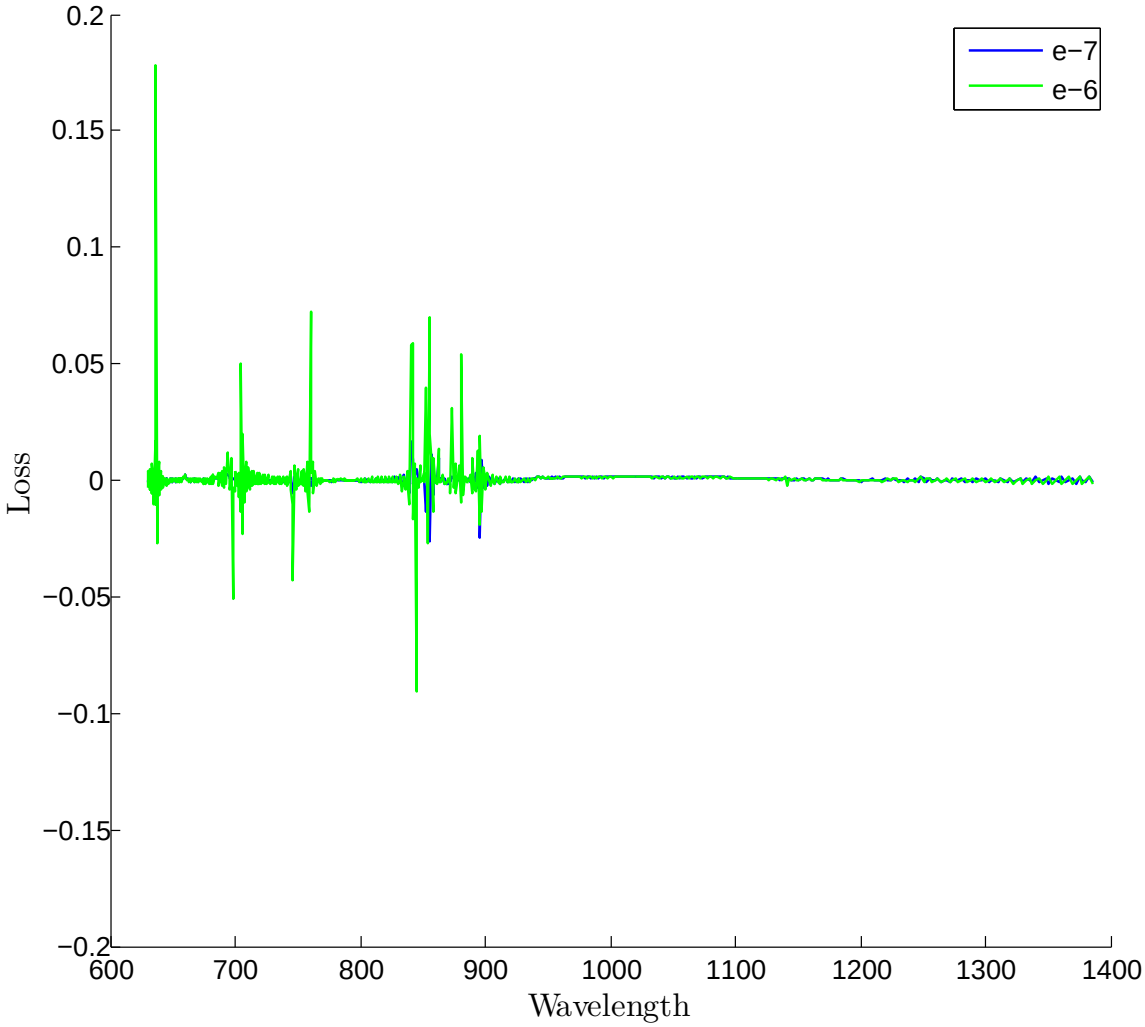

Figure 4.8: The loss in simulations of a 6 layered fcc structure on silicon, with the decay-to value set to e^{-6} (green) and e^{-7} (blue). The loss when the decay-to value has been decreased, is far smaller than before, with only a few spikes around 900nm.

4.2 Scaling properties

In chapter 2.1.1, the scalability of Maxwell's equations was shown mathematically with the master equation. Here this will be demonstrated graphically with the simulated reflectance spectra. The fact that Maxwell's equations are scalable, means that the optical properties of a structure can be shifted in wavelength, simply by adjusting it's scale, i.e. sphere size in an inverted opal. This is shown in figure 4.9, where the reflection peak of the first incomplete BG (red band in figure 4.7) is shifted up and down in wavelength by adjusting the sphere size. Also note that the width of the reflection peaks are reduced when they are shifted down in wavelength, an effect of the inverse dependence of wavelength on frequency.

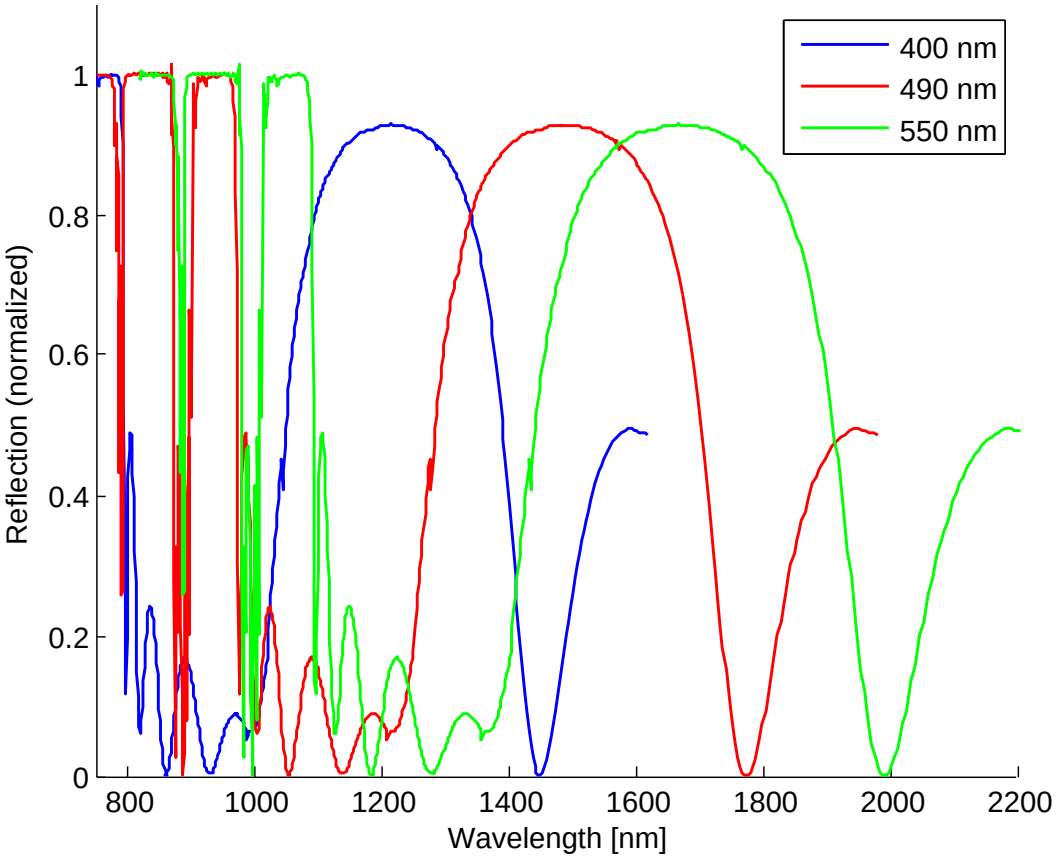

Figure 4.9: Reflection spectra for spheres with a diameter of 400 nm, 490 nm and 550 nm. As can be seen, the spectra is just shifted in wavelength, although with a change in width for the reflection peaks due to the inverse dependence on frequency.

In figure 4.10 a similar shift has been done, but in this case for the reflection peaks corresponding to the complete BG and the incomplete BG just under it in frequency (green band in figure 4.7). This particular wavelength range was chosen as it is the near-visible part of the IR-spectrum, which is of particular interest for this thesis.

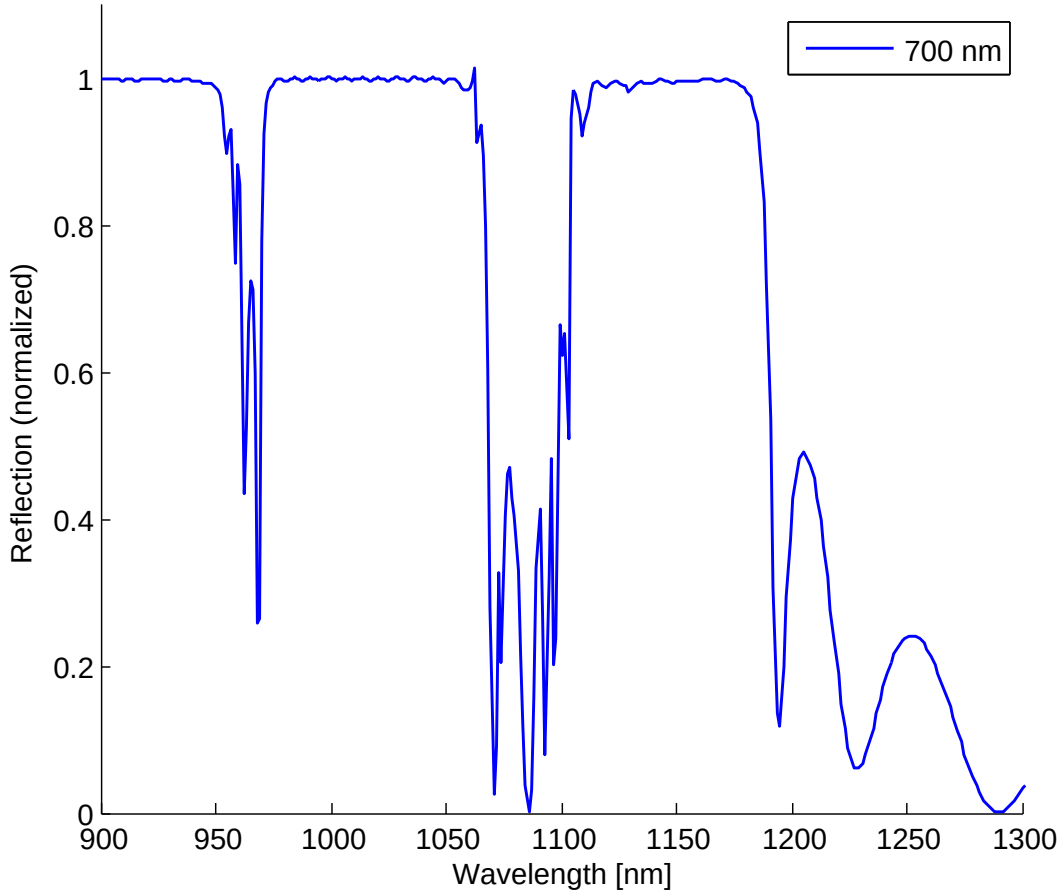

Figure 4.10: The figure shows the reflection tops due to the complete BG (1020 nm) and the incomplete bandgap below it in frequency (1150 nm)

Chapter 5

Results

In this chapter the result of the work done during the master thesis will be presented. First the results with the various opal growth methods will be presented, continued by the results from opal inversion. The results will be presented in form of images taken with an optical microscope and a SEM.

5.1 Opal growth

The opal growth experiments were done using three different methods (see chapter 3.2). The first method was based on the method developed in the preceeding projectwork [34] and the other two were adapted from methods described in publications [26, 28, 29, 31].

The work on the first method was done at an early stage in the master work when only Ugelstad spheres, with a diameter of $3.27\mu m$, were available. The idea was that this method could be adapted for spheres of a more suitable size, i.e. 450-800nm in diameter. Unfortunately this proved unsuccessful, resulting in a discontinuation of the work with this method, as will be explained below. The results and work done will however be presented here. With method #2&3, only PS spheres were used.

5.1.1 Method #1: Diffusion

Method #1 was mainly used with Ugelstad spheres, and the results from these experiments will be presented here. The method proved less suitable for the PS spheres, but the results with these spheres will be briefly presented at the end of this section.

In the masters work, the initial goal was to improve the method used to make the **reference sample** (figure 5.1). This sample was made using the old version

of method #1 used in the master work, as explained in chapter 3.2, and showed a large variation in quality. Large areas had an average grain size in the range of 500-1000μm^2, but the sample average was closer to 300-350μm^2. The reference sample was prepared by diffusing a solution of 23 wt.% spheres, 16 wt.% ethanol and 61 wt.% water onto an ethylene glycol containing water film (30% eth.gl.). The water film was then allowed to evaporate, leaving a polycrystalline monolayer of spheres on the wafer. Figure 5.1 shows an area from the reference wafer of average quality. The black dots that can be seen on this sample, are extra spheres on top of the monolayer. The samples described and shown below will all be compared to this sample.

One thing that was quickly modified in the master work was the deposition method. With the old method, the sphere solution and the water film were placed adjacent to each other on a wafer, but in the new method they were placed on separate wafers. When the wafer with the sphere concentration was brought into contact with the water film, a diffusion of spheres onto the water film started. These spheres diffused rapidly (a few seconds) to the opposite side of the water film, where they immediately started to crystallize. This process continued until the entire water film was covered with spheres, which took about 5 minutes.

It should be mentioned that this method proved unsuccessful for eth.gl. containing water films, so pure water films were used instead. The parameters that were tried optimized, were ethanol and sphere concentration in the sphere solution. Table 5.1 lists the solutions used.

Although the samples made using the different solutions varied in quality, as will be shown, almost all of them produced wafer sized monolayers.

Solution #	Spheres(wt.%)	Ethanol(wt.%)
1.1	23	4
1.2	11.5	4
1.3	8.5	4
1.4	4	4
1.5	2.5	16
1.6	2.5	7
1.7	2.5	2
1.8	2.5	0.8
1.9	11.5	7

Table 5.1: The different solutions used. The remaining content of the solutions was always DI-water.

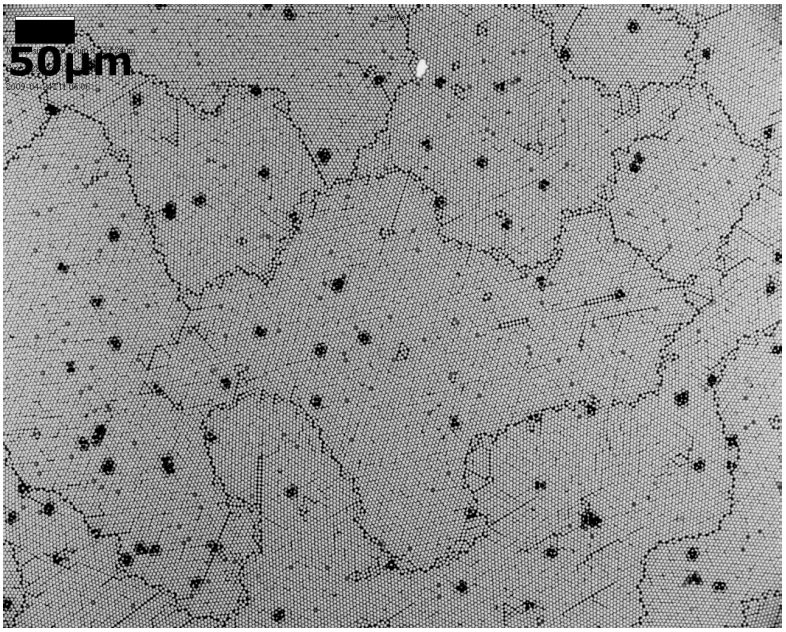

Figure 5.1: Microscope image of an area on the reference sample of average quality. The sample was made using a diffusion process of spheres from a solution reservoir onto a ethylene glycol containing water film. Both the water film and reservoir was on the same wafer, as can be seen in figure 3.1. The solution had a 23 wt.% of spheres and 16 wt.% of ethanol.

All the samples presented below were placed under a plastic cover while the water film evaporated. This had the effect of increasing the evaporation time from approximately 20 hours to 90 hours, as well as protecting the sample from airfluctuations in the laboratory. Sample quality was improved by this, although the effect varied some from sample to sample. An example of how significant this effect could be, is shown in figures 5.2(a) and 5.2(b), where the samples were made without and with a plastic cover respectively.

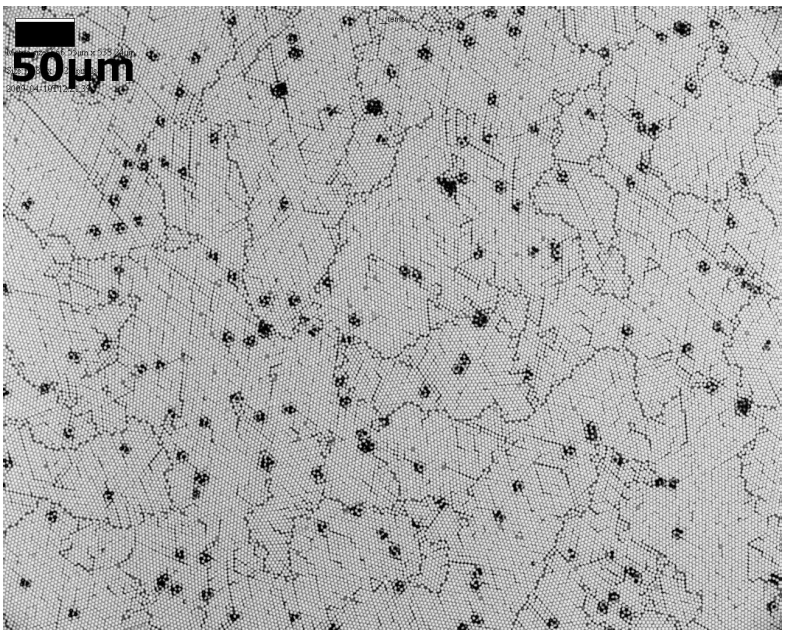

(a) Without a plastic cover

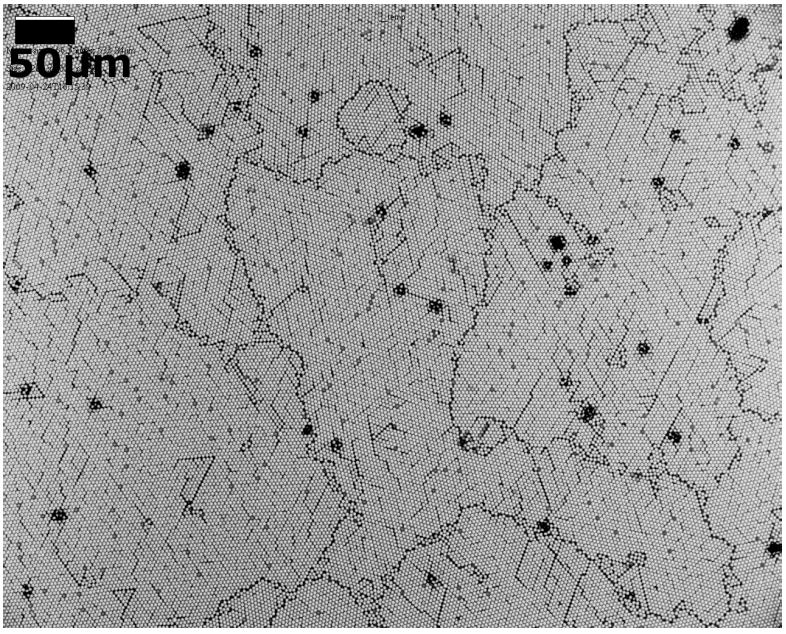

(b) With a plastic cover

Figure 5.2: Sample **a** was prepared without a cover, and sample **b** was prepared with a cover. Notice the greatly improved grain size from sample **a** to sample **b**.

Sphere concentration

To examine the effect of sphere concentration on the quality of the samples, an ethanol concentration of 4 wt.% was chosen. Sphere concentrations that were investigated, were 23, 11.5, 8.5 and 4 wt.% (solution 1-4). Images of these samples are shown in figures 5.3(a)-5.3(d), and as can be seen, there is only a small improvement in grain size from the sample prepared with solution 1.1 to the one prepared with solution 1.4. The grain size of the samples improved from an average of 50-75μm^2 with solution 1 to 75-100μm^2 for the sample prepared with solution 4. For all the samples the defect density was far higher, and the grain size far smaller than for the reference sample.

Ethanol concentration

To see the effect of ethanol concentration on the crystalline quality of the monolayer, samples were made using solutions 1.5-1.8. These solutions had 2.5 wt.% spheres, and 16, 7, 2 and 1 wt.% ethanol respectively.

Using solution 1.5 and 1.6, samples with a maximum grain size of some hundred μm^2 and an average grain size of 50-100μm^2 was obtained (figures 5.4(a) and 5.4(b), 16 and 7 wt.% ethanol respectively).

The sample made using solution 1.7 (figure 5.4(c), 2 wt.% ethanol) yielded a far better result than the two samples above. The quality of this sample regarding grain size, was notably better than for the previous samples with an average grain size of 250-300μm^2. Grains with a size of mm^2 could also easily be found. Compared to the reference sample the amount of both line and point defects was still quite high, and the grain size was slightly lower, although more uniform across the sample. The number of extra spheres were however lower.

With solution 1.8, the method proved unsuccessful. There was some diffusion of spheres onto the water film, but a mixing of the sphere solution and the water film dominated. Mixing may be to stretch it a bit, as what was observed was that the spheres slowly diffused close to the wafer surface, i.e. at the bottom of the water film.

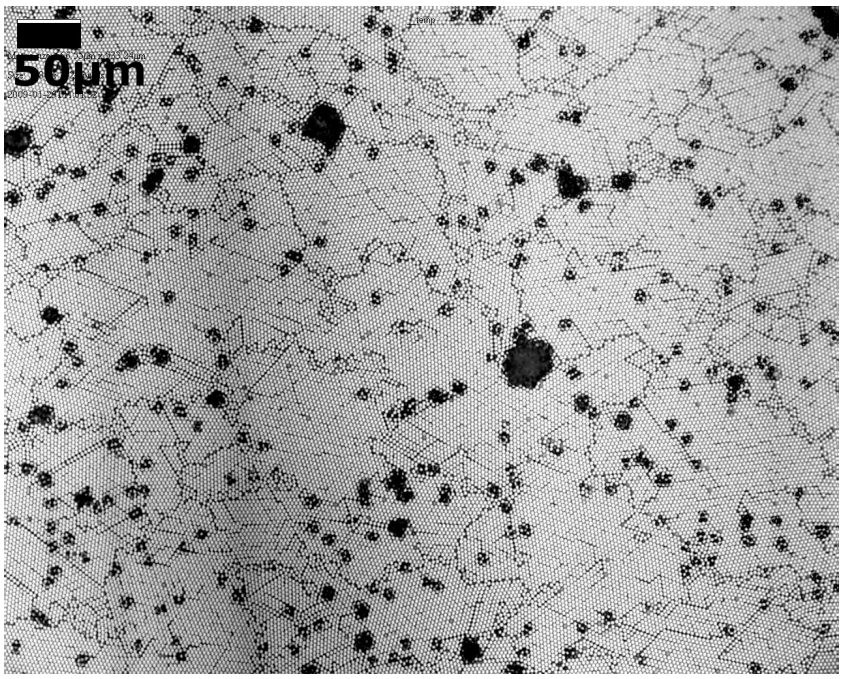

(a) Solution 1.1

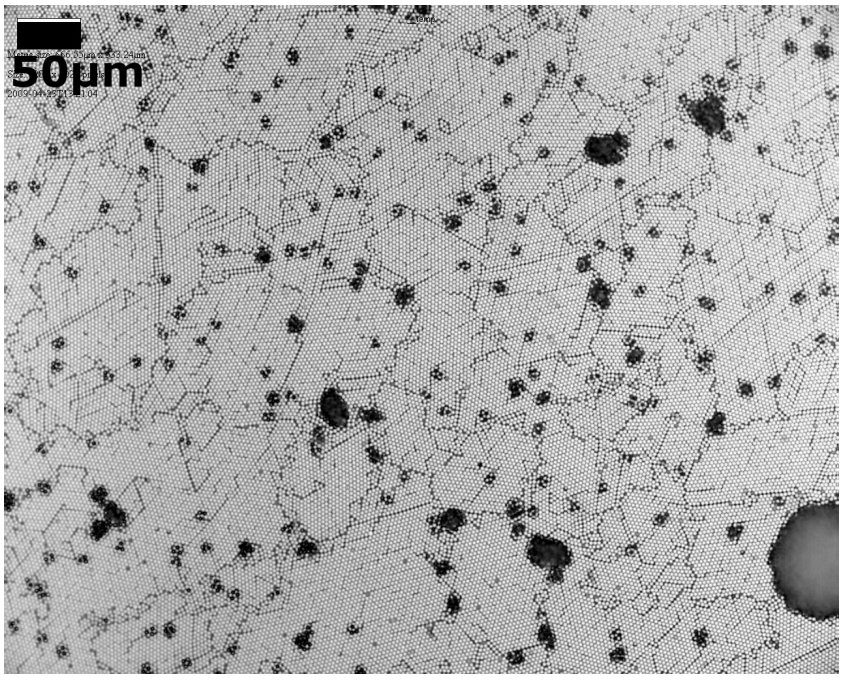

(b) Solution 1.2

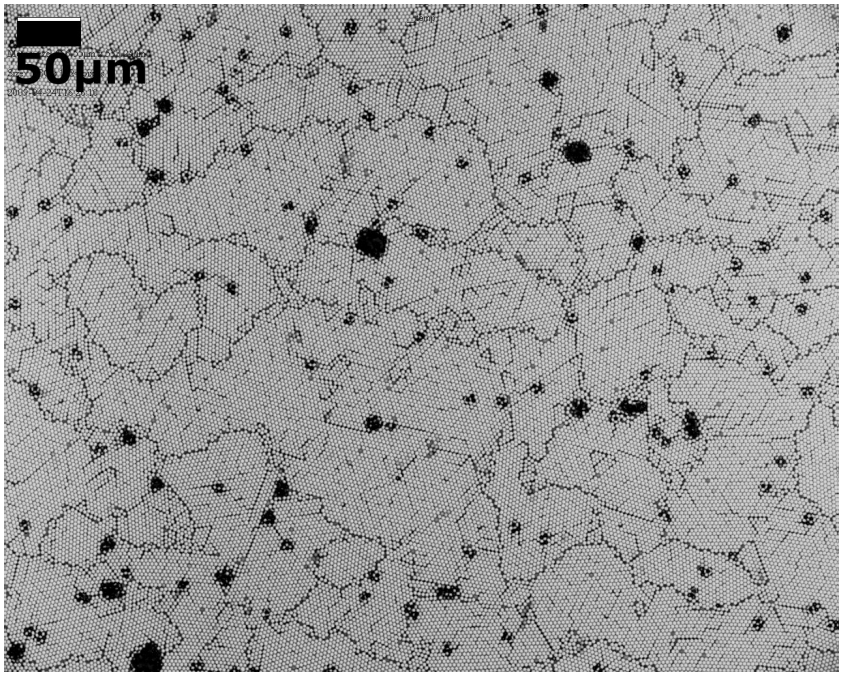

(c) Solution 1.3

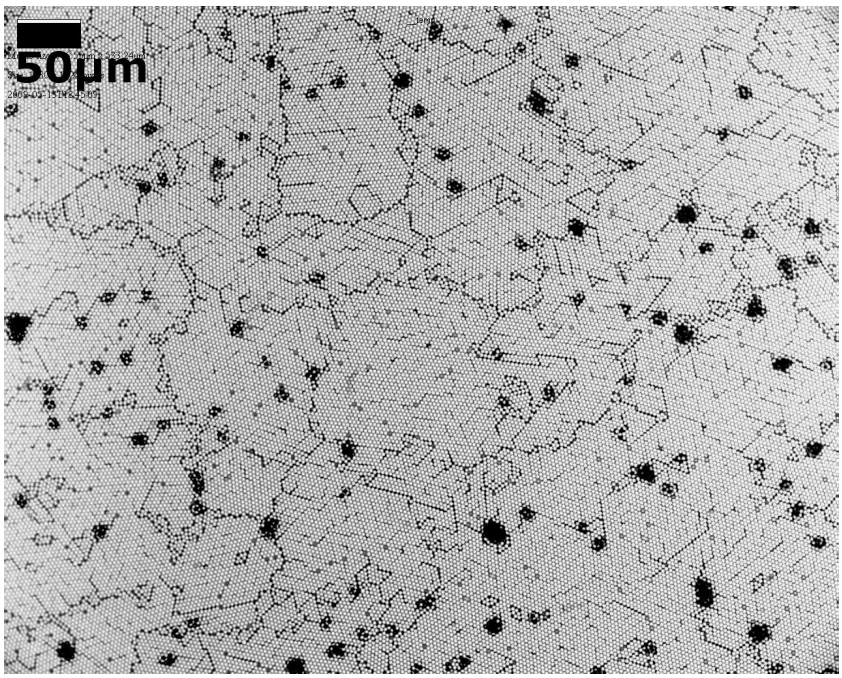

(d) Solution 1.4

Figure 5.3: The four samples shown were made with solutions containing 23, 11.5, 8.5 and 4 wt.% spheres. As can be seen, the average grain size doesn't change much, but the amount of extra sphere on top of the layer is somewhat decreased.

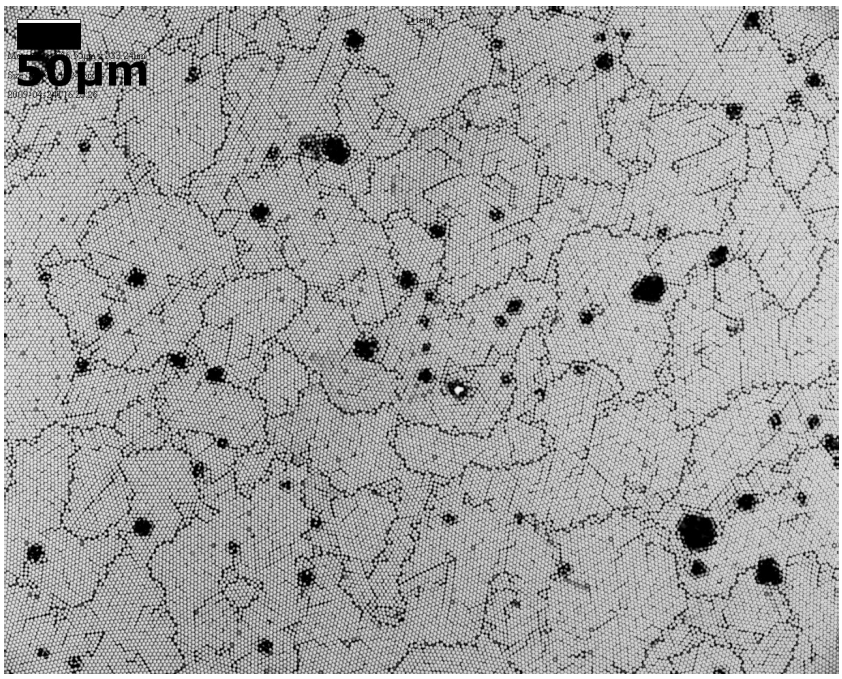

(a) Solution 1.5

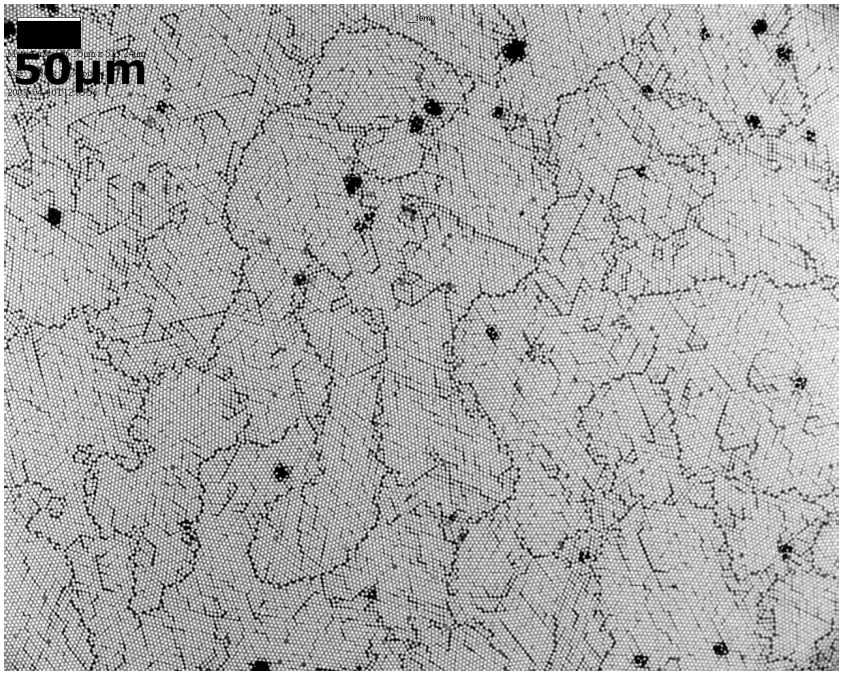

(b) Solution 1.6

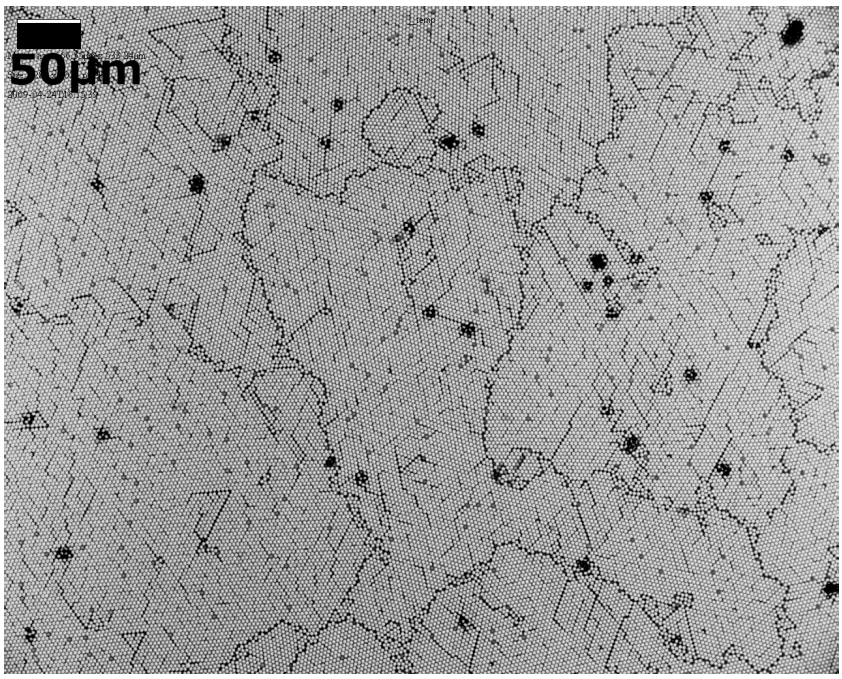

(c) Solution 1.7

Figure 5.4: The images show the samples prepared using solution 1.5-1.7. As can be seen, there is a clear improvement in crystal size from high to low ethanol concentrations. Also, compared to the samples that were made with solutions 1.1-1.4, the amount of extra spheres on top of the layer are greatly reduced.

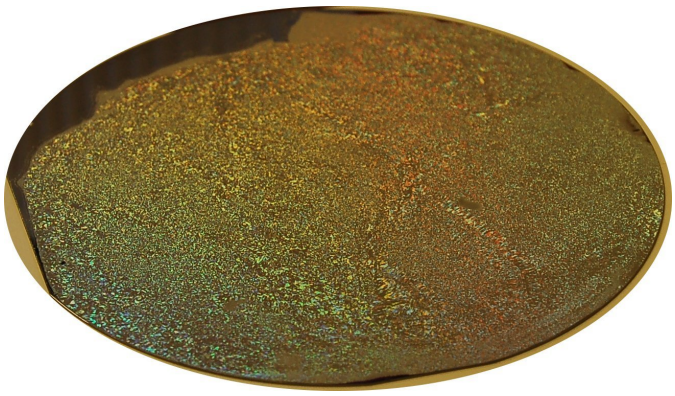

Figure 5.5: Photo of the sample made with solution 1.7, showing the monolayer grown using Ugelstad spheres. The wafer is 10cm in diameter.

Sphere and ethanol interdependence

The results above would indicate that a lower concentration of ethanol and spheres should yield better results. Some experiments were also done to investigate the possibility that ideal ethanol and sphere concentrations were dependent on each other. To do this, a sample was made using solution 1.9, which had the same ethanol concentration as solution 1.6 (figure 5.4(b),11.5 wt.% spheres) and the same sphere concentration as solution 1.2 (figure 5.3(b), 7 wt.% ethanol). A microscope image of the sample made with solution 1.9 can be seen in figure 5.6. If one compares this sample with the ones made with solution 1.6 (figure 5.4(b)), it becomes clear that even though the sphere concentration is increased, the grain size improves. On the other hand, if one compares the sample with the one made using solution 1.2, the quality of the sample also increases with an increase in the ethanol concentration.

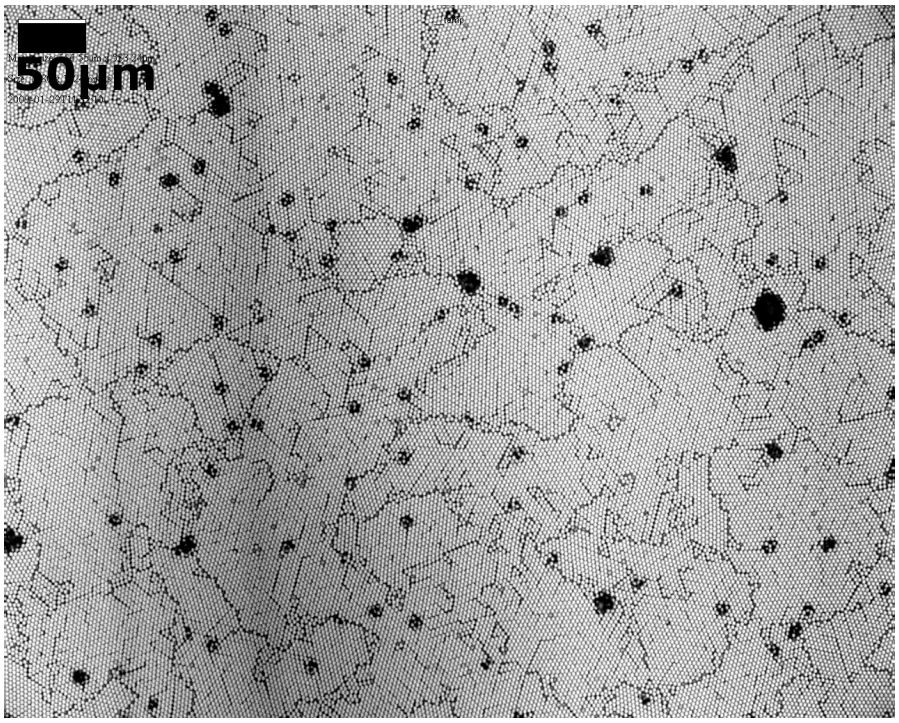

Figure 5.6: A sample made using solution 9: 11.5 wt.% spheres and 7 wt.% ethanol. Comparing this sample with the ones made using solution 1.2 and 1.6 (figures 5.3(b) and 5.4(b) respectively), an improvement can be seen for a relative increase in both ethanol and sphere concentration.

Polysterene spheres

The Ugelstad spheres used in the experiments above had a diameter of $3.27\mu m$, which is far from ideal to obtain strong diffractive reflections in the near visible parts of the IR-spectrum (i.e. for wavelengths between 800nm and 1200nm). For this reason, PS spheres with a diameter of 490 nm was purchased from Bang Laboratories inc.

These spheres can, if they are packed in a crystalline structure, exhibit diffractive properties that are visible to the naked eye. It's also expected that the normal reflective properties will be enhanced, but these reflections may see the greatest enhancement for longer wavelengths.

With the PS spheres, the diffusion of spheres from the reservoir to the water film was done without the use of ethanol (although it was successfully done with ethanol too). The spheres seemed to distribute themselves evenly on the water film, but during evaporation the spheres accumulated at the leading edge of the water film. This resulted in a multilayer structure of spheres that became thinner in the direction of the water films leading edge during evaporation, as indicated in figure 5.7 with black arrows. As can be seen from the photo, which was taken after all the water had evaporated, a large area was left without spheres. Light microscope images of a sample made this way, can be seen in figure 5.8. The average grain size in these samples were about 10-20μm^2.

Due to the problem with covering the entire wafer, and the small grain size achieved, further work with this method was stopped. This choice was also motivated by the knowledge of other methods that could yield far better result, as will be presented below.

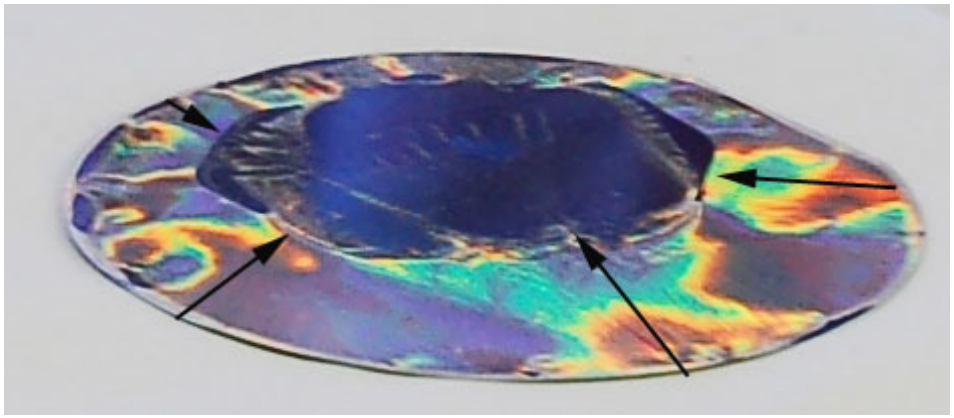

Figure 5.7: Image of the sample using PS spheres with method #1. The direction of the leading edge of the water film during evaporation is indicated with black arrows. Note the large area without spheres.

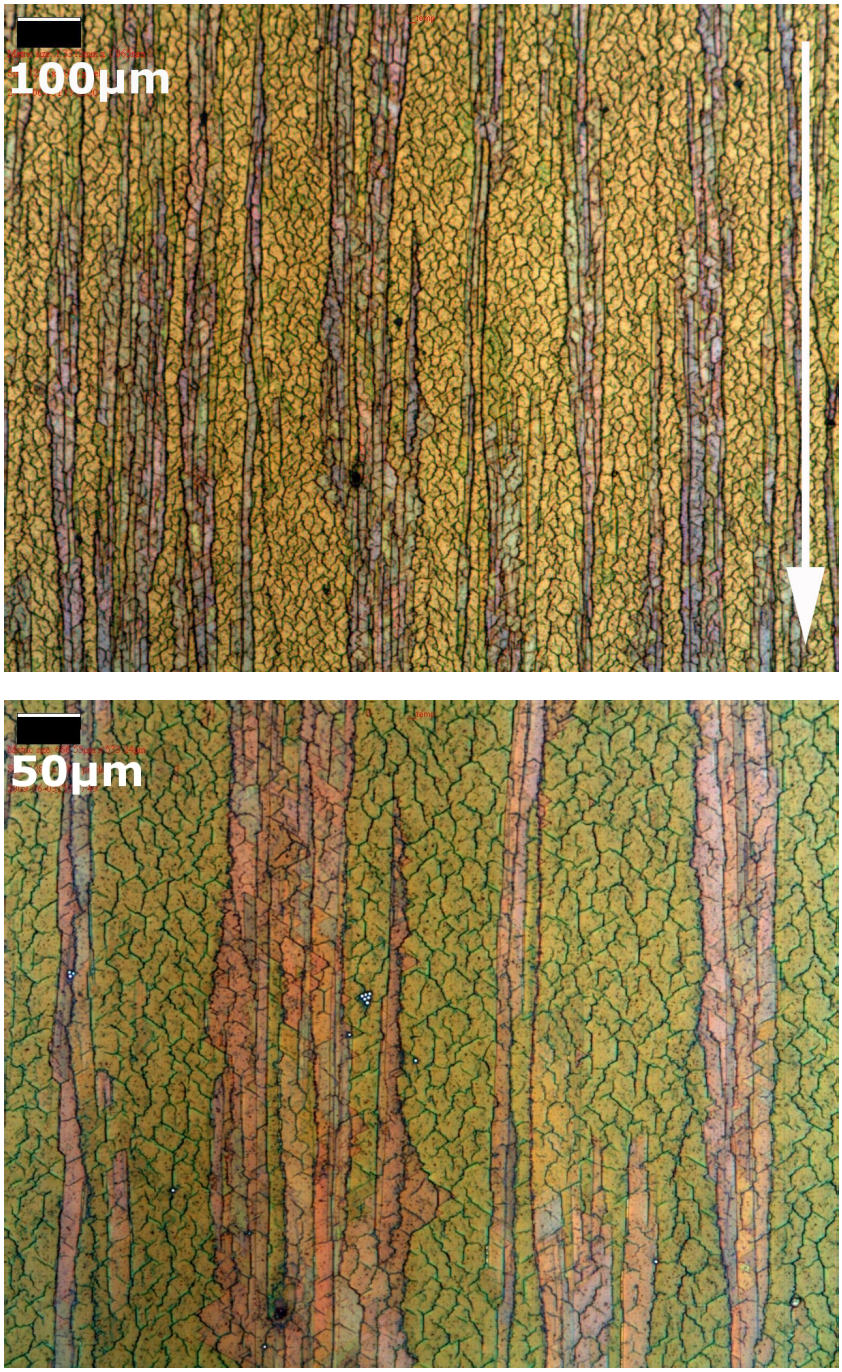

Figure 5.8: Microscope images of an opal made with method #1 using PS spheres. The direction of growth in the images is down, as shown with the large white arrow. The resolution is 10x (top) and 20x (bottom).

5.1.2 Method #2: Draining

With this method, a sphere solution was placed in a reaction vessel, with a substrate vertically submerged in it. The solution was then slowly drained from the bottom of the reaction vessel, thereby causing the meniscus that forms at the substrate-air-solution contact line to move down along the substrate. This speed was determined to be 450nm/s at the beginning of the experiment and 200nm/s at the end, the reason for which will be discussed in the Discussion. The sample made in this experiment is listed in table 5.2, and photos of it can be seen in figure 5.9. The photos have been taken from different directions to show that the color changes if one look at it from different directions. From above, these samples appeared more or less white. Light microscope images of the same sample can be seen in figure 5.10.

Sample #	Sphere concentration	Temperature
D1	1 wt.%	20.5±1textcelsius

Table 5.2: List of the solution used with method #2 and it's sphere concentration. The remaining content of the solution was DI-water.

As can be seen from the image, there are long cracks approximately $1\mu m$ wide running approximately parallel to the direction of growth, indicated with a white arrow in figure 5.10(a). These cracks are connected (or almost connected in many cases) by smaller cracks perpendicular to the direction of growth. When determining the average grain size, the perpendicular cracks were considered to connect the parallel cracks, even though they fell just short of doing that. With these guidelines, the average grain size was determined to be approximately 50x50μm. However, the uniformity along the sample (i.e. in the direction of growth) was poor. At the top the average grain size was about 10x10μm, but getting steadily larger towards the bottom where they were approximately 50x100μm. The images in figure 5.10 were taken at the bottom of the sample.

One important thing that should be noted, is that the grains seems to have been far larger, but have cracked up after being grown. Evidence of this can be seen from the SEM images in figures 5.11, where one can see that the crystalline orientation is unchanged across the crack. Note especially in the bottom figure the lone sphere sticking out of the structure on one side of the crack, and the corresponding vacancy on the other side of the crack. As the images clearly demonstrates, the cracks have split a previously larger structure along crystallographics directions parallel to the growth direction ([110] and [210] is shown in the top image.).

A thing to take note of from the light microscope images, is that there are long, $50\mu m$ wide areas of a different shade of green, bordering to yellow/white/blue, that runs along the direction of growth. In the image in figure 5.10(b) triangular

shapes can be seen on top of the opal. These triangles point in different directions on either side of the previously mentioned areas of another shade of green.

Experiments were done with several different solutions, but due to difficulties with the method these experiments were unsuccsessfull. The difficulties were mostly related to the reaction vessel used, as will be explained in the discussion. These difficulties, and the superior results obtained with method #3, resulted in the discontinuation of the work with this method.

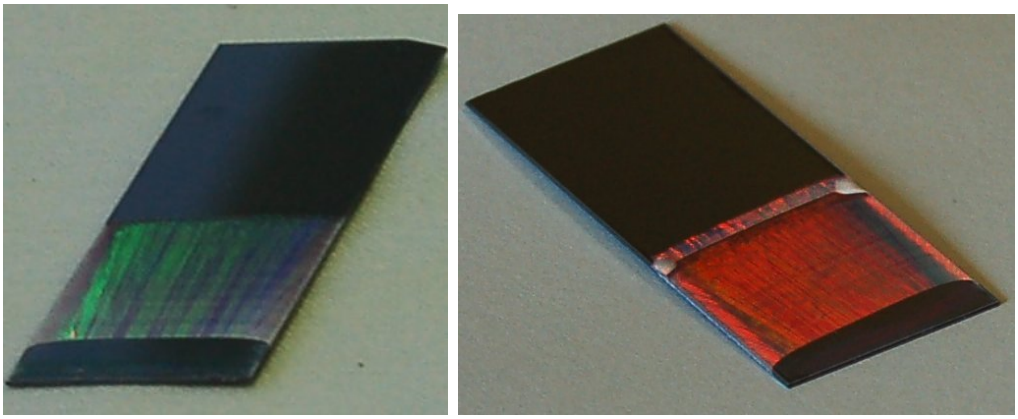

Figure 5.9: Photos of the sample made with method #2 using solution 2.1. The photos are taken at different angles to show that the color varies with the angle it is viewed from.

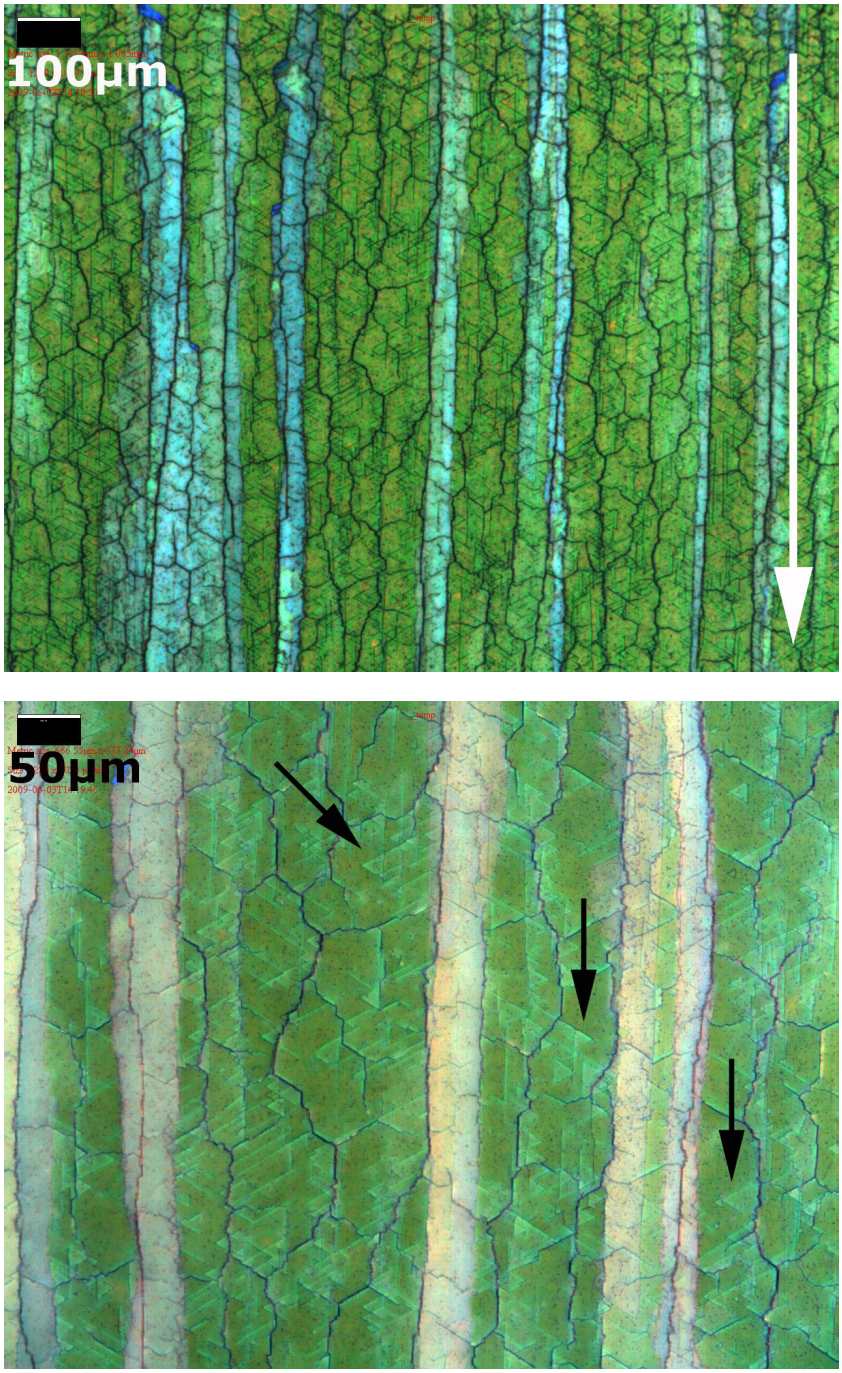

Figure 5.10: Microscope images of the sample made using solution 2.1 in table 5.2. The images were taken with a resolution of 10x (top), and 20x (bottom). Notice the triangular shapes on top of the opal, three of which are pointed out with black arrows.

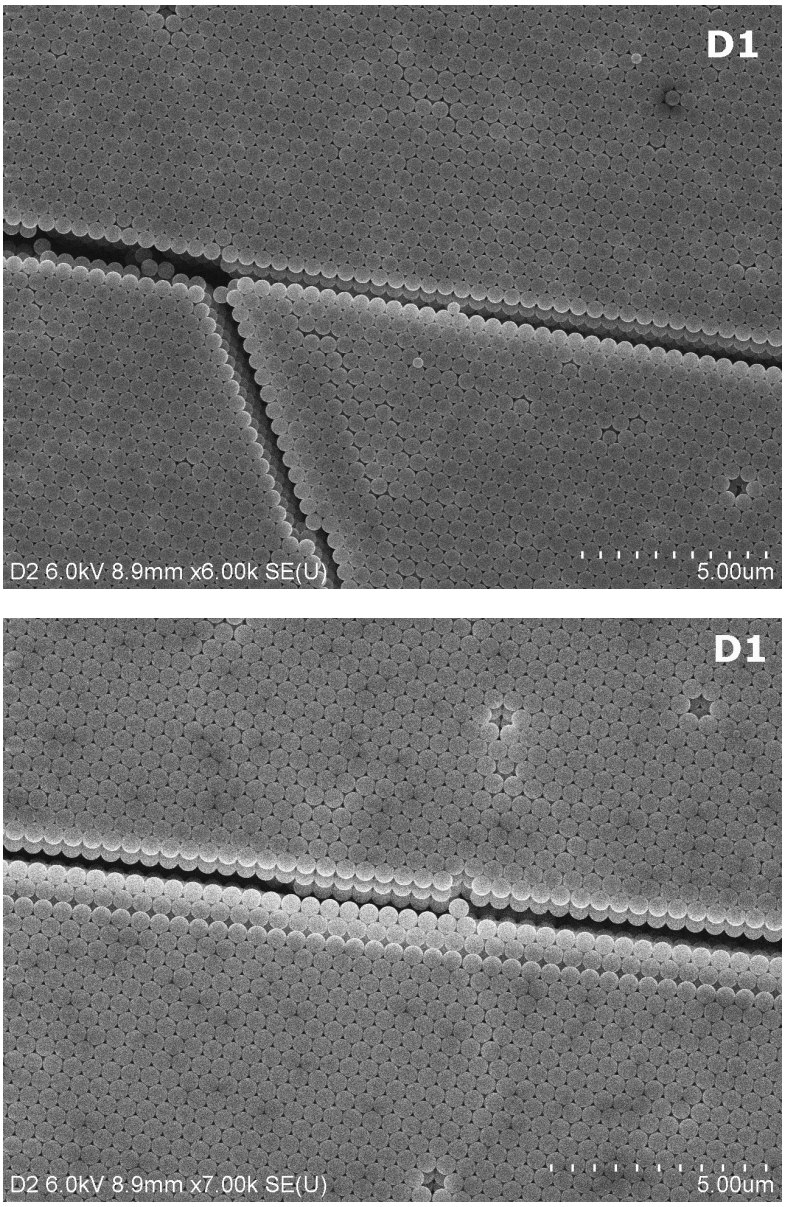

Figure 5.11: A SEM image of the sample made using method #2 with solution 2.1. A crack is indicated with the white arrow. Note that the crystalline order doesn't change across the crack. The brighter spheres in/along the crack is due to charging.

5.1.3 Method #3: Evaporation

With this method, a solution was prepared in a glass vial and placed in a pre-heated oven. A substrate was then held vertically in the solution, resulting in opal growth on it as the solvent evaporated. The evaporation led to a meniscus speed of 250nm/s at 50℃ and 500nm/s at 63℃. Note that one of the solutions was first used with method #2, before being diluted with DI-water and used with method #3. The reason for diluting the solution, was that this method produced thicker structures than method #2, as determined by initial growth attempts. This process did however yield poor control over the sphere concentration, as some of the spheres crystallize on the substrate and on the inside of the reaction vessel. Due to this, the actual sphere concentration in this solution is lower than listed. Table 5.3 lists the different samples made, and sphere concentration in the solutions used to make them.

Sample	Process temperature	Sphere conc.	# substrates in the vial
E1	50℃	$\leq$0.35 wt.%	1
E2	63℃	0.3 wt.%	1
E3	63℃	0.5 wt.%	1
E4	63℃	0.3 wt.%	2
E5	63℃	0.5 wt.%	2

Table 5.3: List of the different samples made with opal growth method #3. In some of the experiments there were two substrates in the same vial during opal growth, in an attempt to compensate for increased sphere concentration due to water evaporation.

Photos of samples E1-E3 can be seen in figures 5.12 -5.14, while figures 5.16-5.18 shows optical microscope images of the same samples. As for the sample made with method #2, these samples showed long cracks parallel to the direction of growth (white arrows in the figures indicates the growth direction). With higher temperature and sphere concentration, the amount of cracks perpendicular to the growth direction became significantly reduced, which can readily be seen by comparing figure 5.16 with figures 5.17 and 5.18. In addition, the cracks running parallel to the growth direction became longer, and straighter, and the distance between them was larger. Also, the width of the cracks changed when the temperature and sphere concentration was increased. For sample E1 the cracks were about $1\mu m$ wide, while for samples E2 and E4 this width increased to 2-3μm and to 4-5μm for sample E3 and E5, as determined with SEM. For samples E3 and E5 these measuements were done after sintering, i.e. heating to 95℃, which increased the width of the cracks some. In the most extreme cases, the cracks in sample E5 was widened to about $20\mu m$, but this was not the norm for the sample.

However, optical microscope images already show an increase for the unsintered samples, although possibly not as large as given above. The reason for sintering these samples before looking at them with SEM, was that the opal got lifted off the substrate due to charging and poor adhesion to the substrate. This problem also persisted after a thin conducting layer of carbon was deposited. A SEM image demonstrating this, can be found in figure 5.15, where the SEM was first focused on the rectangular bright area that can be seen, before zooming out and taking the image.

The grain size of the opals increased to 100x150μm at 63℃ from about 50x50μm at 50℃. One thing that was noticed about samples prepared with this method, was that the opals seemed whiter further down on the substrate. In the whiter regions, a lot of colorvariations were observed with the optical microscope. These variations could be just a a change in the shade of green, bordering to yellow, white and blue, or sharp transistion to blue or red. The observed color variations became more frequent further down on the samples, where they also appeared whiter to the naked eye. Examples of this will come later. The white areas were assumed to be closely related to an increase in opal thickness, due to the expected increase in sphere concentration as water evaporates. This assumption was also based on the fact that higher initial sphere concentration resulted in whiter samples.

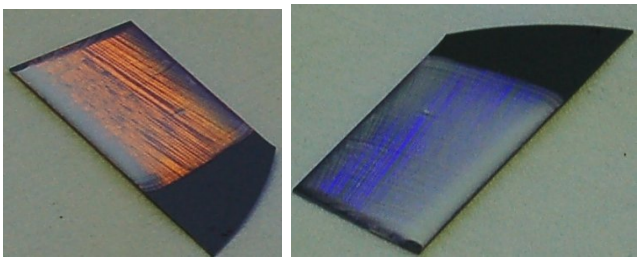

Figure 5.12: Sample E1. The substrate was slightly tilted to one side during growth, so the opal wasn't grown exactly prallel to the substrate edge.

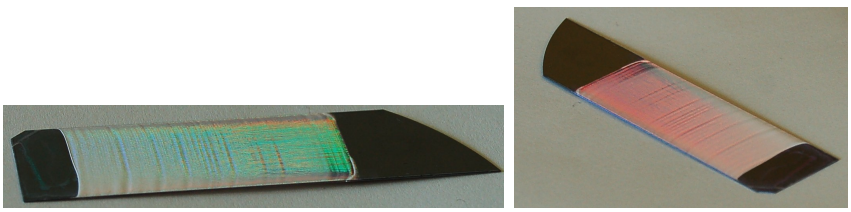

Figure 5.13: Sample E2. Note the whiter appearance of this sample compared to E1.

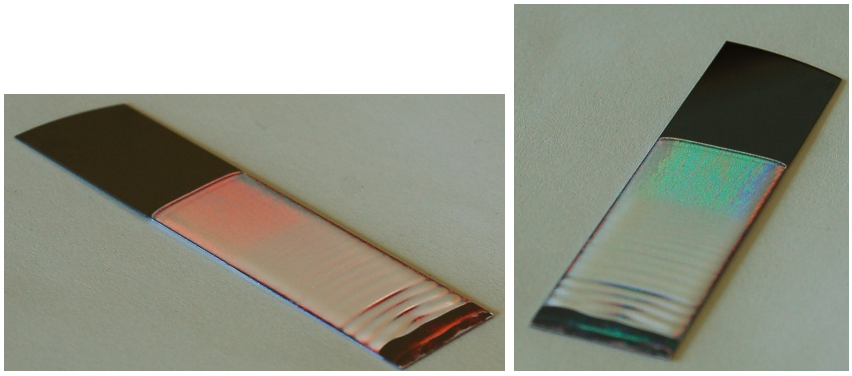

Figure 5.14: Sample E3. Note that the sample appears increasingly whiter towards the bottom.

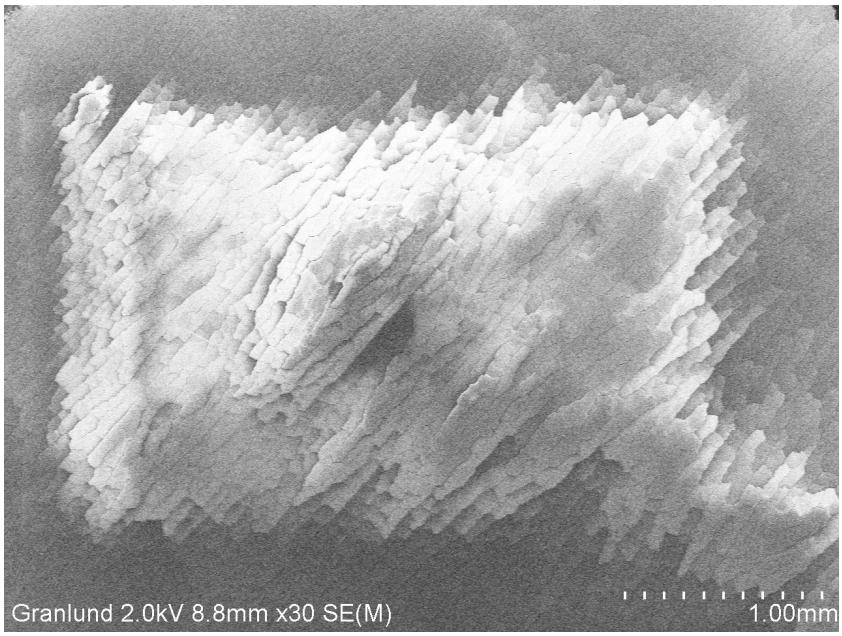

Figure 5.15: Before taking this image, the SEM was zoomed in on the rectangular, bright area that can be seen. After looking at this area for a while, noticing how the structure bent up from the substrate, the SEM was zoomed out and a image was taken. This was a problem for unsintered samples.

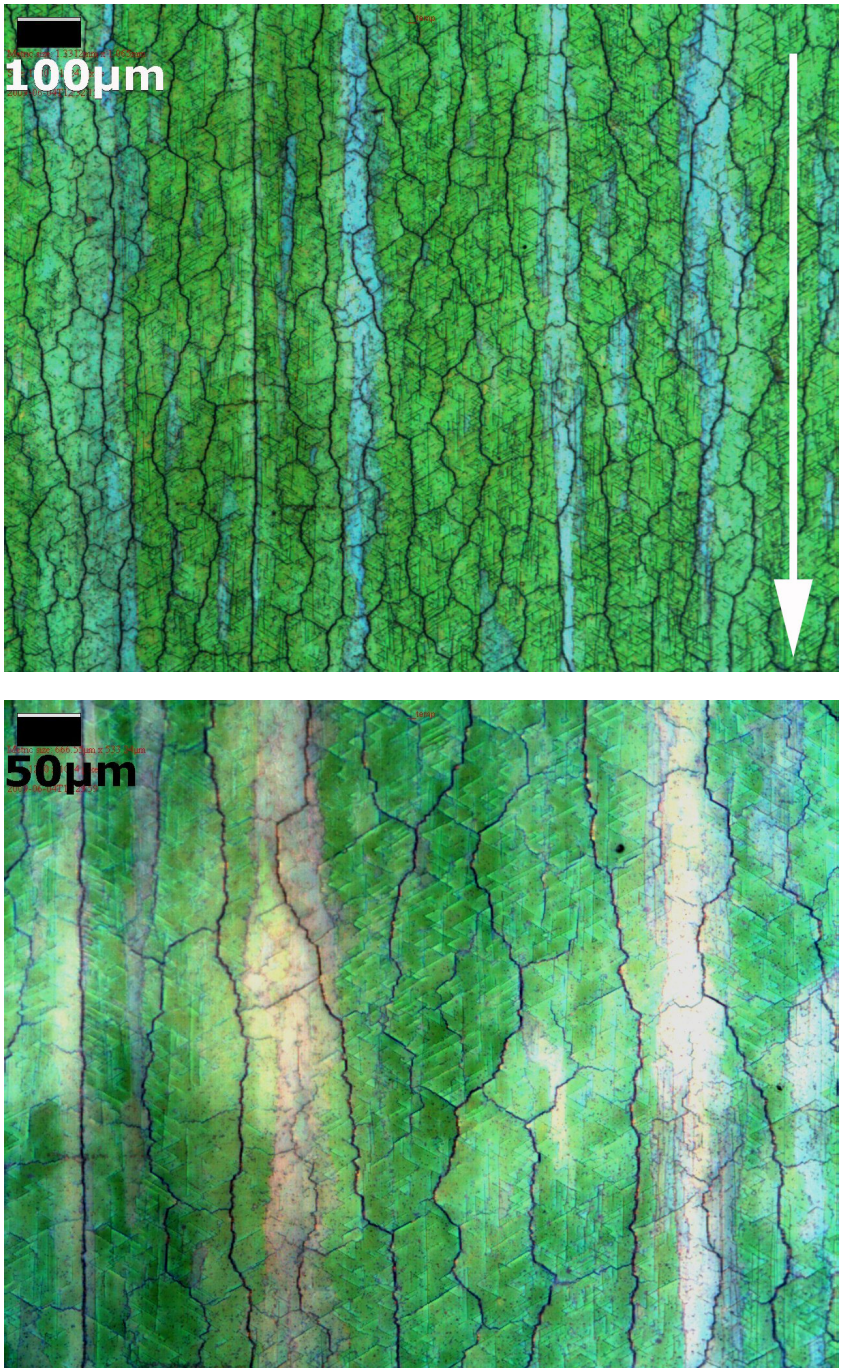

Figure 5.16: Images of sample E1. The images are taken with a resolution of 10x (top) and 20x (bottom). Notice the triangular shapes that can be seen in the bottom image, which was also seen for sample D2.

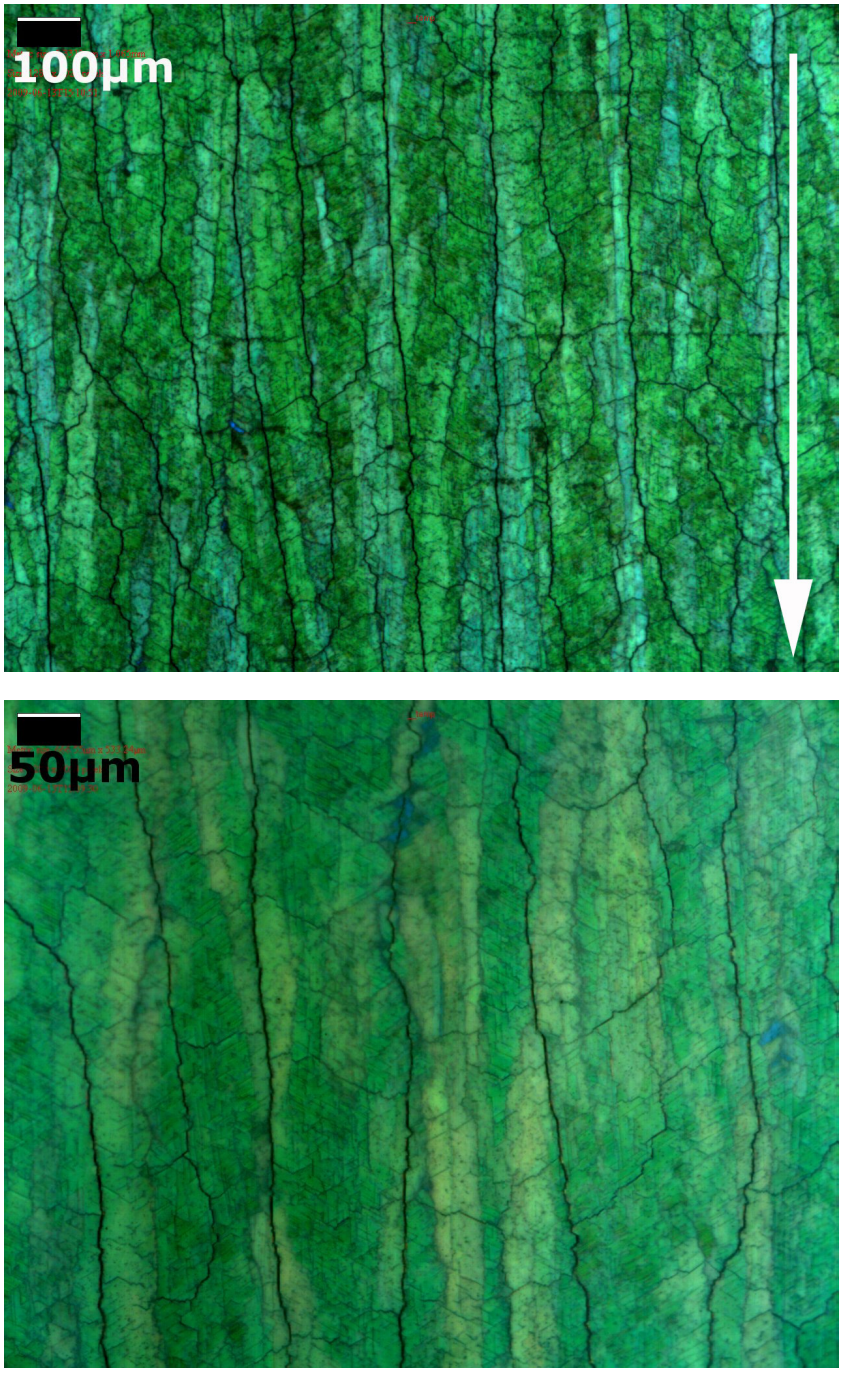

Figure 5.17: Images of sample E2. The images are taken with a resolution of 10x (top) and 20x (bottom). A clear reduction in the amount of cracks from the sample made at 50℃ was observed.

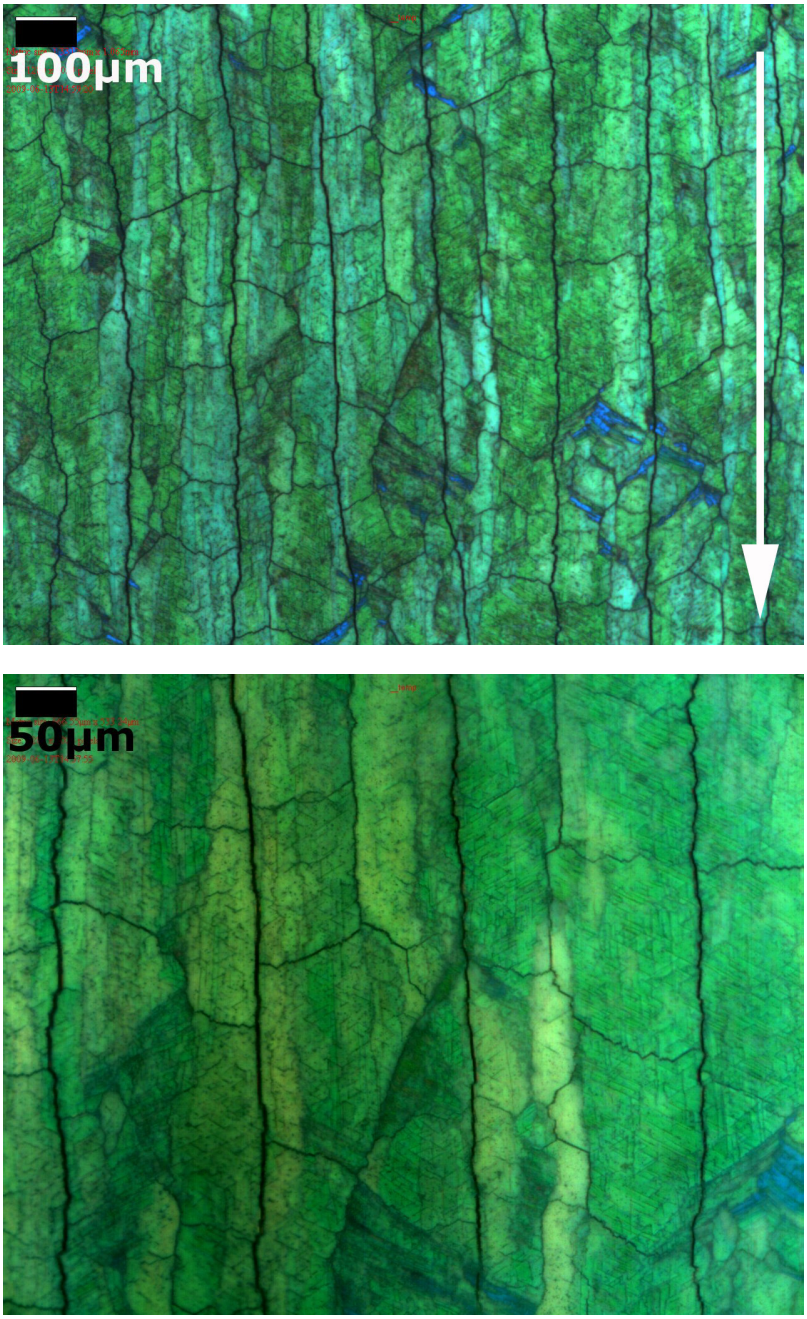

Figure 5.18: Images of sample E3. The images are taken with a resolution of 10x (top) and 20x (bottom). A further increase in grain size, and a reduction in the amount of cracks, was observed with the increased amount of spheres in the solution. Notice the small blue areas in these images. Such color variations became more frequent towards the bottom of the sample. The images here was taken high up on the sample, where the coloring could be seen with the naked eye.

Method #3: Evaporation, continued

After having done the experiments above, two properties in particular were desired to get a better control over: opal thickness uniformity and grain size. This was attempted with two experiments.

In the first experiment, which was done to achieve a uniform thickness, two substrates were placed in the solution together so that a larger amount of spheres would crystallize. Before presenting the results, something should be said about the SEM images obtained here. As the samples had to be coated with a thin layer of conducting carbon to be imaged with SEM, making them unsuitable for further processing, one of the samples were imaged before silicon deposition and calcining, but after sintering, and the other was imaged after. The idea with having more than one substrate in the solution, was that this could offset the increased sphere concentration due to water evaporation. 0.3 wt.% spheres was chosen for this experiment, as for sample E2, as it would be easier to visually verify that the thickness was uniform with a thinner opal. Photos of one of these samples can be seen in figure 5.19, and optical microscope images in figure 5.21. As can be seen from the photo, the opal thickness seem to no longer increase towards the bottom, based on coloring, i.e. it doesn't change color or becomes white. This was also observed with the optical microscope, where the lens no longer needed translation towards or away from the sample while moving along it. The opal also seem to have become thinner overall compared to sample E2, which was placed alone in the vial, but the distance between the cracks parallel to the direction of growth stayed about the same.

Unfortunately, the twin sample from this experiment was not as good as sample E4, so the SEM images of this sample is left out as it wasn't considered to be representative for sample E4. Instead a SEM image of sample E2 is shown in figure 5.23, although being of poor quality as the sample wasn't sintered. The image is taken at the top of the sample.

The second experiment was done with 0.5 wt.% spheres, and yielded a thicker opal, which once again seemed to be of even thickness. Compared to sample E3, which was made with the same sphere concentration, but with only one substrate in the vial, the distance between the cracks parallel to the growth direction increased. In addition, the sample seems to have an increased overall thickness compared to sample E3, with the resulting white appearance as can be seen from the photo in figure 5.20. Optical microscope images of the sample can be found in figure 5.22, and as can be seen, the surface show random color variations, which was typical for the thicker structures. SEM images of the twin sample, which was of the same quality, can be found in figures 5.24-5.27. In figure 5.24 a crack is shown of about 4-5μm in width. Notice that the crystallographic orientation doesn't change across it. The white arrow in figure 5.25 indicates a fcc structure grown in

the [101] direction (magnified in the inset), while the black arrows indicates line defects joining to make triangle like defects. In figure 5.26 a grain of the opal that seems to have grown along the [110] direction is shown. Figure 5.27 shows two examples of point defects that occured; vacancies and spheres of the wrong size that have been incorporated into the structure.

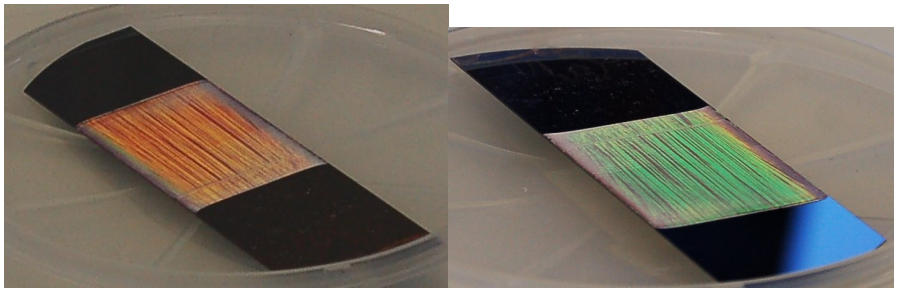

Figure 5.19: Photo of sample E4. As can be seen, the sample seem to be of more uniform thickness than before.

Figure 5.20: Photo of sample E5. No coloring was visible.

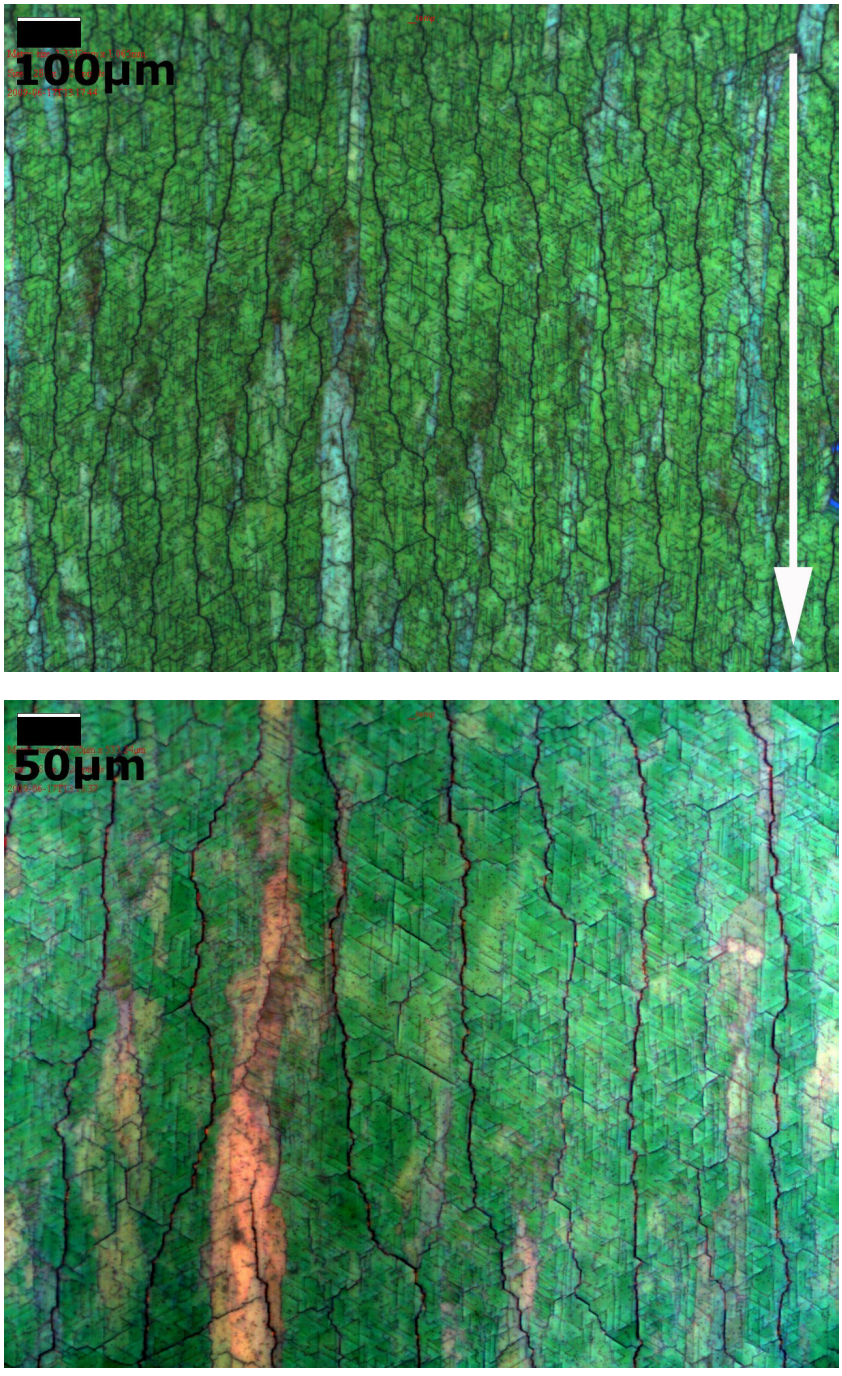

Figure 5.21: Images of sample E4. The experiment was done with two substrates in the glass vial, to obtain an opal of more uniform thickness, which appeared to be a success.

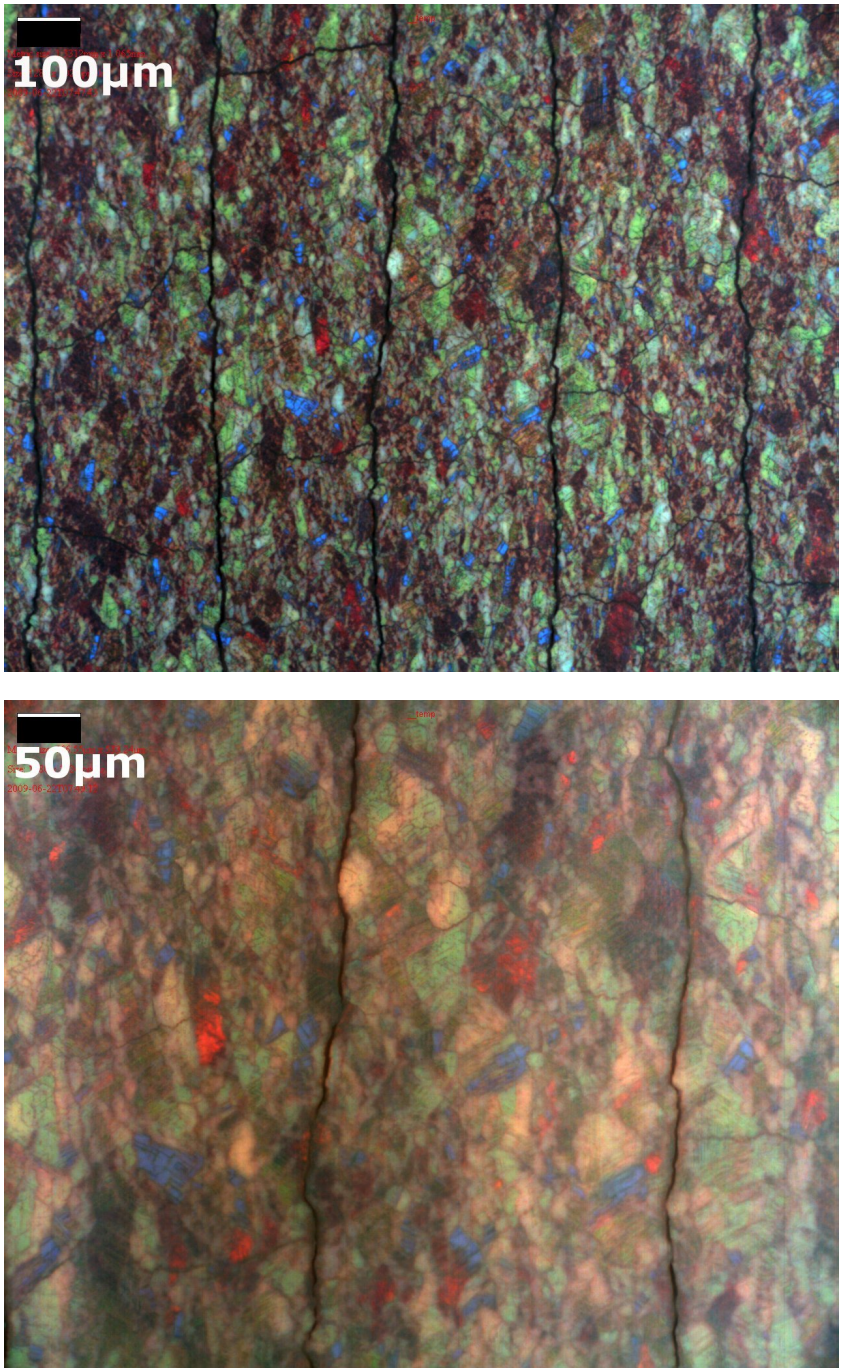

Figure 5.22: Images of sample E5. The experiment were done with two substrates in the glass vial. Note the random variation in color of the surface, and especially the bright blue and red areas.

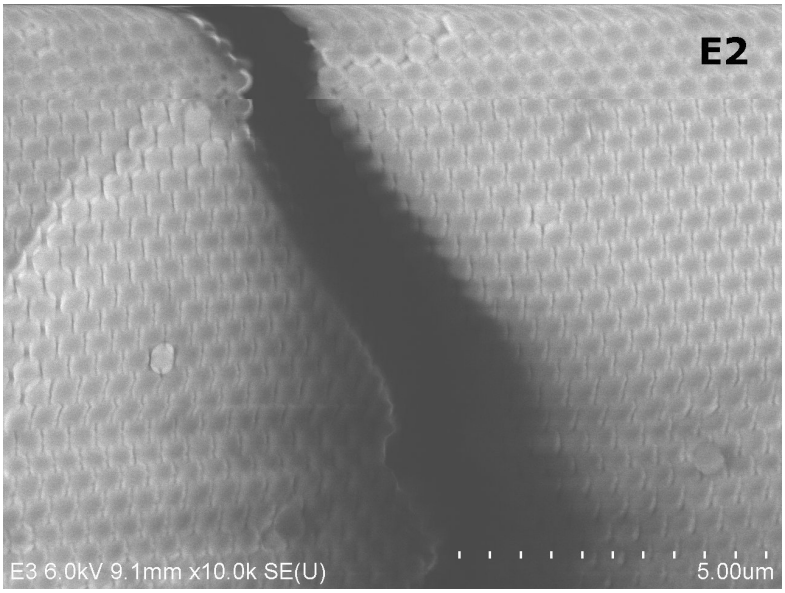

Figure 5.23: SEM image of sample E2 showing a crack of 2-3μm in width. Note that the crystallographic orientation doesn't change across the crack.

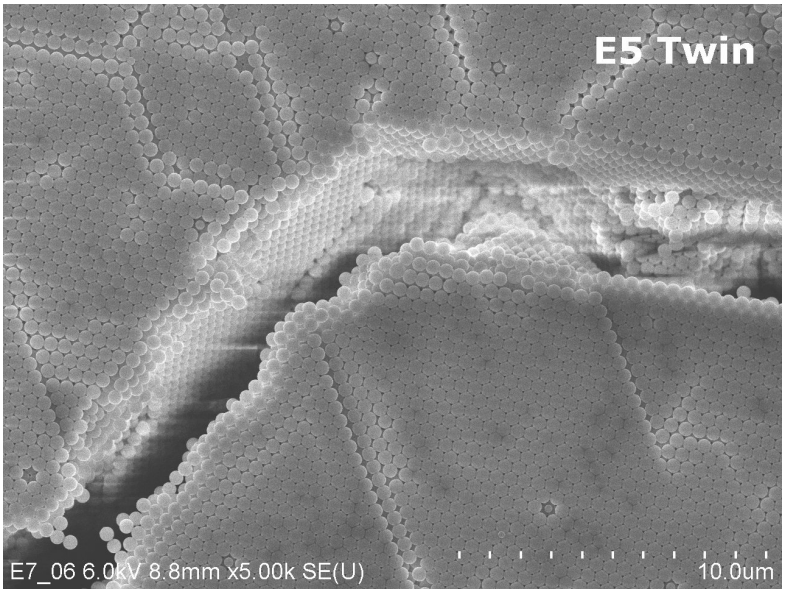

Figure 5.24: SEM image of E5s twin sample showing a typical crack of 4-5μm. Note that the crystallographic orientation doesn't change across the crack. Line defects can clearly be seen on the surface. Some of the sphere appears brighter due to charging effects.

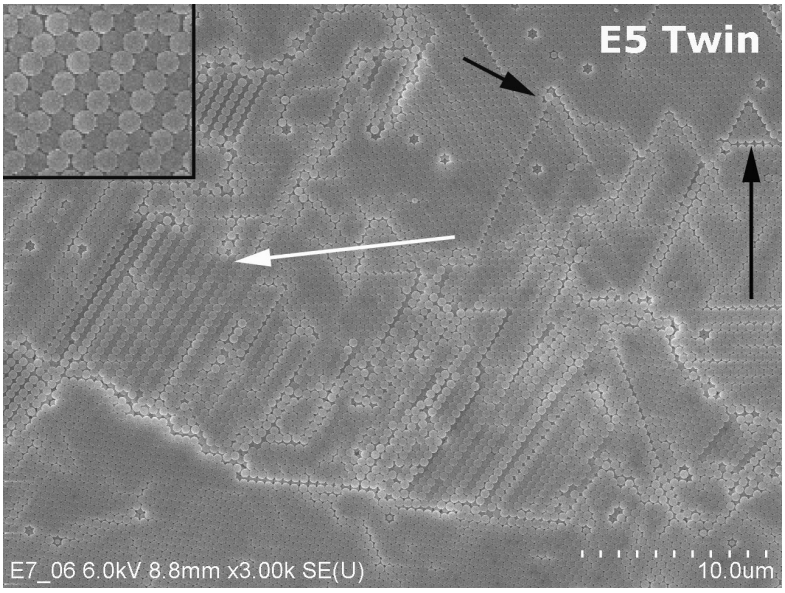

Figure 5.25: SEM image of E5s twin sample showing line defects forming triangular shapes (black arrows), which could also be seen from the images taken with an optical microscope, and an area that seems to have grown in the [101] crystallographic direction (white arrow and inset).

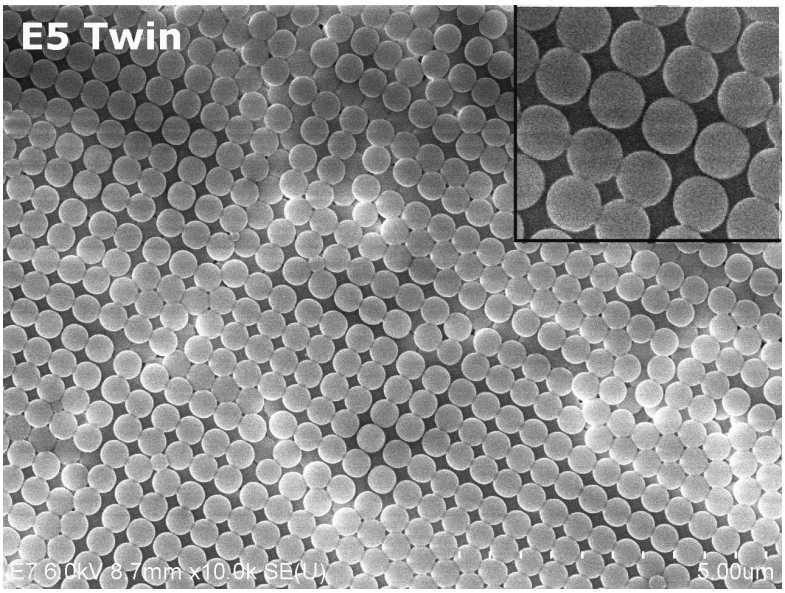

Figure 5.26: SEM image of E5s twin sample showing an area that seems to have been grown in the [110] crystallographic direction. Inset shows a magnified area from the same image.

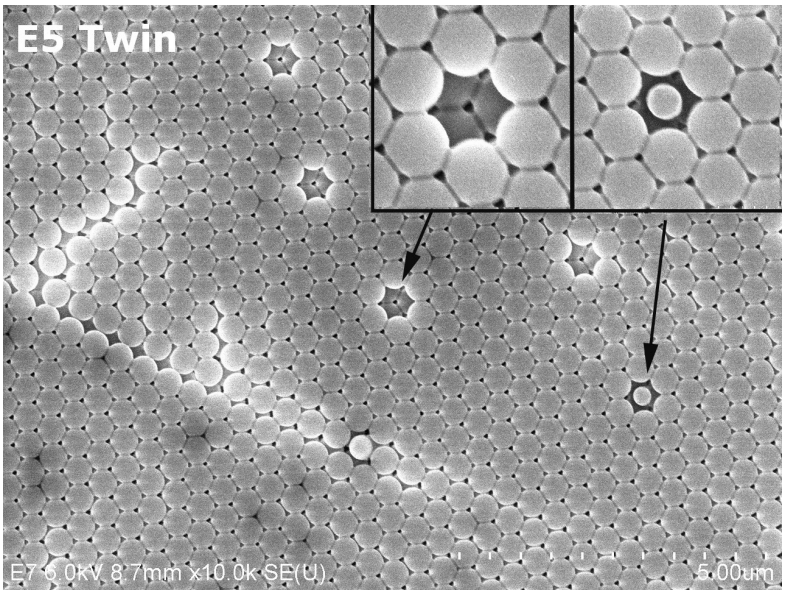

Figure 5.27: SEM image of E5s twin sample showing two kinds of point defects frequently seen; vacancy and a sphere of a deviating size.

5.2 Opal inversion

Opal inversion was performed in three steps: (1) sintering of the opal to make the spheres adhere better to each other, (2) silicon deposition with PECVD to fill in the gaps between the spheres and (3) sphere removal in an oven at 600℃. These steps are described in more detail in Chapter 3.3: Opal inversion.

Sintering had three notable effects. Firstly, the cracks were widened, an effect most visible for the thickest structure, i.e. E5, where some of the cracks widened to about $20\mu m$ and could be seen with the naked eye. Optical microscope images of the samples after sintering can be seen in figure 5.30, while a photo of the thickest sample can be seen in figure 5.28. The photo only shows a 1x2cm area of the sample, and does not represent the sample average. Secondly, the spheres seemed to fuse together at the contact points, as can be seen from the SEM images in figure 5.29, where the top image was taken before sintering and the bottom image after. Thirdly, the opals adhered better to the substrate, which was very important when one wanted to take SEM images of them. Without the sintering step the opals lifted off the substrate during SEM due to charging and poor adhesion to the substrate, a problem that persisted even after a thin layer of conducting carbon had been deposited on them.

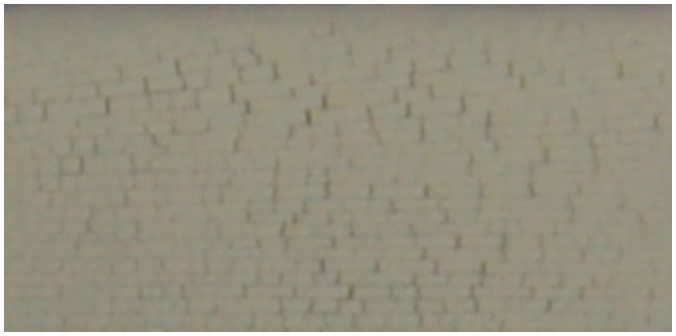

Figure 5.28: A photo of a thick sample (E8) after sintering. As can be seen, the cracks between the grains are now wide enough to be seen by the naked eye. The area shown is about 1x2cm.

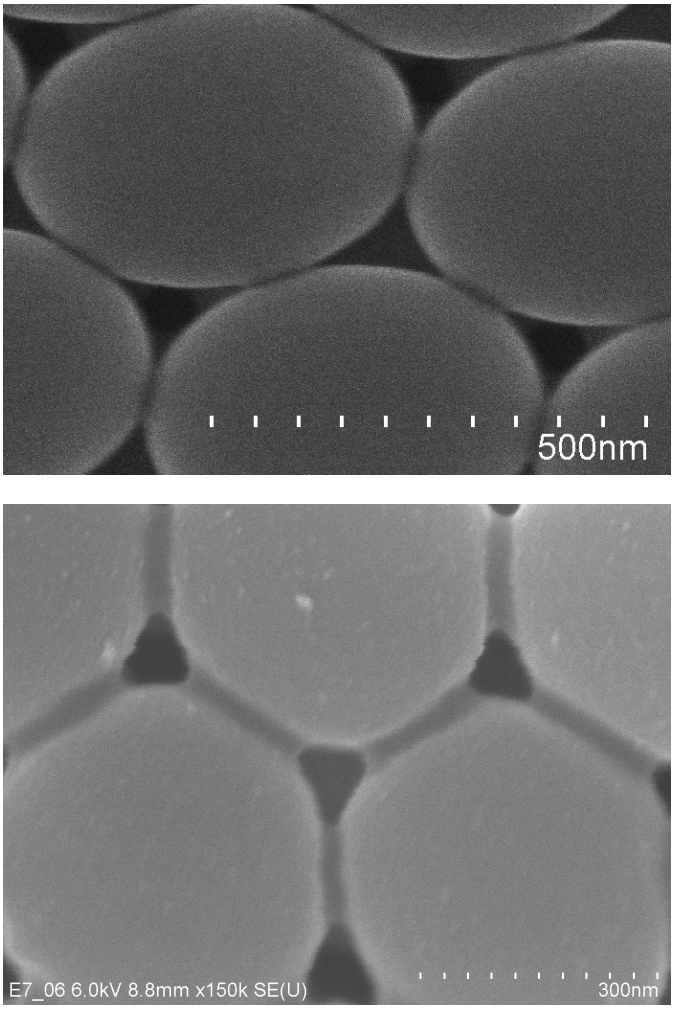

Figure 5.29: SEM images taken before (top) and after (bottom) sintering. As can be seen, the spheres have fused at the contact points after sintering. The spheres in the top image can be seen to be sligtly deformed, but this is only the result of the opal slowly moving on the substrate as the image was taken.

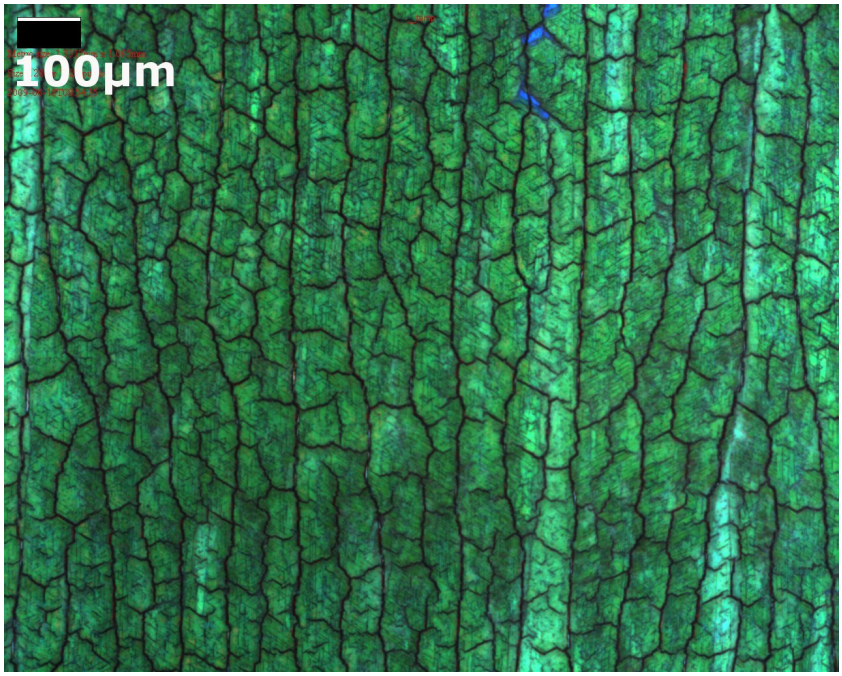

(a)

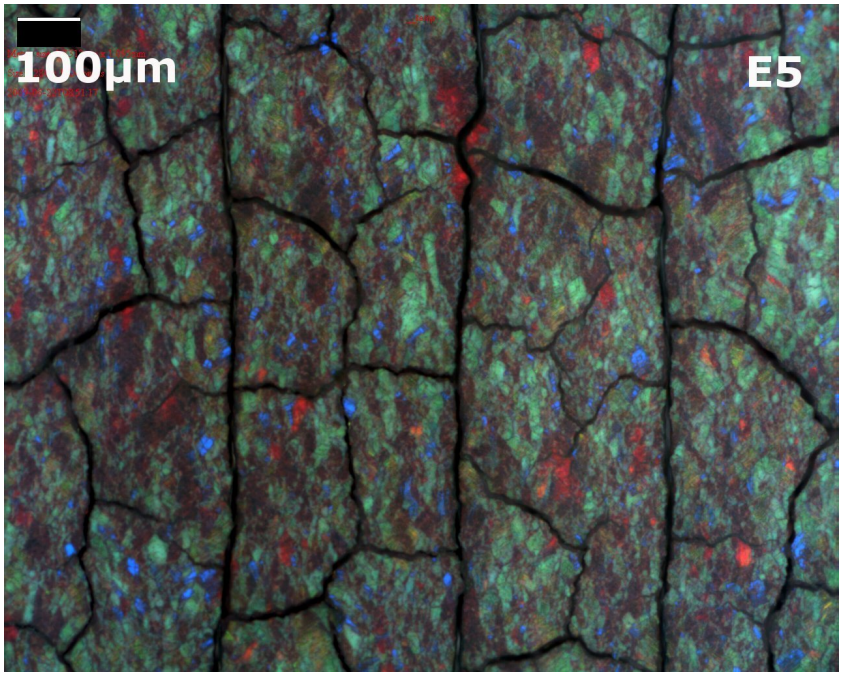

(b)

Figure 5.30: Opt.micr. images of sample E4 (top) and E5 (bottom) after sintering. As can be seen, the cracks have now been widened some.

Opal inversion continued

After sintering, silicon was deposited and the samples were calcined. Photos of the samples before and after calcining can be seen in figures 5.31 and 5.32. Optical microscope images taken after silicon deposition can be found in figures 5.33, and as can be seen, the opals are now covered with a layer of silicon. Whether the silicon have been deposited inside the structure or not, is impossible to say from these images. One thing that was noticed, with the naked eye, was that there was some areas that were colored. These areas were found at the part of the sample that had cracked the worst during sintering. A photo and a microscope image can be found in figures 5.34 and 5.35 respectively.

After calcining, something seemed to have happened to the silicon; it no longer formed a continous film, but was instead lumped together. This was most notable for the silicon deposited on sample E4, while the changes for sample E5 is less pronounced, as can be seen from the photos in figures 5.31 and 5.32 and optical microscope images in figure 5.36. Notice the colored areas along the edges of the grains on sample E5. This coloring was not observed for sample E4. The previously mentioned colored areas that were visible to the naked eye, could no longer be seen after calcining, but the optical microscope image reveals that they are still there, but that the main part of them now is covered with a thin, slightly transparent material. If one takes a closer look, the colored structure can be barely seen under this layer, as shown in the inset. This was only seen at the spots where there before calcining had been a colored spot, as seen in the optical microscope image in figure 5.35.

With the attempted inverted samples, the first successfull attempts at finding out how thick these opals were, were done. Crossectional images of these samples can be seen in figure 5.37, where the top image is from sample E4 and the bottom image from sample E5. As can be seen, sample E4 have a thickness of approximately 16-18 layers of spheres, while sample E5 was about 30-40 layers thick. Due to the difficulty with obtaining good crossectional images of sample E5, it was impossible to get an accurate estimate. Sample E5 was very fragile, and the scalpel that was used to make cuts in was too crude an instrument to provide areas that could be used for high quality crossectional images.

In the crossectional image chosen from sample E5 inverted structures were observed, as marked, which was fcc in nature. A close up can be seen in figure 5.38, showing that the structure is fcc, seen along the [110] crystallographic direction. Figure 5.39 shows a fcc (or hcp) inverted structure seen along the [111] crystallographic direction, found elsewhere on sample E8. However, inverted areas were the special case, as the spheres seemed to mostly have remained intact after calcining.

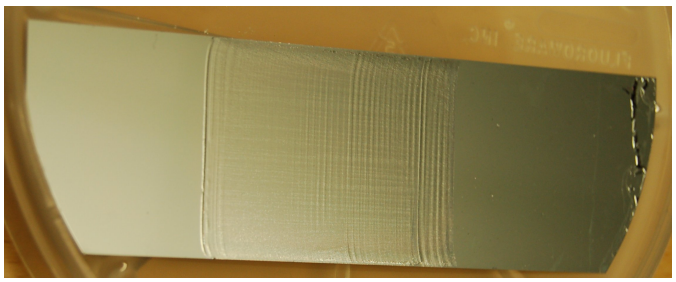

(a)

(b)

Figure 5.31: Photo of sample E6 after PECVD step (top) and after calcining at 600℃ (bottom).

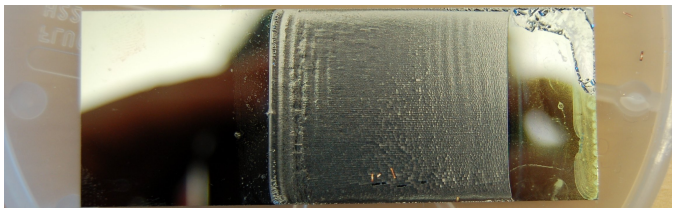

(a)

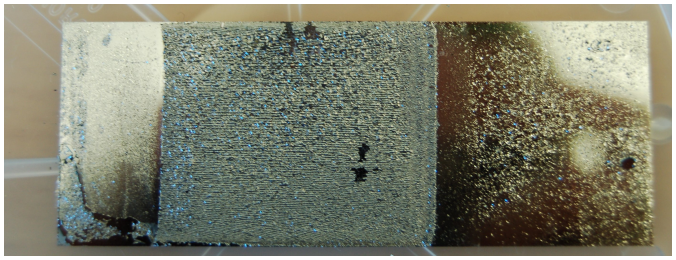

(b)

Figure 5.32: Photo of sample E6 after PECVD step (top) and after calcining at 600℃ (bottom). The darker spots on the sample are cuts made with a scalpel prior to SEM analysis.

(a)

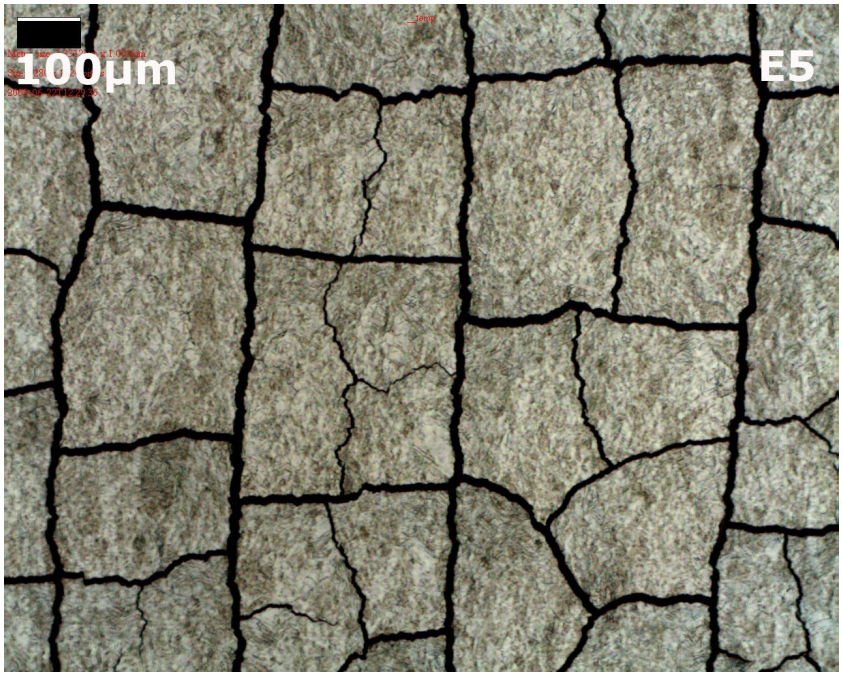

(b)

Figure 5.33: Image of the sample E4 (top) and E5 (bottom) after silicon deposition. As can be seen, silicon now covers the surface of the opals.

Figure 5.34: Photo of sample E5 after PECVD, showing three small colored areas.

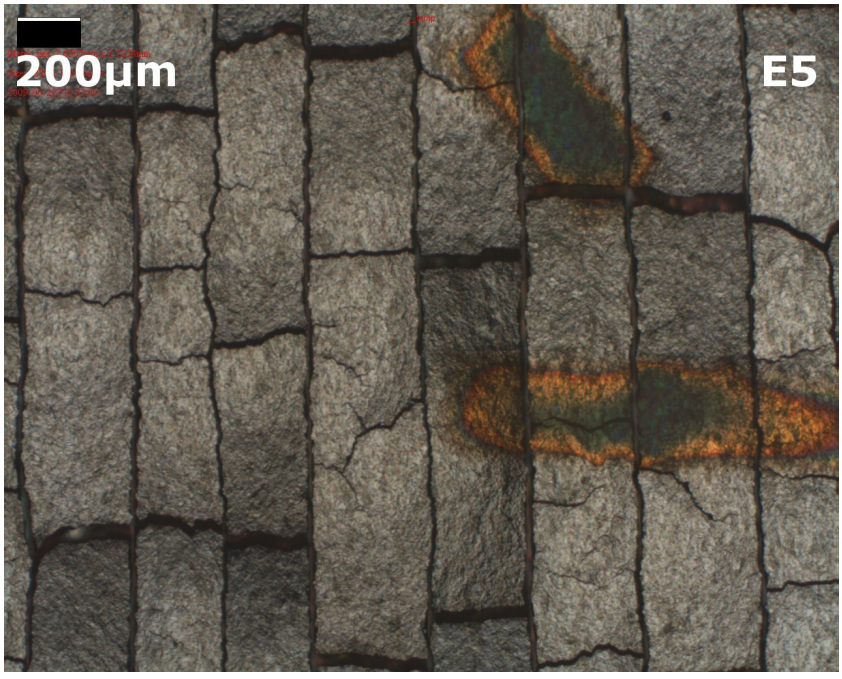

Figure 5.35: Optical microscope image of sample E5 after PECVD, showing the same area as in the photo in figure 5.34

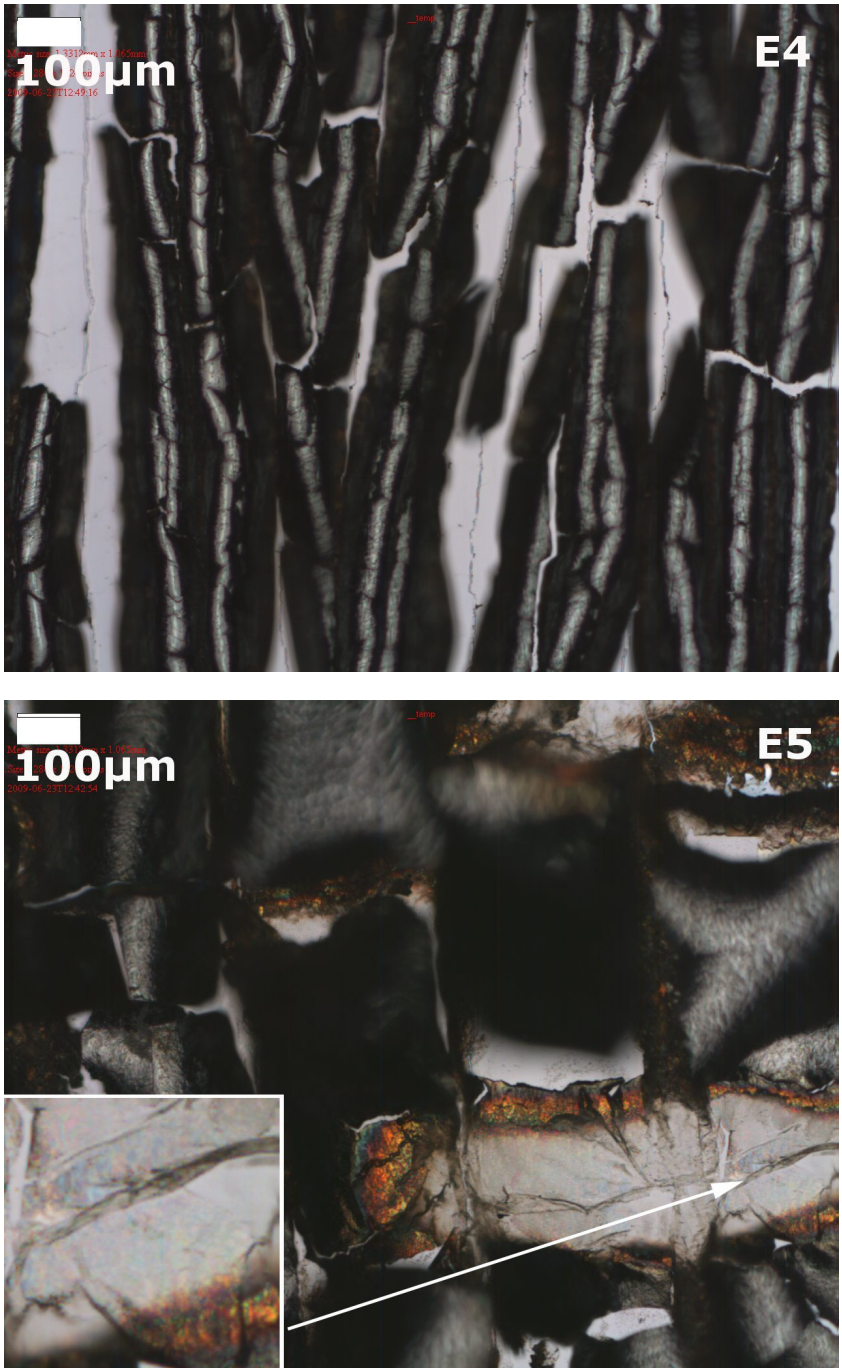

Figure 5.36: Images of sample E4 (top) and E5 (bottom) after calcination. Especially on sample E4 there seem to be silicon lumped together on top of the structure. Notice the colored areas along the edges of the grains for sample E5, and that the coloring continues underneath the brighter area, as shown in the inset.

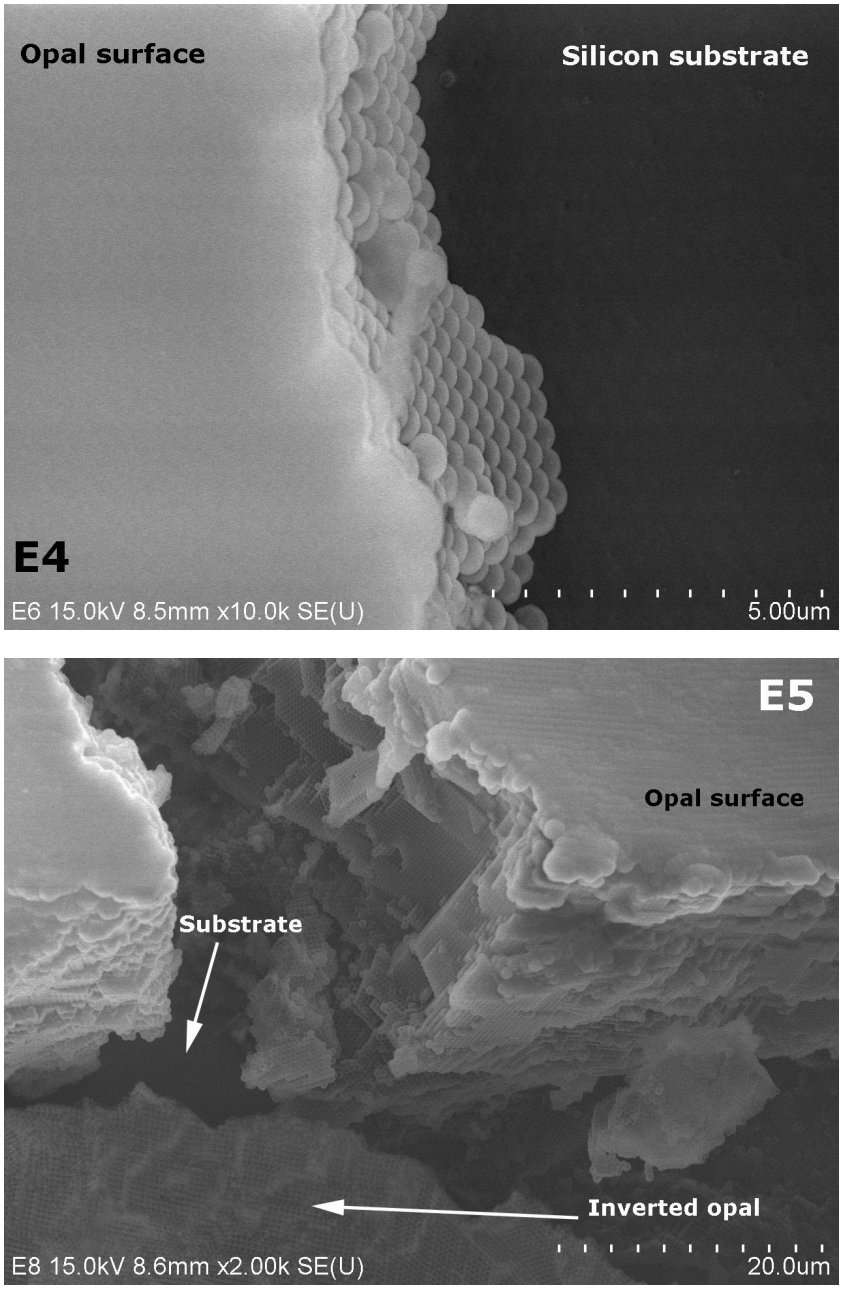

Figure 5.37: Crossectional images of sample E4 (top) and sample E5 (bottom). Opal thickness was estimated to be 16-18 layer for sample E4 and 30-40 layers for sample E5. The crossections confirm that the structure is indeed fcc. In the image of E5, an inverted area is marked. Magnified images of this structure can be found in figure 5.38.

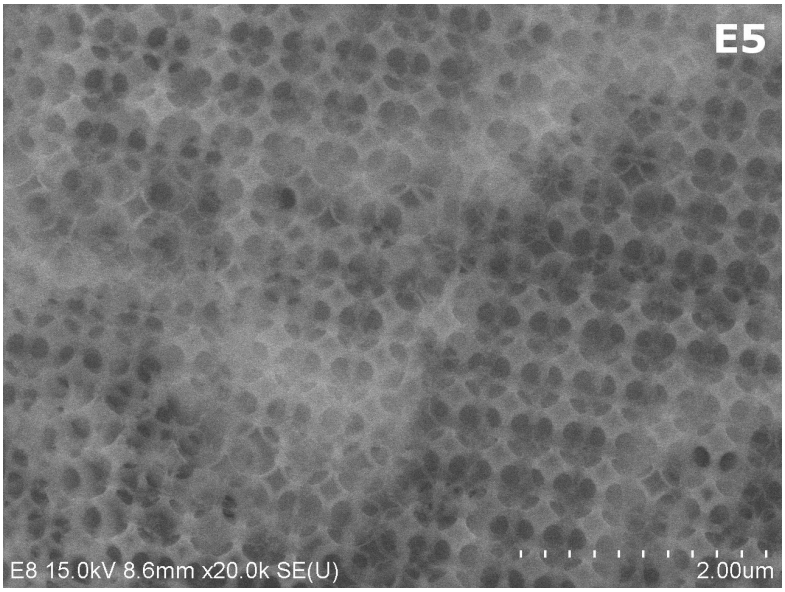

Figure 5.38: The image shows an are of sample E5 that has been inverted. The inverted opal is seen along the [110] crystallographic direction. The underlying structure can be glimpsed through the holes.

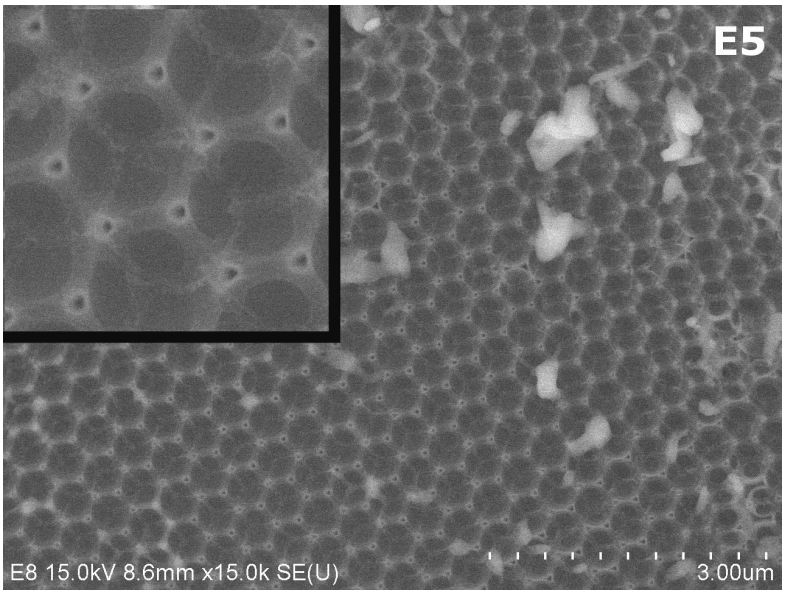

Figure 5.39: The image shows an are of sample E5 that has been inverted. The inverted opal is seen along the [111] crystallographics direction. The inset shows a magnified version, where the underlying structure can be seen, confirming that the structure is either fcc or hcp fcc.

Chapter 6

Discussion

In this chapter, the results from the reflection simulations, opal growth methods and inversion process will be discussed.
In the discussion of opal growth method #2, the main focus will be on the method, while the discussion of the opals themselves will be done while discussing method #3. This is because most of the opals in question were made with method #3, and that the discussion applies equally well for the opals made with method #2.

6.1 Reflection simulations

The reflection simulations were done for three reasons; (1) to investigate the width and the placement of the reflection peaks in wavelength, (2) to see if the measured reflection could be used to determine whether a grown structure were fcc or hcp, and (3) to show the scalability of Maxwell's equation, and how this can be used to shift the reflection spectra simply by changing the size of the spheres used to make the inverted opal. Reflection spectrums were only simulated for normal incidence on the [111] crystallographic direction, as MEEP, the simulation software, proved to be unsuited for other incident angles.

A couple of things about the general results of the simulations need commenting first though. First of all, the obtained reflection spectra had a shift in frequency relative to the band diagram used as a referance of about 0.05, or 100nm in wavelength. This was assumed to be due to the finite nature of the structure in the direction perpendicular to the substrate, and the interface to air and silicon on either side of it in that direction. Vlasov et al. [8] calculated the band diagram for a similar structure, showing the same shift in frequency, supporting this assumption.

Secondly, the simulated spectra had some small oscillations and some larger spikes in it, which was thought to be due to interference between light still trapped

in the structure at the end of the simulation and light that had escaped. These effects were most notable for wavelengths corresponding to the bandgaps, excempting the lowest one. The light trapped was registered as a loss, which was calculated as 1-R(eflectance)-T(ransmission). This hypothesis was strengthened by a simulation that was allowed to run far longer, which showed a substantial reduction in the loss, but with a few spikes remaining at wavelengths corresponding to the bandgaps of the structure.

The width and placement of the reflection peaks were seen to coincide well with the expected bandgaps, although with the mentioned shift. The peaks became well defined after only 6 layers of spheres, while the thinner structures had a less sharp respons. Around $\lambda = 1500$nm the reflection peak of the first incomplete bandgap was seen, with a FWHM of about 430nm and a reflection of 93%, which at first glance should make it ideal as a rear reflector. However, simulations done by Bielawny et al. [45] shows that only a fraction of the light is reflected in a non-specular manner, so the usefulness of this reflection peak is uncertain.

Reflection peaks corresponding to BGs at higher frequencies were shifted to cover most of the wavelengths in the near-visible part of the IR-spectrum (800-1200nm), by scaling the structure. These peaks had a reflection of unity, i.e. all the light is reflected, which should make them perfect as a reflector. However, there are dips in the reflection spectrum between these peaks where almost all the light is transimtted, and the individual peaks are not broad enough to cover the entire spectrum from 800-1200nm. A possible way to circumvent this could be to grow two structures, one on top of the other, that are matched to reflect all the light. This may however be a bit far fetched, both due to the difficulties with realizing it and added process steps, which increases the cost of making cells. However, should this approach yield a substantial increase in cell efficiency, an increase in the production cost may be worth it.

In the simulations, it was also shown that the reflection spectrum of the structure could be shifted in wavelength by simply changing the size of the spheres used to make it. This is an effect of the scalability of Maxwell's equations, and makes the result obtained for spheres of one size valid for all sizes, although with a shift in wavelength.

The last thing that should be noticed about the simulations, is that they can not be used to determine whether an opal is grown with hcp or fcc ordering, as the reflection spectra of the two near identical.

All in all the simulations showed that the inverted opal exhibit the necessary reflection peaks to be used as a rear reflector in solar cells, although its usability for thinner wafers still need further investigation. It was also seen that the reflection spectra couldn't be used to determine whether the grown opals were fcc or hcp.

6.2 Opal growth method #1: Diffusion

With this method, wafer sized crystalline monolayers were successfully grown using Ugelstad spheres. This was done by diffusing spheres situated in an ethanol containg solution, onto a water film. The diffusion of spheres was intiated by bringing the sphere solution, placed on a wafer, into contact with a water film, which covered a seperate wafer. The spheres diffused onto the water film in a fan like fashion all the way across it, upon which they began to crystallize. No crystallization of spheres was observed before they had diffused across the film. Diffusion and crystallization kept on until almost the entire film was covered, which took about 5 minutes. Although the process took 5 minutes, a sphere only used a few seconds to diffuse across the water film, so the time it took to cover the film was limited by the amount of spheres diffusing onto it per second.

After the spheres had formed a crystalline monolayer on the water film, the water was allowed to evaporate, which took about 90 hours when the samples were placed under a plastic cover. The plastic cover was important for high quality monolayers to be left on the wafer; without the cover, the evaporation took about 24h and yielded monlayers of significantly reduced quality. This was thought to be a combination of reduced evaporation rate, and protection from air fluctuations in the lab. For most of the solutions tried, wafer size polycrystalline monolayers were easily grown, with the best samples having an average grain size of 250-300μm^2.

The developed method was based on the method used in the preceeding project [34], and the goal here was to determine the ideal amount of spheres and ethanol in the solution. Sphere concentration was varied from 23 wt.% to 4 wt.%, with a constant ethanol concentration of 4 wt.%, and was found to have only small effects on the quality of the crystalline monolayer. The grains became slightly larger, from about 75μm^2 with 23 wt% spheres to 100μm^2 with 4 wt.%, and the amount of extra spheres on top of the monolayer decreased slightly with less spheres in the solution. As the improvement was very small, it was suspected that the variation between these samples could be due to random variations in the experiments. Foremost among these variations were the amount of spheres diffusing onto the film per second. The wafers were brought into contact by hand, resulting in some variations in the size of the contact point, which again affected the amount of spheres that could diffuse onto the water film per second (this difference could easily be seen by the naked eye). Other possibilities are vibrations in the lab, which varied from day to day, and temperature fluctuations. The latter seems improbable, as the tempereature was held at 20.5°C±1°C, but the former could have a substantial effect as the amount of vibrations varied dependending on how much traffic there was in the lab.

The other parameter that was investigated, **ethanol concentration**, had a **large** effect on the crystalline quality of the monolayers. Ethanol concentration

was varied from 16 wt.% to 2 wt.% with a constant sphere concentration of 2.5 wt.%, and the average grain size increased from $75\mu m^2$ to close to $300\mu m^2$ for 2 wt.% ethanol. For lower ethanol concentrations, the diffusion process didn't start, and a mixing of the sphere solution and the water film happened instead. To explain these results, more in depth discussion is needed, so we'll return to this later.

First, the prerequisite for the diffusion process was ethanol. Without or with too little ethanol, the diffusion process failed to start, and naturally no crystalline monolayer could be formed. To further investigate the effect of adding ethanol to the sphere solution, an additional experiment was done. A vial was filled half full with water, and a sphere solution was carefully added. With a pure sphere solution, i.e. no added ethanol, most of the spheres gently sank to the bottom, while a very small amount resided in a thin layer on the surface (less than one cm^2 in area). When ethanol was added to the solution however, the spheres rapidly distributed themselves in a large, thin layer on the water surface, although without any visible crystallization. This layer could easily cover the entire surface as long as enough spheres were provided. In addition, when ethanol-containing solutions were added more roughly, i.e. with a downward force, or below the surface, they didn't sink, but started to rise and spread on the surface. This effect did however depend on the amount of ethanol; with a small of amount of ethanol, some of the spheres started to sink, but by increasing the amount of ethanol, almost all of the spheres rose. These results indicates that the ethanol associates with the spheres, but in what way is uncertain.

Ethanol is a straight-chain alcohol, i.e. non-polar, that is fully miscible in water [46], so it doesn't in and of itself, explain why the spheres prefere the surface rather than the bulk of the water, nor why they resurface. Two possible reasons are proposed. The ethanol-containing solution has a lower mass density (not counting spheres) which causes it to rise, carrying with it spheres that then redistributes themselves on the surface as they are slightly hydrophobic. Alternatively, or in addition, the ethanol associates itself with the individual spheres, e.g. by absorbtion, resulting in a lower mass density, or some association with the sphere surface, which together with their hydrophobic nature causes them to seek the surface of the water. From observations during the experiments, it was, as earlier mentioned, noticed that spheres kept diffusing onto the water film for severeal minutes. However, diffusion of indivdual spheres across the water film only took a few seconds, making it probable that ethanol associates in some way with the spheres rather than dragging them along. If the spheres were to be dragged along by ethanol diffusing onto the water film, the process should halt in just a few seconds, considering the speed of the spheres. Also, as ethanol is fully miscible in water, it won't simply distribute itself only on the surface, but within the water film as well.

So, returning to why the grains of the crystalline monolayers were larger for low concentrations of ethanol than for high, and why the experiments with concentrations lower than 1 wt.% failed. If one assumes, as suggested above, that the ethanol associates in some way with the individual spheres, there will be a specific amount at which all the spheres have been associated with ethanol, without too much extra ethanol. Reduce the amount of ethanol and there will be, depending on the nature of the association, an amount of spheres relatively/sufficiently unaffected by ethanol. In this case, spheres will also diffuse within the water film, which was observed. Actually, the spheres were observed to move close to the wafer surface, possibly due to their higher mass density, with a small amount of spheres diffusing onto the water film surface, supporting the hypothesis presented above. If, on the other hand, more ethanol was added, there would be an excess of ethanol in the solution. In this case ethanol will diffuse into the water film, and can affect both the diffusion and the crystallization process, and in the end the resulting monolayers.

But why do the spheres crystallize? First of all, ethanol does not seem to cause the crystallization, but makes it possible as it enables the spheres to float on top of the water. According to Nagayama et al. [30] there will be attractive capillary forces between spheres floating on a liquid, due to gravity driven surface deformation. These forces were determined to be overcome by the thermal energy when the spheres had a radius of less than about $10\mu m$. However, these calculations were done for a sphere mass density of $1.05gcm^{-3}$ on a pure water water film. The Ugelstad spheres used in the experiments here had a mass density of $1.16cm^{-3}$, which should lead to a substantial increase in these forces. In addition, ethanol is present, which could also affect the surface deformation.

The experiments done with PS spheres with a diameter of 490nm and mass density of $1.05gcm^{-}3$, indirectly support that attractive capillary forces between the floating spheres were the mechanism behind crystallization. These sphere could also be diffused onto the water film, but in this case both with and without ethanol. It is believed that this is due both to their more hydrophobic surface and lower mass density, compared to the Ugelstad spheres. However, these spheres didn't crystallize on the water surface, but at the leading edge of the evaporating water film. Most probably, the spheres can't crystallize on the surface as the attractive forces between them are overcome by the thermal energy. As the water film dries and becomes thinner than a sphere diameter at the film edge, the spheres no longer float, but rest on the wafer surface. The attractive capillary forces are much stronger in this case, as explained in the theory, and the crystal growth can begin. According to Nagayama et al., these forces can be significant compared to the thermal energy for spheres with a dimater down to 10nm.

When the crystallization has started, there will be a flow of water and spheres

towards the leading edge of the evaporating film, both due to a pressure difference in the meniscus relative to the bulk of the water film, as explained in the theory, but also due to a compensating flux due to water evaporation. This water flux brings with it spheres, allowing a multilayer structure to be grown, i.e. an opal. However, this means that the spheres are "used up" before the entire wafer is covered with spheres, and should leave an area in the middle where no spheres exists, which was in fact observed.

All in all, this method proved to be suitable for monolayer growth of spheres on a wafer, but is most probably limited to quite "large" spheres. To grow multilayer structures it was unfortunately unsuitable, as it either left large areas uncovered, for small spheres, and only monolayers were achieved with larger spheres. As multilayer structures was desired, this lead to new methods being adopted and the discontinuation of further work with this method.

6.3 Opal growth method #2: Draining

With this method, opals were grown on silicon substrates by slowly draining a sphere solution out of a reaction vessel. The substrates were placed vertically in the solution, allowing the meniscus that forms at the substrate-air-solution contact line to move along the substrate, as the solution is drained. Opals of approximately uniform thickness were successfully grown, with a grain size improving from 10x10μm at the top to 50x100μm at the bottom. These grains were always longest in the direction parallel to the direction of growth. With SEM it was verified that adjacent grains had the same crystalline orientation, separated by a crack rather than a grain boundary. A possible explanation for this is that far larger grains initially forms, but that they crack up as the spheres shrink when they dry. This effect has been reported by several groups [28, 29, 31], and was shown in several of the SEM images provided in the Results chapter. It should be mentioned that the grain size was determined based on the observed cracks. If grain boundaries were present within these "grains", this was not taken into consideration. The sample presented from this method will be denoted D1 later in the discussion.

The reason for the increased grain size towards the bottom of these samples was though to be related to a decreasing sphere concentration and meniscus speed during growth (will be explained below). Why this should lead to larger grains remain undetermined, but a possible explanation is that there is some ideal meniscus speed for a given sphere concentration and meniscus film thickness. No attempt was done with this method to verify this, as will be explained, but it was done with method #3.

This method had some problems associated with it, which, together with a limited suply of spheres and superior results obtained with method #3, led to the

discontinuation of further experiments with it. Some of the most severe problems were associated with the reaction vessel used. The reaction vessel valve was very inaccurate, and left poor control of the opening at the bottom of the vessel. This, combined with the fact that there was a seemingly abrubt transition between no flow and flow, made it very hard to control the starting speed. When I say an abrupt transition between flow and no flow, this implies that it was experienced this way, perhaps due to the inaccuracy of the valve. An abrupt transition can also appear if the opening is increased from being so small that the spheres simply clog it, to being large enough for the spheres to pass through. It seems probable that something like the latter occured, as the problems with flow were far less pronounced when only water was added to the vessel.

When the solution started to drain out of the vessel, spheres began to crystallize on both the substrate and on the inside of the reaction vessel. As the evaporation of water was insignificant during the experiments, this should result in a decrease in the sphere concentration during the experiment. With a decreasing sphere concentration, one would expect a steadily thinner structure, but this was not observed. In fact, the thickness of the opal seemed to remain unchanged. But why?

As the solution is drained from the vessel, the pressure at the valve of the reaction vessel is reduced, which results in a decreased flow out. The effect of this is that the meniscus speed along the substrate is reduced, leading to a thicker opal [28, 29, 31]. In fact, the meniscus speed was reduced from 450nm/s to 200nm/s during the experiment. If the effect of reduced speed is as large as the effect of reduced sphere concentration, the thickness will remain unaffected, which seems to be the case here.

Another problem that appeared in these experiments, was that a thin layer of dust particles settled on the solution surface during opal growth. This was due to the length of the experiemnts, usually 12-24 hours, and can easily be removed by moving the setup to a cleaner environment, such as a clean-room or a glovebox. Whether this layer of dust had any effect on the opal quality was unknown, but no large amounts of dust was immediately visible on the samples. The accumulation of dust did however lead to a halt in re-using the solutions used with this method in method #3.

The draining approach turned out to be suitable for vertical opal growth, an opals with an average size of 50x50μm were grown. But, due to the problems with the reaction vessel used, it was decided to focus on the next method. This method utilized evaporation, rather than draining, to initiate the meniscus movement along the substrate.

6.4 Opal growth method #3: Evaporation

With this method, opals were grown on silicon substrates partially submerged vertically in a solution, by evaporation. Evaporation of the solution causes the meniscus that forms at the substrate-air-solution contact line to move along the substrate, allowing for opal growth, as explained in the theory. The setup was placed in a preheated oven, at T=50℃ and T=63℃. Compared to method #2 this method produced thicker samples, which was believed to be due to the decresed meniscus speed, which was 50nm/s at 63℃ and 25-30nm/s at 50℃. For method #2 this speed varied from 200-450nm/s during the experiment. The grains of these samples were far larger too, in the order of 200x400μm for the largest ones.

The samples made with this method are listed in table 6.1 with the different process parameters listed. Photos of these samples, as presented in the Results, show that their color varies depending on where one is relative to the sample. This was believed to be due to partial bandgaps in certain directions for certain wavelengths, as explained in the theory. Colors that were observed, were blue, red, green and a reddish golden color. All of the samples with a coloring showed all these colors.

Sample	Process temperature	Sphere conc.	# substrates in the vial
E1	50℃	$\leq$0.35 wt.%	1
E2	63℃	0.3 wt.%	1
E3	63℃	0.5 wt.%	1
E4	63℃	0.3 wt.%	2
E5	63℃	0.5 wt.%	2

Table 6.1: List of the different samples made with opal growth method #3. In some of the experiments there were two substrates in the same vial during opal growth, in an attempt to compensate for increased sphere concentration due to water evaporation.

Most of the samples made with this method appeared whiter towards the bottom, which was thought to be due to an increased thickness (more on this later). This increase in thickness was due to an increased sphere concentration as water evaporates during the experiment. In an ettempt to offset this, two substrates were placed in the vial so that more spheres could crystallize. Judging from samples E4 and E5, this was a success. In these cases, one of the samples was examined with SEM after sintering, i.e. heating to 95℃ to make the spheres adhere better to each other, while the other was examined after the attempted inversion. This was done as the bare opals (sintered or unsintered) needed to be coated with a thin layer of carbon to make them conducting, for a good result with the SEM, which

made them unsuitable for further processing. This made the characterization a bit inaccurate, as these samples weren't necessarily perfect twins. Even so, most of the discussion will relate to the samples made this way, i.e. E4 and E5.

Opals of different thicknesses were grown by varying the wt.% of spheres in the solutions. With a concentratiion of 0.3 wt.%, opals with a thickness of approximately 18 layers were grown, as determined by crossectional images with SEM. By increasing the amount of spheres to 0.5 wt.% spheres, the opal thickness increased to 30-40 layers. Due to the poor crossectional images from this sample, the exact number of layers was difficult to determine. This problem could have been solved with a more precise cutting tool than a scalpel, but this was not available. That the thickness of the opals increased with increasing sphere concentration is not surprising, as this allows for a higher flux of spheres towards the meniscus.

As for the opals made with method #2, these opals had long cracks running parallel to the growth direction. For the samples prepared at 63℃ the distance between them became longer; approximate distances were $100\mu m$ for samples E2 and E4, $150\mu m$ for E3 and $200\mu m$ for E5. This indicated that the distance between the cracks also increased for an increase in sphere concentration, or alternatively opal thickness. Why sample E3 and E5 differed here was a bit unclear, but possible explanations are intereference from the meniscus of E5s twin sample or from small variations in the surface properties of the substrates, which could affect the thickness and shape of the meniscus. Another possebility is that the substrte was held at angle slightly lower than 90°. The length of these grains also increased, to 100-200μm for E2 and E4, and to 300-400μm for E3 and E5. The largest grains did however have greatly defected surfaces, but grains with a size of 150x300μm were successfully achieved with a "nice" surface.

Returning to the cracks themselves; as indicated above, the distance between the cracks became even longer with an increase in sphere concentration, i.e. for thicker structures. For the thinnest opals, samples D1 and E1, the cracks were about $1\mu m$ wide, while for the thicker opals prepared at 63℃ the cracks widened to 2-3μm (E2 and E4) and 4-5μm (E3 and E5). For sample E5 some o the cracks widened to about $20\mu m$, but this was not the average for the sample. These widths were determined with SEM, but it should be mentioned that samples E2-E5 were sintered before being looked at, which, judging from optical microscope images, resulted in some additional cracking. This is most probably due to further shrinking of the spheres, but may also be due to some deformation of the spheres, as they are heated to their softening temperature during sintering. Even so, the unsintered versions of samples E2-E5 showed wider cracks than E1 and D1, although this weren't shown with SEM. The samples were sintered before being examined with SEM as the unsintered samples tended to be lifted from the substrate during examination. This was a combination of poor stiction to the substrate and

charging effects due to non-conducting samples. This was somewhat mitigated by coating the samples with a thin conducting layer of carbon (a few nanometers), but excempting the very thin samples like D1 and E1, all the samples had to be sintered for any useful images to be taken.

So, why does the distance between and the width of the cracks increase when the temperature and sphere concentration are increased? With an increase in temperature, it is believed that the stresses in the structure caused by the shrinking spheres are somewhat relieved during cracking, so that instead of cracking up in a multitude of places, the distance between and width of the cracks increases. But why the longer distance between cracks with an increased sphere concentration, as was seen for sample E3 and E5? One hypothesis was that the forces holding these structures together increases, simply due to the increased amount of spheres, i.e. increased thickness.

Although the distance between and the width of these cracks increased, the surface of the thicker samples had a lot more defects. These came in the form of line defects, making up the triangular shapes seen with the optical microscope, grain boundaries and grains that seem to have been grown in crystallographic directions other than the [110] direction. The observed growth directions were [111], the desired one, [110] and [101]. It is thought that the two latter directions corresponds to the bright blue and red areas seen with the optical microscope, while the green areas corresponds to the usually observed [111] direction. Whether the grains actually grew in the [110] and [101] directions, or if they were simply surface defects could not be determined, but considering the well defined red and blue colors seen, it's not unlikely that the former is the case. Areas of less well defined colors, much seen on the thicker samples, is thought to be related to highly defected surfaces. These areas had a lot of line defects, grain boundaries and frequent changes in crysallographic growth directions. Samples with this kind of surface, appeared white when looked upon with the naked eye. A possible explanation for this is that rapid variations in the wavelength reflected, both by changes in crystallographics growth direction and crystallographic orientation, result in an effective white appearance. Another possebility is that there is a lot of Mie-scattering from the defected areas, i.e. light scattered by spherical particles. A combination of the two is naturally possible, and quite likely.

But why were the surface of the thicker samples so highly defected? Three possible explanations are proposed. Firstly, defects deep down in the structure can increase towards the surface, i.e. the disruptions caused by the defects will increase more and more. For thicker structures theses effects will then naturally be larger than for thinner structures. A possible counter argument to this, is the way these opals grow, i.e. parallel to the substrate, but in that case the defects will grow along the growth direction and may reach the surface in any case. Secondly,

the grown opals may become thicker than what the meniscus can easily support, as the meniscus has a finite thickness. It's not unlikely that this may affect the opal surface. Thirdly, the meniscus may be affected by the menisci forming at the walls of the glass vial and the 2nd substrate in it. The distance between substrate and vial and substrate and substrate was at least 2cm, but it is not known if that was enough.

All in all , the method proved suitable for growing opals of high quality and of even thickness. The quality of the samples was seen to improve with an increased temperature, with the largest high quality grains being approximately 150x300μm. But is this large enough? For the finished inverted opal structure to exhibit the desired optical properties, the structure should be several wavelengths in all directions. This is most probably fullfilled with the obtained structures, which extends more than 100 wavelengths in all directions, using 1000nm as the referance wavelength.

6.5 Comparison of the opal growth methods

Growth method	Diffusion	Draining	Evaporation
Structure	Monolayer	Multilayer	Multilayer
Process temperature	20.5℃	20.5℃	50℃/63℃
Grain size	2-300μm^2	50x50μm	50x50/150x300μm
# spheres in grain	60-90 in either directions	100x100	100x100/300x600
Process time	90 hours	ca.24 hours for a 3cm sample	16.5 hours for a 3cm sample

Table 6.2: Table showing the properties of the three opal growth methods used in the master project. Process time for the last two methods were calculated based on the meniscus speeds given in the results, which was 200-400nm/s for the draining method, and 500nm/s for the evaporation method.

6.6 Opal inversion

Opal inversion was performed in three steps: (1) sintering of the opals to make the spheres adhere better to each other, (2) filling in the gaps with silicon using PECVD and (3) calcining at 600℃ to remove the spheres by evaporating them. With this method, inverted opals were succefully made, as was shown in the Results.

Sintering was confirmed to succeed with SEM, where it was obvious that the spheres had fused together at their contact points. This also proved to be an important step to be able to characterize the thicker samples with SEM, as the samples no longer got lifted off the substrate. The reason for this could simply be that the spheres fused to the substrate at their contact points, similarily to what happened between the spheres. Calcining also resulted in some additional widening of the cracks, up to $20\mu m$ in certain areas on sample E5. This was thought to be a result of further shrinking of the spheres.

Silicon was deposited using a low temperature (90℃), low pressure (300mTorr) PECVD process which was allowed to run for 1.5 hours. This time was chosen based on the growth rate in the standard silicon deposition process used at IFE, which is about 650nm per hour at 230℃, and the desired thickness which was 650nm. The extra half hour was chosen as it was believed that the deposition rate would be reduced with the lower temperature. 650nm was chosen, as this is what's needed to fill the gaps between 8 layers of spheres with a filling fraction of 20%[1]. 8 layers was somewhat arbitrarily chosen, but the time spent with the PECVD was the limiting factor. From optical microscope images, it was however clear that at least some of the silicon was simply deposited on the surface. Unfortunately, there was no time for SEM images to be taken between this step and the next. With the optical microscope some areas were observed to have bright colors, which in some cases could also be seen with the naked eye, but the surface in general was grey. Why some areas appeared colored was thought to be evidence of silicon actually infiltrating the structure, as the inverted opal was expected to exhibit some coloring. Strictly speaking, as long as silicon fills in the spaces between the spheres an inverted opal is achieved, but with a lower dielectric contrast than if the spheres were to be removed. One concern about the PECVD process, was that the silicon deposited would be of poor quality. It was believed that the silicon would be porous, amorphous and hydrogen rich. This would most assuredly reduce the refractive index, and leave a lot of unsaturated silicon, i.e. silicon with dangling bonds. Due to this, a high calcining temperature was chosen, as this might activate some of the hydrogen, i.e. bind it to the silicon, and help crystallize the silicon.

The next step was to remove the spheres, which was done by calcining the samples for 2.5 hours at 600℃. Initial attempts with a bare opal, i.e. no silicon deposited, showed that this removed the spheres, most probably by evaporating the PS. This also succeded, to a certain degree when silicon had been deposited, as was confirmed with SEM when inverted opals were found on the samples. It should be mentioned that for the most part the spheres stayed intact after calcining. Some small areas were inverted though, and were thought to correspond to the brightly colored areas mentioned above. These areas could no longer be seen

[1] A filling fraction of 26% would have perfectly filled the gaps between the spheres.

with the naked eye, but they were easily seen with the optical microscope, where brightly colored areas at the edges of the grains could be seen. The fact that these areas were seen at the edges of the grains, were believed to be no coincidence. One of the major problems with the inversion process used, is probably the transport of PS out of the structure. With some of the silicon simply being deposited on top of the structure, effectively acting like a cap, the transport of PS would be limited to the surfaces within the cracks, where the highly colored areas were seen. Another thing that supported this, was that the colored areas were mostly seen where the opal had cracked up the most, which would ease the problem of PS transport out of the structure. In the Results, an optical microscope image was shown of a larger colored area (figure 5.35), which didn't have silicon on top of it after PECVD. After calcining, a thin transparent layer was observed on top of this area. A possible explanation for this, is that not all the PS initilly trapped within the structure had time to be transported out during calcining, leaving a thin layer on top of the opal after the sample was removed from the oven. This could most probably be remedied by increasing the calcining time. If in fact this was the case, it clearly shows how hard it is to transport the PS out of the structure, especially when there is a cap of silicon on top of it. A possible way to ease the transport of PS out of the structure, could be to remove the cap on top of the structure with a selective dry etch, e.g. RIE. For sample E4, where no really wide cracks were found, no colored areas were observed, and no inverted areas could be found with SEM.

The silicon also seemed to be affected by the calcining process, and was seen to have been lumped together with the optical microscope. This was seen both for the silicon deposited directly on the substrate and on top of the opal.

Inversion was seen to be successfull with the used process, but it is clear that further improvement is needed before large scale inverted opals can be made. The sintering step seems to work well, but things need doing both with the silicon deposition and the PS removal.

Chapter 7

Conclusion

In this master project, two different methods were used in attempt to make an opal; a diffusion process of spheres from a ethanol containing solution onto a water film, and crystallization of spheres from a solution on a vertical substrate at a moving meniscus. The movement of the meniscus in the latter case was achieved in two ways; draining and evaporation of the sphere solution. Some of the grown opals were further processed to invert them. This was done by filling in the gaps between the spheres with silicon, and then removing the spheres by calcining them at 600℃, which was seen to successfully produce inverted opals. Reflection simulations of inverted opals on silicon substrates were also done.

The reflection simulations showed that the inverted opal can indeed be used as a rear reflector in solar cells, but it was not determined how much of the light will be reflected into diffractive orders, which is of particluar interest. Further study should focus on this.

With the first opal growth method, which was based on work in the preceeding project [34], wafer sized monolayers were successfully grown. The quality of these layers was seen to improve for low concentrations of ethanol in the sphere solution, although too low concentrations $\leq 1wt.\%$ proved insufficient to initiate diffusion. Sphere concentration in the solutions didn't seem to affect the quality of the monolayers, but a tendency towards a reduced amount of extra spheres on top of the monolayer could be seen for lower concentrations. The method proved successfull for Ugelstad spheres, but not for the smaller and lighter PS spheres. It is believed that the thermal energy overcomes the attractive forces between the spheres in the latter case, as the attractive forces depends on the weight and size of the spheres. As a way to make multilayered structures, which was desired, this method proved unsuitable. A multilayer structure could be made with the PS spheres, but this resulted in an opal of varying thickness and a large area without spheres at all.

With the draining approach to the second method, opals of a relativly even

thickness were achieved, with a coloring that depended on where they were viewed from, indicating partial bandgaps. These opals had a grain size of about 50x50μm, but there was evidence of these grains having been larger. The grains were separated by cracks, where the crystallographics orientation didn't change across it. This was also the case for the opals made with the evaporation approach.

With the second way to initiate meniscus movement along a substrate, evaporation, the entire setup was placed in an oven to increase the evaporation rate. This led to opals of increasing thickness during the experiment, due to an increasing sphere concentration as the water evaporated. To offset this, a second substrate was added to allow more spheres to crystallize, which yielded opals of even thickness. The method in general resulted in thicker structures and larger grains compared to the draining approach, and the grains were seen to increase with an increase in temperature and sphere concentration, with the largest achieved grains being of 200x400μm. The surface of the largest grains were however heavily defected, with line and point defects, and sub grains grown in different crystallographics directions or of a different orientation, so the term "grain" may not be an entirely fitting description. Grains with a surface not heavily defected were achieved with a maximum size of about 150x300μm. It was noted that the thicker structures adhered poorly to the substrate, making them practically impossible to investigate with SEM, as they got lifted off the substrate. This problem was solved by sintering the opals, as explained below, and by coating the samples with a thin conducting layer of carbon.

The opals made with the evaporation approach to vertical deposition, were further processed to invert them. First the opals were sintered, i.e. heated to the softening temperature of the spheres, which had the effect of fusing the spheres together at their contact points, and improve the adhesion to the substrate. Silicon was then deposited with a PECVD process, before the samples were calcinated at 600℃. The PECVD process was meant to fill the gaps between the spheres with silicon, but silicon also settled on the surface of the opal. However, for the most cracked up areas of opals, brightly colored areas could be seen at the edges of the grains. After calcining, which was done to evaporate and remove the spheres, these areas still remained colored, and was believed to correspond to the inverted areas found with the SEM. Inverted areas were however rare, as the spheres mostly remained after calcining. This was thought to be due to problems with transporting the PS out of the structure due to the cap of silicon on top of the opal.

The process used in this master project was able to produce the desired inverted opals, but great improvement is needed with the silicon deposition and sphere removal process. With this process in place, wafer scale inverted opals should be quite "easy" to make with the approach taken here.

Chapter 8

Further work

The focus in this master project was split in three; (1) monolayer growth of Ugelstad spheres, (2) opal growth of PS spheres and the subsequent inversion and (3) simulations with MEEP. Although inverted opals were made in the master project, there is still a lot that should be done.

If large, crystalline monolayer are wanted, the method used with Ugelstad spheres show much promise for further improvement, and much is still unknown about the mechanisms behind crystallization. Investigation of temperature effects, solution and water film composition and sphere size is still not done. Doing so could yield more knowledge about the mechanisms involved, and as a consequence lead to possible improvements. Also, the method for making contact between solution and water film, is in great need of improvement, as the one used here introduced a certain randomness from experiment to experiment.

When it comes to the opals made with PS sphere, there is also alot that can and need to be done. With the draining approach to opal growth, issues with variation in draining rate and sphere concentration needs to be solved. Possible avenues here could be to place the entire setup in a pressure controlled chambre, where the pressure could be gradually increased to compensate for the decreasing amount of water in the vessel. This may however be rather tedious , and a different approach altogether may be desired.

The major part of the opals made in the master work were made with the evaporation method, which proved successfull for growing relatively large opals of even thickness. However, more work can be done to determine the ideal amount of spheres in the solution and the ideal process temperature. Other avenues of improvement could be to investigate the effect of the surface properties of the substrate on opal quality, or similarily, to change the solution composition in order to alter its surface tension. The idea behind this is that this will change the shape and thickness of the meniscus that appears at the substrate-air-solution contact line, which was believed to affect the ideal thickness of the opal.

It was noted that some of the thicker samples had a greatly increased amount of surface defects, and some investigation should go into the nature of these. Are they simply surface defects, or are they a sign of defects buried deep in the structure?

Although inverted opals were achieved, the inversion process needs improvement for it to produce inverted opals of a sufficient size. Optimization of both the silicon deposition and sphere removal methods used needs to be done, and alternative routes like atomic layer deposition for the material deposition step, and selective etching of the spheres ought to be explored.

On the simulation side, reflection spectra for more than normal incidence needs to be done, as well as band diagram calculations for the inverted opal on a substrate. Optical characterization of the opals and inverted opals also need doing, which could give an indication of the quality of the structures. This should also be done in order to find out how many layers of spheres are necessary to yield satisfactory reflection properties, as well as to find out how much of the light is reflected into diffractive orders. The latter should be done both with simulations and with experimental measurements.

Bibliography

[1] International Energy Agency. World energy outlook 2008: Executive summary, 2008.

[2] Jenny Nelson. *The Physics of Solar Cells*. Imperial College Press, 2006.

[3] www.solarbuzz.com. 19.11.2008.

[4] P. Bermel, C. Luo, L. Zeng, L. C. Kimerling, and J. D. Joannopoulus. Improving thin-film crystalline silicon solar cells efficiencies with photonic crystals. *Optics Ecpress*, 15(25):16986–17000, 2007.

[5] L. Zeng, Y. Yi, C.-Y. Hong, J. Liu, N. Feng, X. Duan, and L. C. Kimerling. Efficiency enhancement in si solar cells by textured photonic crystal back reflector. *Applied physics letters*, 89:111111–(1–3), 2006.

[6] K. Varis and M. Mattila. Reflection of focused beams from opal photonic crystals. *Optical Society of America*, 13:2653–2667, 2005.

[7] J. D. Joannopoulos, S. G. Johnsen, J. N. Winn, and R. D. Meade. *Photonic Crystals: Molding the Flow of Light*. Princeton University Press, 2nd edition edition, 2008.

[8] Yu. A. Vlasov, Xiangh-Zheng Bo, J. C. Sturm, and D. J. Norris. On-chip natural assembley of silicon photonic bandgap crystals. *Nature*, 414:289–293, 2001.

[9] Charles Kittel. *Introduction to Solid State Physics*. Johm Wiley & Sons, 8th edition edition, 2005.

[10] B. E. A. Saleh and M. C. Teich. *Fundamentals of Photonics*. John Wiley & Sons, Inc., 2nd edition edition, 2007.

[11] E. Yablonovitch, T. J. Gmitter, and K. M. Leung. Photonic band structure:the face-centered cubic case employing nonspherical atoms. *Phys. Rev. Lett.*, 67:2295–2298, 1991.

[12] K. M. Ho, C. T. Chan, C. M. Soukoulis, R. Biswas, and M. Sigalas. Photonic band gaps in three dimensions: new layer-by-layer periodic structures. *Solid State Comm.*, 89:413–416, 1994.

[13] H. S. Sözüer and J. P. Dowling. Photonic band calculations for woodpile structures. *J.Mod.Opt*, 41:231–239, 1994.

[14] H. S. Sösüer, J. W. Haus, and R. Inguva. Photonic bands: Convergence problems with plane wave method. *Phys. Rev. B*, 45:13962–13972, 1992.

[15] http://www.aps.org/publications/apsnews/200208/forefronts.cfm. 28.11.2008.

[16] S. J. F. L. Pedrotti, L. M. Pedrotti, and L. S. Pedrotti. *Introduction to Optics*. Pearson Prentice Hall, 2007.

[17] http://en.wikipedia.org/wiki/Silicon. 30.05.2009.

[18] Zhi-Yuan Li and Zhao-Qing Zhang. Fragility of photonic bands in inverse-opal photonic crystals. *Physical Review B*, 62(3):1516–1519, 2000.

[19] Yu. A. Vlasov, V. N. Astratov, A. v. Baryshev, A. A. Kaplyanskii, O. Z. Karimov, and M. F. Limonov. Manifestation of intrinsic defects in optical properties of self-organized opal photonic crystals. *Physical Review E*, 61(5):5784–5793, 2000.

[20] Raul Mayoral, Joaquin Requena, José S. Moya, Cefe López, Adelaida Cintas, Hernán Miguez, Francisco Meseguer, Luis Vázquez, Miguel Holgado, and Álvaro Blanco. 3d long-range ordering in an sio_2 submicrometer-sphere sintered superstructure. *Advanced Materials*, 9(3):257–260, 1997.

[21] http://en.wikipedia.org/wiki/Colloid. 30.11.2008.

[22] Alvaro Blanco, Emmanuel Chomski, Serguei Grabtchak, Marta Ibisate, Sajeev John, Stephen W. Leonard, Cefe Lopez, Francisco Meseguer, Hernan Miguez, Jessica P. Mondia, Geoffrey A. Ozin, Ovidiu Toader, and Henry M. van Driel. Large-scale synthesis of silicon photonic crystal with a complete three-dimensional bandgap near 1.5 micrometers. *Nature*, 405(437-440), 2000.

[23] Bernd Griesebock, Marc Egen, and Rudolf Zentel. Large photonic films by crystallization on fluid substrates. *Chemical Materials*, 14:4023–4025, 2002.

[24] Hiroshi Fudozi. Fabricating high-quality opal films with uniform structure over a large area. *Journal of Colloid and Interface Science*, 275:277–283, 2004.

[25] Sang Hyuk Im, Yong Taik Lim, Duck Jong Suh, and O Ok Park. Three-dimensional self-assembly of colloids at a water-air interface: A novel technique for the fabrication of photonic bandgap crystals. *Advanced Materials*, 14(19):1367–1369, 2002.

[26] Antony S. Dimitrov and Kuniaki Nagayama. Continuous convective assembling of fine particles into two-dimensional arrays on solid surfaces. *Langmuir*, 12:1303–1311, 1996.

[27] Marc Egen, Rebecca Voss, Bernd Griesebock, and Rudolf Zentel. Heterostructures of polymer photonic crystal films. *Chemical Materials*, 15:3786–3792, 2003.

[28] Martyn A. McLachlan, Nigel P. Johnson, Richard M. De La Rue, and David W. McComb. Thin film photonic crystals: synthesis and characterisation. *Journal of Material Chemistry*, 14:144–150, 2004.

[29] Zhong-Ze Gu, Akira Fujishjima, and Osamu Sato. Fabrication of high-quality opal films with controllable thickness. *Chemical Materials*, 14:760–765, 2001.

[30] P. A. Kralchevsky, N. D. Denkov, V. N. Paunov, O. D. Velev, I. B. Ivanov, H. Yoshimura, and K. Nagayama. Formation of two-dimensional colloid crystals in liquid films under the action of capillary forces. *Journal of Physics: Condensed Matter*, 6:A395–A402, 1994.

[31] P. Jiang, J. F. Bertone, K. S. Hwang, and V. L. Colvin. Single-crystal colloidal multilayers of controlled thickness. *Chemical Materials*, 11:2132–2140, 1999.

[32] David J. Norris, Erin G. Arlinghaus, Linli Meng, Ruth Heiny, and L. E. Scriven. Opaline photonic crystals: How does self-assembley work? *Advanced Materials*, 16(16):1393–1399, 2004.

[33] M. Bardosova and R. H. Tredgold. Ordered layers of monodispersive colloids. *Journal of Materials Chemistry*, 12:2835–2842, 2002.

[34] Håvard Granlund. Synthesis of a monolayer crystal from ugelstad spheres. 2008.

[35] http://en.wikipedia.org/wiki/Meniscus. 03.06.2009.

[36] Paul C. Hiemenz and Raj Rajagopalan. *Principles of Colloid and Surface Chemistry*. Taylor & Francis Group, third edition, revised and expanded edition, 1997.

[37] Bing Dai and Alan Graham. Disjoining pressure for non-uniform thin films. http://www.lanl.gov/orgs/adtsc/docs/section8/18Dai.pdf.

[38] Siun-Chuon Mau and David A. Huse. Stacking entropy of hard-sphere crystals. *Physical review E*, 59(4):4396–4401, 1999.

[39] http://en.wikipedia.org/wiki/Atmospheric_drag. 03.06.2009.

[40] E. Palacios-Lidón, B. H. Juárez, E. Castillo-Martínez, and C. López. Optical and morphological study of disorder in opals. *Journal of Applied Physics*, 97:063502–(1–6), 2005.

[41] Wei Gao and Nigel M. Sammes. *An introduction to Electronic and Ionic Materials*. World Scientific Publishing Co. Pte. Ltd., 2006.

[42] http://en.wikipedia.org/wiki/Scanning_electron_microscope. 19.06.2009.

[43] http://ab initio.mit.edu/wiki/index.php/Meep. 19.06.2009.

[44] http://ab initio.mit.edu/wiki/index.php/Yee_lattices. 24.04.2009.

[45] Andreas Bielawney, Johannes Üpping, Paul T. Miclea, Ralf B. Wehrspohn, Carsten Rockstuhl, Falk Lederer, Marius Peters, Lorenz Steidl, Rudolf Zentel, Seung-Mo Lee, Mato Knez, Andreas Lamertz, and Reinhard Carius. 3d photonic crystal intermediate reflector for micromorph thin-film tandem solar cell. *Physica status solidi (a)*, 205(12):2796–2810, 2008.

[46] http://en.wikipedia.org/wiki/Ethanol. 15.06.2009.

Appendix A

MEEP source code

```
;fcc file

(define-param no-opal? true)     ;if true, reference measurement
(set! eps-averaging? false)      ;if true, the simulation fails for
                        ;for structures that traps light
                        ;(electric field "blows up")


;------various structure parameters-----------------------------

(define-param r2 (/ 1 (sqrt 6 )))
(define-param rsph (/ 1 (sqrt 8 )))              ;radius of spheres
(define-param dz (* (/ (sqrt 8 ) (sqrt 3)) rsph));distance in the
                        ; z-direction between center of sphere layers

(define-param pmlt 2)                    ;pml layer thickness
(define-param d 9)                       ;distance between material
                                         ;and source


(define y1 (* (sqrt (/ 4 3 )) rsph))     ;2/3 from cell_center towards
(define y2 (* (sqrt 3 ) rsph))           ; cell_center to y-edge
(define y3 (* (/ 1 (sqrt 3 )) rsph))     ; 1/3 from cell_center
                                                ;towards y-edge

(define-param N 2)
        ;number of unitcells
```

```
        ;defined as number of
        ;3 layers, i.e. N = 1


(define-param unitcell (+ (* 2 dz) (* 2 rsph) (* 3 (- N 1) dz)))
                                        ;z-direction

(define-param subt 5)                   ;thickness of the substrate

(define sx (* 2 rsph))                  ;size of cell in x-direction
(define sy (* 2 (sqrt 3 ) rsph))        ;size of cell in y-direction
(define sz (+ d subt unitcell))         ;size of cell in z-direction



(define cell_center (- (/ sz 2) subt rsph dz))
        ;z-coord. of center of the first layer of spheres


(define substrate_center (- (/ sz 2) (/ subt 2)))
(define inc_center (+ (/ sz -2) (/ (+ d rsph) 2)))
        ;center of the substrate and the incoming material


(define-param e1 13)
        ;dielectric constant of silicon

(define Si (make dielectric (epsilon 13)))
        ;diel.const. of filling material

(define M1 air)
        ;What the spheres are filled with

(define M2 (make dielectric (epsilon 13)))
        ;diel.const of the material between spheres



(set! geometry-lattice (make lattice (size sx sy sz)))
        ;cell dimensions
```

```
(set! geometry

;--------------Referance run without opal----------------------

(if no-opal? (list
(make block (center 0 0 0) (material air)
                (size infinity infinity infinity))

                )       ;end list, incoming medium


;-----------------If opal is present-----------------------------

(append (list
(make block (center 0 0 0) (material air)
                (size infinity infinity infinity))

                )       ;end list, incoming medium



;--------------The opal structure-------------------------------

; Infill material, defined as a structure of spheres larger than
; the spherical airholes that will be placed on top of these
; later.

        (list
        ;Lag 1 - kuler, infill

        (make sphere (center 0 (* y1 -1) (+ cell_center dz))
                        (radius r2)
                        (material M2))

        (make sphere (center 0 (+ y2 y3) (+ cell_center dz))
                        (radius r2)
                        (material M2))
```

```
(make sphere (center rsph y3 (+ cell_center dz))
                (radius r2)
                (material M2))

(make sphere (center (* rsph -1) y3 (+ cell_center dz))
                (radius r2)
                (material M2))

;Lag 2 - kuler, infill

(make sphere (center rsph y2 cell_center)
                (radius r2)
                (material M2))

(make sphere (center rsph (* y2 -1) cell_center)
                (radius r2)
                (material M2))

(make sphere (center (* rsph -1) y2 cell_center)
                (radius r2)
                (material M2))

(make sphere (center (* rsph -1) (* y2 -1) cell_center)
                (radius r2)
                (material M2))

(make sphere (center 0 0 cell_center)
                (radius r2)
                (material M2))

;Lag 3 - kuler, infill

(make sphere (center 0 y1 (- cell_center dz))
                (radius r2)
                (material M2))

(make sphere (center 0 (+ (* y2 -1) (* y3 -1))
                                (- cell_center dz))
                (radius r2)
```

```
                (material M2))

(make sphere (center rsph (* y3 -1) (- cell_center dz))
                (radius r2)
                (material M2))

(make sphere (center (* rsph -1) (* y3 -1) (- cell_center dz))
                (radius r2)
                (material M2))

;Lag 4 - kuler, infill

(make sphere (center 0 (* y1 -1) (- cell_center (* 2 dz)))
                (radius r2)
                (material M2))

(make sphere (center 0 (+ y2 y3) (- cell_center (* 2 dz)))
                (radius r2)
                (material M2))

(make sphere (center rsph y3 (- cell_center (* 2 dz)))
                (radius r2)
                (material M2))

(make sphere (center (* rsph -1) y3 (- cell_center (* 2 dz)))
                (radius r2)
                (material M2))

;Lag 5 - kuler, infill

(make sphere (center rsph y2 (- cell_center (* 3 dz)))
                (radius r2)
                (material M2))

(make sphere (center rsph (* y2 -1) (- cell_center (* 3 dz)))
                (radius r2)
                (material M2))

(make sphere (center (* rsph -1) y2 (- cell_center (* 3 dz)))
                (radius r2)
```

```
                    (material M2))

        (make sphere (center (* rsph -1) (* y2 -1)
                                    (- cell_center (* 3 dz)))
                    (radius r2)
                    (material M2))

        (make sphere (center 0 0 (- cell_center (* 3 dz)))
                    (radius r2)
                    (material M2))


        ;Lag 6 - kuler, infill

        (make sphere (center 0 y1 (- cell_center ( * 4 dz)))
                    (radius r2)
                    (material M2))

        (make sphere (center 0 (+ (* y2 -1) (* y3 -1))
                                    (- cell_center (* 4 dz)))
                    (radius r2)
                    (material M2))

        (make sphere (center rsph (* y3 -1) (- cell_center (* 4 dz)))
                    (radius r2)
                    (material M2))

        (make sphere (center (* rsph -1) (* y3 -1)
                                    (- cell_center (* 4 dz)))
                    (radius r2)
                    (material M2))

        ); end list, opal infill


;The air spheres, smaller radius than the dielectric spheres
;defined above.

        (list
        ;Lag 1 - kuler, luft
```

```
(make sphere (center 0 (* y1 -1) (+ cell_center dz))
                (radius rsph)
                (material M1))

(make sphere (center 0 (+ y2 y3) (+ cell_center dz))
                (radius rsph)
                (material M1))

(make sphere (center rsph y3 (+ cell_center dz))
                (radius rsph)
                (material M1))

(make sphere (center (* rsph -1) y3 (+ cell_center dz))
                (radius rsph)
                (material M1))

;Lag 2 - kuler, luft

(make sphere (center rsph y2 cell_center)
                (radius rsph)
                (material M1))

(make sphere (center rsph (* y2 -1) cell_center)
                (radius rsph)
                (material M1))

(make sphere (center (* rsph -1) y2 cell_center)
                (radius rsph)
                (material M1))

(make sphere (center (* rsph -1) (* y2 -1) cell_center)
                (radius rsph)
                (material M1))

(make sphere (center 0 0 cell_center)
                (radius rsph)
                (material M1))

;Lag 3 - kuler, luft
```

```
(make sphere (center 0 y1 (- cell_center dz))
                (radius rsph)
                (material M1))

(make sphere (center 0 (+ (* y2 -1) (* y3 -1))
                                (- cell_center dz))
                (radius rsph)
                (material M1))

(make sphere (center rsph (* y3 -1) (- cell_center dz))
                (radius rsph)
                (material M1))

(make sphere (center (* rsph -1)(* y3 -1)(- cell_center dz))
                (radius rsph)
                (material M1))


;Lag 4 - kuler, luft

(make sphere (center 0 (* y1 -1) (- cell_center (* 2 dz)))
                (radius rsph)
                (material M1))

(make sphere (center 0 (+ y2 y3) (- cell_center (* 2 dz)))
                (radius rsph)
                (material M1))

(make sphere (center rsph y3 (- cell_center (* 2 dz)))
                (radius rsph)
                (material M1))

(make sphere (center (* rsph -1) y3 (- cell_center (* 2 dz)))
                (radius rsph)
                (material M1))

;Lag 5 - kuler, luft

(make sphere (center rsph y2 (- cell_center (* 3 dz)))
```

```
                (radius rsph)
                (material M1))

(make sphere (center rsph (* y2 -1) (- cell_center (* 3 dz)))
                (radius rsph)
                (material M1))

(make sphere (center (* rsph -1) y2 (- cell_center (* 3 dz)))
                (radius rsph)
                (material M1))

(make sphere (center (* rsph -1) (* y2 -1)
                                 (- cell_center (* 3 dz)))
                (radius rsph)
                (material M1))

(make sphere (center 0 0 (- cell_center (* 3 dz)))
                (radius rsph)
                (material M1))



;Lag 6 - kuler, luft

(make sphere (center 0 y1 (- cell_center ( * 4 dz)))
                (radius rsph)
                (material M1))

(make sphere (center 0 (+ (* y2 -1) (* y3 -1))
                                 (- cell_center (* 4 dz)))
                (radius rsph)
                (material M1))

(make sphere (center rsph (* y3 -1) (- cell_center (* 4 dz)))
                (radius rsph)
                (material M1))

(make sphere (center (* rsph -1) (* y3 -1)
                                 (- cell_center (* 4 dz)))
                (radius rsph)
```

```
                    (material M1))

        ); end list , opal air holes




;------Substrate----------
        (list (make block (center 0 0 substrate_center) (material Si)

        );end list , substrate

;------termination of spheres, half spheres on top---------------

        (list
        (make block (center 0 0 inc_center) (material air)
                    (size infinity infinity (+ d rsph)))



        )       ;end list , termination

        )       ;end append

        )       ;end if opal

)               ;end set geometry


;--------------Source parameters-----------------------


(define-param fcen 0.65)        ;pulse center frequency
(define-param df 0.6)           ;pulse width
```

```
;----------------------SOURCES-----------------------------


(set! sources (list
        (make source(src
                  (make gaussian-src (frequency (+ fcen 0.1))
                                                    (fwidth df)))
                  (component Ex)
                  (center 0 0 (+ pmlt (* -0.5 sz) 0.5))
                  (size sx sy 0))

       (make source(src
                 (make gaussian-src (frequency (- fcen 0.1))
                                                    (fwidth df)))
                  (component Ex)
                  (center 0 0 (+ pmlt (* -0.5 sz) 0.5))
                  (size sx sy 0))

)) ; End list of sources


;-------Resolution, pml layers and boundary conditions----------



(set-param! resolution 40)
(set! pml-layers (list (make pml (thickness pmlt) (direction Z))))
(set-param! k-point (vector3 0 0 0))
(set! ensure-periodicity true)


;------------Transmission and reflection planes-------------------


(define-param nfreq 700)          ;number of frequencies at which to
(define trans
        (add-flux fcen df nfreq
        (make flux-region
                 (center 0 0 (- (/ sz 2) pmlt 1)) (size sx sy 0)
```

```
        )
        )       ;add-flux end
)       ;define transmission plane end

(define refl
        (add-flux fcen df nfreq
        (make flux-region
                (center 0 0 (+ (/ sz -2) pmlt 1)) (size sx sy 0)
        )
        )       ;add-flux end
)       ;define reflection plane end



;-------------------------RUN-------------------------------------------

;Normal run, loading incident fields from normalization
;to be subtracted
(if (not no-opal?) (load-minus-flux "refl-flux" refl))



(run-sources+
        (stop-when-fields-decayed 50 Ex
                (vector3 0 0 (+ (/ sz -2) pmlt 1))
                1e-6)
        (at-beginning output-epsilon)
;       (at-every 5 (in-volume (volume (center 0 0 0) (size sx 0 sz))
;                               (output-png Ex "-R -Zc dkbluered")))
        (at-every 5
                (to-appended "ex-field"
                        (in-volume (volume (center 0 0 0)
                                (size sx 0 sz)) output-efield-x)))
)       ;end run sources+
;(in-volume (volume (center 0 0 0) (size sx 0 sz))
(if  no-opal? (save-flux "refl-flux" refl)

)       ;end normalization run

(display-fluxes trans refl)
```

Appendix B

Matlab code

```
%Program used to plot transmission and reflection
%data generated from the MEEP simulations
\clear
a=693;%nm
%Reading data files
data = dlmread('fcc6/data.dat',',',0,1);
data0  = dlmread('fcc6/data0.dat',',',0,1);
data1 = dlmread('fcc4/data.dat',',',0,1);
data10 = dlmread('fcc4/data0.dat',',',0,1);
data2 = dlmread('run23a/data.dat',',',0,1);
data20 = dlmread('run23a/data0.dat',',',0,1);
data3 = dlmread('run23b/data.dat',',',0,1);
data30 = dlmread('run23b/data0.dat',',',0,1);
data4 = dlmread('run24/data.dat',',',0,1);
data40 = dlmread('run24/data0.dat',',',0,1);

%Getting frequency interval from read data files

fq = data(:,1);

%Normalizing the transmission,
%reflection and loss data

trans = data(:,2) ./ data0(:,2);
refl  = -data(:,3) ./ data0(:,2);
```

```
trans2 = data1(:,2) ./ data10(:,2);
refl2  = -data1(:,3) ./ data10(:,2);

trans3 = data2(:,2) ./ data20(:,2);
refl3  = -data2(:,3) ./ data20(:,2);

trans4 = data3(:,2) ./ data30(:,2);
refl4  = -data3(:,3) ./ data30(:,2);

trans5 = data4(:,2) ./ data40(:,2);
refl5  = -data4(:,3) ./ data40(:,2);


loss  = 1-trans-refl;
loss2 = 1-trans2-refl2;


figure(1)
hold on

plot(a./fq,loss,'b', a./fq,loss2,'g')%, fq,refl3,'r',
%fq,refl4,'k', fq,refl5,'c')%,b./fq,null,'k')

axis([600 1400 -0.2 0.2 ])
```